

## **INFORMATION TO USERS**

**This manuscript has been reproduced from the microfilm master. UMI films the text directly from the original or copy submitted. Thus, some thesis and dissertation copies are in typewriter face, while others may be from any type of computer printer.**

**The quality of this reproduction is dependent upon the quality of the copy submitted. Broken or indistinct print, colored or poor quality illustrations and photographs, print bleedthrough, substandard margins, and improper alignment can adversely affect reproduction.**

**In the unlikely event that the author did not send UMI a complete manuscript and there are missing pages, these will be noted. Also, if unauthorized copyright material had to be removed, a note will indicate the deletion.**

**Oversize materials (e.g., maps, drawings, charts) are reproduced by sectioning the original, beginning at the upper left-hand corner and continuing from left to right in equal sections with small overlaps.**

**Photographs included in the original manuscript have been reproduced xerographically in this copy. Higher quality 6" x 9" black and white photographic prints are available for any photographs or illustrations appearing in this copy for an additional charge. Contact UMI directly to order.**

**ProQuest Information and Learning  
300 North Zeeb Road, Ann Arbor, MI 48106-1346 USA  
800-521-0600**

**UMI<sup>®</sup>**



**Evolutionary Models and Pulsation Analysis  
of Selected MOST and MONS Target Stars:  
 $\epsilon$  Eridani,  $\beta$  Hydri, and  $\beta$  Geminorum**

Peter A. MacDonald

Submitted in partial fulfilment  
of the requirements for the degree of  
Master of Science

Saint Mary's University  
Halifax, Nova Scotia  
September 2001

© Peter A. MacDonald 2001



**National Library  
of Canada**

**Acquisitions and  
Bibliographic Services**

**395 Wellington Street  
Ottawa ON K1A 0N4  
Canada**

**Bibliothèque nationale  
du Canada**

**Acquisitions et  
services bibliographiques**

**395, rue Wellington  
Ottawa ON K1A 0N4  
Canada**

*Your file Votre référence*

*Our file Notre référence*

**The author has granted a non-exclusive licence allowing the National Library of Canada to reproduce, loan, distribute or sell copies of this thesis in microform, paper or electronic formats.**

**The author retains ownership of the copyright in this thesis. Neither the thesis nor substantial extracts from it may be printed or otherwise reproduced without the author's permission.**

**L'auteur a accordé une licence non exclusive permettant à la Bibliothèque nationale du Canada de reproduire, prêter, distribuer ou vendre des copies de cette thèse sous la forme de microfiche/film, de reproduction sur papier ou sur format électronique.**

**L'auteur conserve la propriété du droit d'auteur qui protège cette thèse. Ni la thèse ni des extraits substantiels de celle-ci ne doivent être imprimés ou autrement reproduits sans son autorisation.**

0-612-65735-3

**Canada**

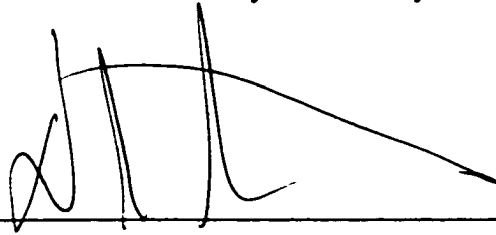
# Table of Contents

Table of Contents.....	i
The Examining Committee.....	iv
Acknowledgements.....	v
Abstract.....	vi
List of Tables.....	vii
List of Figures.....	viii
List of Copyrighted Material.....	x
 Chapter 1. Introduction.....	 1
1.1 Asteroseismology and Helioseismology.....	1
1.2 Diagnostic Power of Astero/Helioseismology.....	2
1.2.1 Solar Non-radial Oscillations.....	3
1.2.2 Convection Zone.....	5
1.2.3 Solar Tachocline.....	7
1.2.4 Helium Abundance.....	7
1.2.5 Solar Neutrinos and Neutrino Physics .....	8
1.3 Thesis Goals and Purpose.....	8
1.4 Observational Asteroseismology.....	11
1.4.1 Observational Methods: Photometry.....	11
1.4.2 Observational Methods: Doppler-Shift/Velocity Measurements.....	15
1.4.3 Observational Methods: Balmer Line Equivalent Widths.....	17
1.5 Scaling Solar Oscillations.....	18
1.6 Successful and Failed Non-radial Oscillation Observations.....	19
1.6.1 Arcturus ( $\alpha$ Boo).....	20
1.6.2 Procyon ( $\alpha$ CMi).....	21
1.6.3 $\alpha$ Cen A.....	24
1.6.4 $\eta$ Boo.....	29
1.6.5 $\alpha$ Ursae Majoris ( $\alpha$ UMa).....	35
1.6.6 M67.....	37
1.7 Seismology in Space.....	38
1.7.1 MOST (Microvariability and Oscillations of STars).....	39
1.7.2 MONS (Measuring Oscillations in Nearby Stars).....	40
 Chapter 2. Theory and Model Description.....	 41
2.1 Fundamental Principles.....	41

2.2	Linear Theory.....	44
2.2.1	Lamb and Brunt-Väisälä Frequencies.....	42
2.2.2	General Definitions of $p$ , $g$ , & $f$ -modes.....	47
2.2.3	Turning/Reflection Points.....	48
2.2.4	Acoustic Cutoff.....	52
2.3	Asymptotic Theory.....	53
2.3.1	Asymptotic Formula for $p$ -modes.....	54
2.4	Driving / Excitation Mechanisms.....	56
2.4.1	$\epsilon$ Mechanism.....	57
2.4.2	$\kappa$ Mechanism.....	57
2.4.3	Five-Minute Oscillations: Turbulent Convection.....	58
2.5	Yale Stellar Evolution Code with Rotation: YREC.....	60
2.5.1	Opacities.....	61
2.5.2	Diffusion.....	61
2.5.3	Convection.....	61
2.6	The Pulsation Code.....	63
Chapter 3. $\epsilon$ Eridani.....		65
3.1	Magnitude, Colours, and Parallax.....	65
3.2	Effective Temperature, Surface Gravity, and Metallicity.....	66
3.3	Bolometric Correction and Luminosity.....	67
3.4	Mass.....	70
3.5	Seismology: Age and Mixing Length Parameter.....	71
3.6	Stellar Evolution Models.....	74
3.7	Pulsation Model Results.....	80
Chapter 4. $\beta$ Hydri.....		92
4.1	Magnitude, Colours, and Parallax.....	92
4.2	Effective Temperature, Surface Gravity, and Metallicity.....	93
4.3	Bolometric Correction and Luminosity.....	95
4.4	Mass and Age.....	95
4.5	Previous Seismology.....	99
4.6	Stellar Evolution Models.....	102
4.7	Seismological Results.....	107
Chapter 5. $\beta$ Geminorum.....		117
5.1	Observational Parameters.....	117
5.2	Photospheric Parameters.....	118
5.3	Mass and Evolutionary Status.....	120
5.4	Stellar Evolution Models.....	122
5.5	Seismology Results.....	124

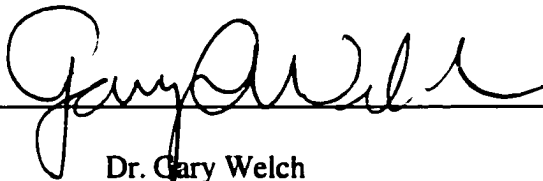
Chapter 6. Summary and Discussion.....	135
6.1 $\epsilon$ Eridani.....	135
6.2 $\beta$ Hydri.....	136
6.3 $\beta$ Geninorum.....	137
6.4 General Conclusions.....	138
References.....	143
Curriculum Vitae.....	153

Certificate of Examination  
Department of Astronomy and Physics  
Saint Mary's University



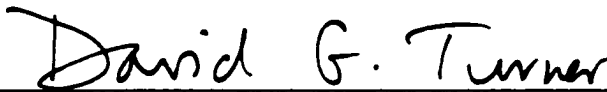
---

Dr. David Guenther  
Associate Professor of Astronomy and Physics  
Saint Mary's University  
(Thesis Supervisor)



---

Dr. Gary Welch  
Associate Professor of Astronomy and Physics  
Saint Mary's University



---

Dr. David Turner  
Professor of Astronomy and Physics  
Saint Mary's University



---

Dr. Pierre Demarque  
Professor Emeritus  
~~Astronomy and Physics~~  
Yale University  
(External Reader)



## **Acknowledgements**

A thesis this thick certainly does not get accomplished by one person. There were many contributors of both the scientific and moral variety. First and foremost I'd like to thank my supervisor, Dr. David Guenther for his intelligence and expertise. He ruled with an "Iron Fist" and everything he had to say was encouraging and insightful. A thank you goes to my examining committee: Dr. David Turner, Dr. Gary Welch, and Dr. Pierre Demarque (external) whose editing skills and scientific input were of great value. Thank you to the entire Saint Mary's astronomy and physics department.

This work would not have been possible without the support of family and friends. Thanks Sarah for listening to my astrophysical mumbo-jumbo and your continuing support and caring, and Dan and Dave O. for your sarcasm and insults. To Sandro for convincing me to go to the pub instead of working, but never coming when I invited him. To Kevin, Dave M., and Ray for the poker and hockey games. Thank you Andrew for suffering with me and the conversations that had nothing to do with astronomy. Thank you especially to Harold and his truck, and the love and support of Mom, Dad, and Paul.

# **Abstract**

Stellar evolution models and their associated non-radial pulsation spectra are presented for the nearby stars  $\epsilon$  Eridani (K2 V),  $\beta$  Hydri (G2 IV),  $\beta$  Geminorum (K2 III). This analysis was performed in preparation for the future observations of these (and other) stars by the MOST and MONS space missions. These missions will be able to identify non-radial oscillations on a variety of stars. This work is an uncertainty analysis of the oscillation spectra. These results represent the latest stellar evolution models and asteroseismological analyses of the three stars, and include a possible age indicator for  $\epsilon$  Eridani, the effects of mode bumping during subgiant evolution, and a possible mass refinement for  $\beta$  Gem. This work also includes a brief review of the observational techniques used to detect non-radial oscillations on distant stars, and of previously successful and failed seismology observations.

# List of Tables

Table 3.1	Observational Parameters of $\epsilon$ Eridani.....	65
Table 3.2	Colour Correction Data and Interpolation Parameters.....	68
Table 3.3	Results of Bolometric Correction Interpolation.....	70
Table 3.4	Model Input Parameters of Guenther and Demarque (1986) and Soderblom and Däppen (1989) for $\epsilon$ Eridani.....	71
Table 3.4	Stellar Model Characteristics of Guenther and Demarque (1986) and Soderblom and Däppen (1989) for $\epsilon$ Eridani.....	73
Table 3.6	Summary of Model Parameters for $\epsilon$ Eridani (this work).....	74
Table 3.7	Diffusion Model Evolution and Pulsation Output for $\epsilon$ Eridani.....	78
Table 3.8	Linear Regression Results of Small Spacing vs. Age.....	88
Table 4.1	Required Parameters for Bolometric Correction Interpolation.....	95
Table 4.2	Results of Bolometric Correction Interpolation.....	95
Table 4.3	Difference in Stellar Parameters Due to Different Parallaxes.....	98
Table 4.4	Model Information from Dravins <i>et al.</i> (1998).....	99
Table 4.5	Stellar Evolution Parameters for $\beta$ Hydri (this work).....	102
Table 4.6	Diffusion Model Evolution and Pulsation Output for $\beta$ Hydri.....	105
Table 5.1	Observational Parameters for $\beta$ Gem from Hipparcos Catalogue.....	118
Table 5.2	Summary of Pollux's ( $\beta$ Gem) Chromospheric Parameters.....	119
Table 5.3	Stellar Evolution Parameters for $\beta$ Gem (this work).....	122
Table 5.4	Non-diffusion Model Properties for $\beta$ Gem.....	125
Table 5.5	Large Spacing Data for $\beta$ Gem.....	126

# List of Figures

Figure 1.1	Disk Integrated Solar Power Spectrum.....	4
Figure 1.2	Degree – Frequency Diagram.....	6
Figure 1.3	Power Spectra of Simulated Time series for Various Integration Times.....	14
Figure 1.4	Several $l = 1$ p-mode Frequencies for and Evolving Solar Mass Star.....	28
Figure 1.5	Power Spectrum of Equivalent Width Measurements for $\eta$ Boo.....	30
Figure 1.6	Comb Response of the Power Spectrum of $\eta$ Boo.....	31
Figure 2.1	Contour Plots of Several Spherical Harmonics.....	43
Figure 2.2	Schematic of a Propagation Diagram for a Polytrope of Index 4.....	46
Figure 2.3	Schematic Acoustic Wave Propagation for Various Modes.....	49
Figure 2.4	Simulated Eigenfunctions for Selected p-modes.....	50
Figure 2.5	Simulated Eigenfunctions for Selected g-modes.....	51
Figure 3.1	Model Tree for Simplifying Model Descriptions.....	76
Figure 3.2	Selected Evolutionary Models for $\epsilon$ Eridani.....	77
Figure 3.3	Large Frequency Spacing as a Function of Radial Order for $\epsilon$ Eridani.....	81
Figure 3.4	Same as Figure 3.3 but for the Non-diffusion Models.....	82
Figure 3.5	Relationship Between the Large Frequency Spacing and Stellar Radius for $\epsilon$ Eridani.....	84
Figure 3.6	Small Frequency Spacing Variations with Age for Selected Diffusion Models of $\epsilon$ Eridani.....	86
Figure 3.7	Same as Figure 3.6 but for the Non-diffusion Models.....	87
Figure 3.8	Propagation Diagram for a selected $\epsilon$ Eridani Model.....	90

Figure 3.9	Eigenfunction for an $l = 20$ mode for $\epsilon$ Eridani.....	91
Figure 4.1	Variations in Evolution of $\beta$ Hydri Due to Different Parallaxes.....	97
Figure 4.2	Power Spectrum of Oscillations Obtained for $\beta$ Hydri.....	101
Figure 4.3	Stellar Evolution Models for $\beta$ Hydri.....	103
Figure 4.4	Mode Bumping Affects in Evolved Stars ( $\beta$ Hydri).....	108
Figure 4.5	Large Frequency Spacing vs. Radial Order for Diffusion Models of $\beta$ Hydri.....	109
Figure 4.6	Same as Figure 4.5 but for Harmonic Degree $l = 1$ .....	111
Figure 4.7	Small Frequency Spacing Relation with Age for $\beta$ Hydri.....	113
Figure 4.8	Propagation Diagram for the Subgiant $\beta$ Hydri.....	114
Figure 4.9	An $l = 4$ Eigenfunction for a $\beta$ Hydri Model.....	116
Figure 5.1	Nine of 27 Evolutionary Tracks (Models) for $\beta$ Gem.....	123
Figure 5.2	Propagation Diagram for the Giant Star $\beta$ Gem.....	128
Figure 5.3	An Eigenfunction for an $l = 3$ $\beta$ Gem Mode.....	129
Figure 5.4	Eigenfunction for an $l = 40$ $\beta$ Gem Mode.....	131
Figure 5.5	Large Frequency Spacing as a Function of Radial Order for $\beta$ Gem.....	132
Figure 5.6	Large Frequency Spacing vs. Age for $\beta$ Gem.....	133
Figure 6.1	General Variation of Lamb Frequencies Between Stars of Different Evolutionary Status.....	139
Figure 6.2	General Variation of the Brunt-Väisälä Frequency with Stellar Evolution.....	140
Figure 6.3	General Behaviour of the Large Frequency Spacing with Stellar Evolution.....	142

# List of Copyrighted Material

All of the following are used with permission.

Christensen-Dalsgaard, J. 1998:	Figure 1.3 Figure 2.1 Figure 2.3 Figure 2.4 Figure 2.5
Toutain and Fröhlich 1922:	Figure 1.1
Duvall <i>et al.</i> 1988:	Figure 1.2
Guenther and Demarque 2000:	Figure 1.4
Kjeldsen <i>et al.</i> 1995:	Figure 1.5 Figure 1.6
Bedding <i>et al.</i> 2001:	Figure 4.2
Green <i>et al.</i> 1987:	Table 3.2
Guenther & Demarque 1986, and Soderblom & Däppen 1989:	Table 3.4
Dravins <i>et al.</i> 1998:	Table 4.4
Drake and Smith 1991:	Table 5.2

# Chapter 1

## Introduction

### 1.1 Asteroseismology and Helioseismology

Although still in its infancy, asteroseismology, the study of stellar interiors via global oscillations, has proven to be a powerful diagnostic tool of stellar structure and theory. Asteroseismology has its foundations in helioseismology, the study of oscillations in the Sun (§ 1.2.2), with the only difference being that stellar oscillations are not spatially resolved.

Non-radial oscillations in the Sun were first observed by Leighton, Noyes, and Simon (1962). They discovered that certain regions of the Sun's surface were moving up and down with a velocity on the order of  $15 \text{ cm s}^{-1}$ , or a period of about 5-minutes. The phenomenon was first believed to be related to turbulent convection (§ 2.4.3, and later it was suggested (correctly) that the oscillations were trapped acoustic waves (Ulrich 1970, Leibacher and Stein 1971). The trapped pressure,  $p$ -modes manifest themselves as non-radial oscillations on the solar surface, an observed global phenomenon, and are the result of the superposition of millions ( $\sim 10^7$ ) of distinct  $p$ -modes.

Linear oscillation theory (Chapter 2) predicts a dependence of the frequencies on the horizontal wavelength of the oscillation (see Figure 1.2), and that was confirmed by Deubner (1975). It was this discovery that led to the realization that acoustic waves

carry physical information about the solar (stellar) interior and helioseismology (asteroseismology) was born.

The rapid rate of the development of asteroseismology, both theoretical (Chapter 2) and observational (§ 1.4), has led to the development of promising space-based observing missions. Two in particular, MOST (**M**icrovariability and **O**scillations of **S**Tars; Matthews *et al.* 2000) and MONS (**M**easuring **O**scillations of **N**earby **S**tars; Kjeldsen, Bedding, and Christensen-Dalsgaard 2000), have target stars that are presented in this thesis (discussed in more detail in § 1.3 and § 1.7). Each mission will be able to measure many frequencies for modes of low harmonic degree on a variety of stars.

## **1.2 Diagnostic Power of Astero/Helioseismology**

A more explicit description of the benefits of asteroseismology is given in Chapter 2, and in § 1.6 which gives a brief review of successful and failed oscillation observations for stars other than the Sun. Observations will reveal frequency spacings in the power spectrum that are directly related to the mass, radius, and state of evolution of the star.

The best and most detailed example of the power of non-radial oscillations are the results obtained for the Sun. There are many well documented reviews about helioseismology (Cox 1976; Deubner and Gough 1984; Gough and Toomre 1991; Harvey 1995; Demarque and Guenther 1999), and this section is designed to be a brief look at what we have learned so far (information in the following sections, except § 1.2.1, is taken primarily from Demarque and Guenther 1999).



### 1.2.1 Solar Non-radial Oscillations

In almost any current review article about helioseismology, one is sure to find a graph of the disk-integrated power spectrum of the Sun. The power spectrum is a plot of the way the intensity of the frequency of the signal vary with frequency, and is usually obtained from a Fourier transform of the signal. One such example is shown in Figure 1.1, taken from Toutain and Fröhlich (1992). The data were taken with the IPHIR full disk photometer while heading to Mars. What is displayed is the full time-series analysis of 160 days of observations.

The most prominent features of the power series are the well defined frequencies and mode amplitudes that are large only between 2500 and 4000  $\mu\text{Hz}$ . Within this range the frequencies are evenly spaced and modes ( $l = 0, 2$  or  $l = 1, 3$ ) are separated by about 68  $\mu\text{Hz}$ . This bodes very well for asymptotic theory (§ 2.3) which predicts the separation to be  $\sim 67 \mu\text{Hz}$  (Christensen-Dalsgaard 1998).

The ability to resolve the solar disk allows for measurements of modes with high harmonic degree. If observations were not able to resolve the stellar disk, then only a few frequencies would have been observed because the oscillations suffer from cancellation effects across the solar disk. For the Sun modes as high as  $l \sim 3000$  (the number of nodes on the solar surface),  $n \leq 26$  (the number of nodes along a radial path to the solar centre), and  $\nu \sim 1600 - 6000 \mu\text{Hz}$  (frequency of the oscillation) have been observed. It is the large number of frequencies which make it possible to infer the structure and dynamics of the solar interior. For stars in general, the more frequencies observed, the better one will be able to constrain the star's physical parameters.

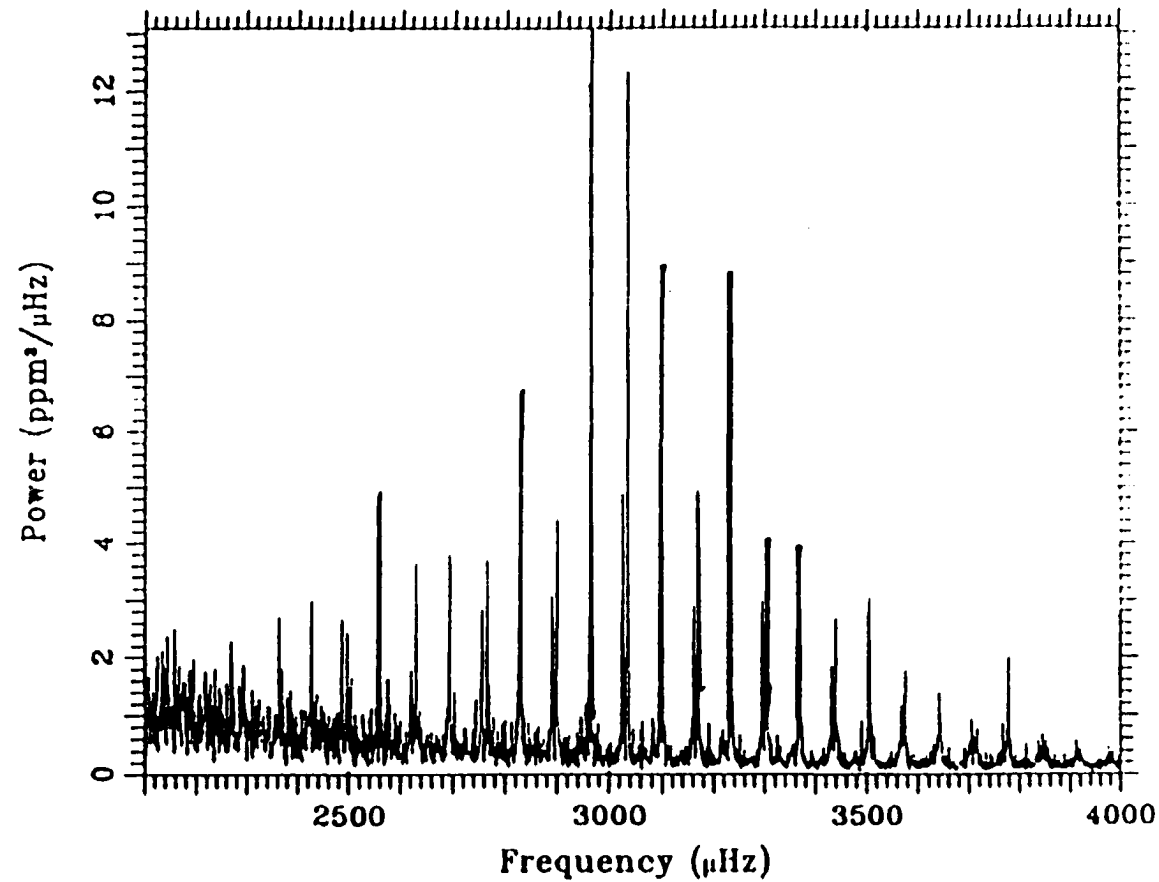


**Figure 1.1** Power spectrum of the Sun from the entire time series of disk integrated light of 160 days observing length. Note the very defined *p*-mode frequency spacings and frequency maxima (Toutain and Fröhlich 1992).

The data for the observed solar modes are best displayed in a  $l$ - $\nu$  (harmonic degree – frequency) diagram, shown in Figure 1.2 (from Duvall *et al.* 1988). The first plot of this kind was done by Deubner (1975), and it was at that time researchers recognized the probing potential of non-radial oscillations. Most of the power (in the figure) is concentrated in the ridges (data points) for the observed  $p$ -mode oscillations. The data are fully consistent with the mode-trapping of acoustic wave hypothesis (Ulrich 1970; Toomre 1970; Leibacher and Stein 1971). With these results researchers were able to recover an accurate description of the solar interior. Some of the discoveries are discussed below.

### 1.2.2 Convection Zone

The depth of the solar convection zone has ramifications for every aspect of the structure of the solar interior and solar evolution. Besides providing a better understanding of the convection phenomenon itself, an accurate determination of the convective region, in combination with the Sun's known physical parameters, can constrain physical models of the deep stellar interior.

Using helioseismic inversion (retrieving physical parameters from many observed  $p$ -mode frequencies) to map out the variation in sound speed with depth, Christensen-Dalsgaard *et al.* (1991) and Basu (1997) were able to pinpoint the location of the base of the convection zone to  $r/R_{\odot} = 0.713 \pm 0.003$ .

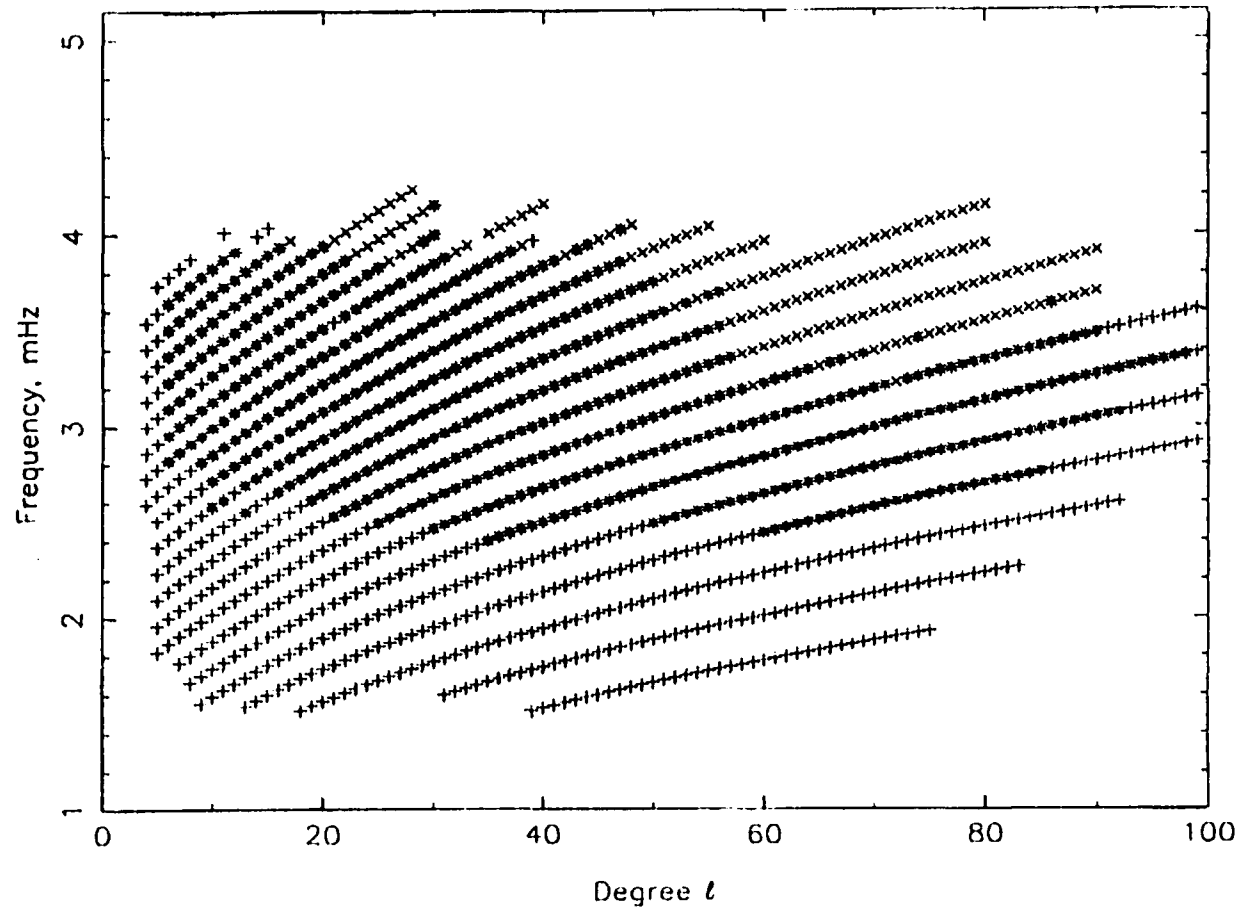


**Figure 1.2**  $l - \nu$  diagram displaying the power concentration on the Solar surface. The different symbols represent data obtained from two different sites. Lowest frequency ridge consists of  $p$ -mode oscillations with radial order  $n = 3$ , and the ordinate is in milli-Hertz (Duvall *et al.* 1988).

### 1.2.3 Solar Tachocline

The Tachocline is a thin region near the base of the convection zone where the rotation becomes independent of latitude (Spiegel and Zahn 1992). It is in this area that the solar dynamo, that controls the solar activity, is believed to be anchored. Understanding solar activity is of great importance to the commercial (and scientific) world.

Inversions of the low degree ( $l = 0, 1, 2, 3$ )  $p$ -mode rotational splitting, arising from the Doppler effect, reveal the differential rotation of the solar interior. At the base of the convection zone there is a discontinuity in the rotation rate where the solar interior transports energy radiatively (much study was done by Basu 1997; and Basu and Antia 1998).

### 1.2.4 Helium Abundance

Because of the Sun's low effective temperature, spectroscopic observations of the solar photosphere will not display any helium lines. The best way to infer a helium abundance of the solar interior, until recently, has been with stellar evolutionary models (Guenther *et al.* 1992a). Their models give the mass fraction of helium to be about,  $Y_{\text{initial}} \approx 0.275$ .

Helioseismic inversions now allow for the determination of the helium abundance in the convective zone (Basu and Antia 1995). The work of Richard *et al.* (1998) recently obtained  $Y = 0.248 \pm 0.002$ , thus supporting conclusions that there is helium diffusion in the solar interior (Bahcall *et al.* 1997).

### **1.2.5 Solar Neutrinos and Neutrino Physics**

In quest of a solution to the solar neutrino problem there lies three possible answers: 1. the physics of the Standard Solar Model (SSM) is not complete; 2. our knowledge of neutrino physics is lacking; or 3. a combination of the two.

Helioseismology has eliminated the first possible explanation, since the agreement between the observed  $p$ -mode frequencies and the SSM with helium and heavy element diffusion is very good. Thus, because the physics of the current standard solar model are well understood, it is our knowledge of neutrino physics which is incomplete (Bahcall *et al.* 1997; Guenther and Demarque 1997).

Other notable results include: new information about the structure of the superadiabatic transition layer (Nordlund and Stein 1996); solar age determination (Guenther and Demarque 1997); and a constraint on varying-G cosmologies (Guenther, Krauss, and Demarque 1998). The discoveries noted here are the result of high precision data acquisition and the ability to resolve the solar disk. Such resolution allows for frequencies of high degree to be observed, and it is inversions of the high degree modes which led to the above conclusions. The findings of seismological observations on distant stars is less detailed (for now) and are discussed in § 1.6.

## **1.3 Thesis Goals and Purpose**

The recent excitement over future space-based telescopes, designed for collecting seismology information, is the motivation behind the work presented here. The solar-type targets of the MOST (§ 1.7.1) and MONS (§ 1.7.2) missions are of particular interest for asteroseismology. It is hoped that successful observations will be able to answer a

number of questions related to stellar structure and evolution: Where is the border between stars with and without a convective core? When/where does core hydrogen fusion end and hydrogen-shell fusion begin? (Kjeldsen and Bedding 2000).

There is also the possibility of accurately measuring stellar ages; the best chance of this is to obtain low-noise data so as to determine an average small frequency spacing (Chapter 2), thus restricting observing bright, nearby stars. The significance of the small frequency spacing is that it is directly related to the composition of the core. Of course, the observations will be useful for testing the details and theory of stellar models. Much remains to be learned about turbulent mixing, diffusion, magnetic fields, convection, and rotation (Kjeldsen and Bedding 2000).

The positive identification of oscillation frequencies, and large and small frequency spacings alone will not determine (or refine) the physical parameters and structure of stars. Theoretical stellar models must be used with the observed frequencies to study the properties of the star. It is the generation of such stellar models and their pulsation spectra that is accomplished in the thesis. The thesis is an uncertainty analysis (except systematic) of the evolutionary state and non-radial pulsation spectrum of three stars in various stages of evolution. The models are generated to cover the range of the observational uncertainties for the selected target stars.

After the MOST and MONS satellites are operational for about a week, the satellites will have observed a power envelope for the target star. Shortly after a week the large and small frequency spacings will be determined, followed by the identification of individual frequencies. Longer integration times (~ month) will then reveal amplitude and phase information.

On the basis of their assumed state of evolution and past observations, I have generated models for  $\epsilon$  Eridani (K2 V; MOST and MONS; Chapter 3),  $\beta$  Hydri (G2 IV; MONS; Chapter 4), and  $\beta$  Geminorum (Pollux K0 III; MOST; Chapter 5). Each of the stars is bright and nearby, but the uncertainties in their physical parameters are still large. To account for that I generated a large grid of models to obtain the maximum spread in parameter space for each star. As explained in more detail in chapters 3-5, the models are evolved varying only one parameter at a time (either mass, composition, luminosity, or effective temperature) for each case of diffusion or non-diffusion of helium and heavy elements ( $\beta$  Gem models were all non-diffusion). The reason for the two sets of models is to test the dependency of the  $p$ -mode spectrum to elemental diffusion, thus helping to constrain the surface composition.

Since only one parameter at a time is varied (to observe any frequency dependence for that parameter), the models are not evolved to their respective error box extremes (see Figure 3.2 as an example). However, to first order, a simple linear interpolation (Pythagorean theorem) can be made with the model results to calculate the extremities of the  $p$ -mode oscillation uncertainties.

As just stated, for each stellar model a non-radial, non-adiabatic pulsation spectrum was generated. It is the tables of data along with their stellar structure information and observations which will yield a wealth of information. The amount and quality of information that can be interpolated depends entirely on the number of modes observed for the star; obviously, the more modes observed the better we can refine the stellar structure. Even a few observed large frequency spacings for the low  $l$  (0, 1, 2) modes will result in a more accurate determination of the star's mass and radius.



Of specific interest is the evolutionary state of the stars that were modeled. This work studies, in detail, how the pulsation spectrum changes for stars in different stages of evolution; main-sequence dwarf, subgiant, and giant branch stars. These findings are summarized in Chapter 6.

Unfortunately, time did not allow for the generation of results for any more target stars. However, should there be a need, this thesis can be used as a guide or methodology for the rigorous modeling of any star. Much of the methodology used in this thesis is analogous to the work done by Guenther and Demarque (1993, 1996, and 2000) in generating stellar evolution models and pulsation spectra for Procyon,  $\eta$  Boo, and  $\alpha$  Cen AB, respectively.

## **1.4 Observational Asteroseismology**

This section will discuss the ground-based techniques used for observing non-radial oscillations on distant stars, and the transition to space-based observations. Also included is a section describing what is expected to be found with observations from scaling the solar pulsation spectrum.

### **1.4.1 Observational Methods: Photometry**

Stars other than the Sun are spatially unresolved in most observing instruments (they are point sources). That limits the observable oscillations to modes of low harmonic degree,  $l \leq 3$ . The higher degree modes approximately average out from the integrated positive and negative fluctuations over the stellar disk.

To optimize the interpretation of the photometric data, the methods used should be sensitive only to the modes of low  $l$ . The objective is then to get time strings from a few oscillations so their frequencies can be retrieved by a discrete Fourier analysis over time (Christensen-Dalsgaard 1998). The optimal method is to observe the intensity fluctuations with integrated-light (whole-disk) photometry. The optimal instrument of choice is then a CCD, for differential CCD photometry.

Intensity oscillations on a star can be written in the form,

$$I(\theta, \phi; t) = \sqrt{4\pi} \operatorname{Re} \left\{ I_0 Y_l^m(\theta, \phi) e^{-i(\omega_0 t - \delta_0)} \right\} \quad (1.01)$$

where  $I_0$  is an intensity constant,  $Y_l^m$  is the spherical harmonic, the terms in the exponent describe the oscillatory time dependence, and we are only concerned with the real part of the complex function. The response in whole-disk observations is obtained as the average over the stellar disk,

$$I(t) = S_l^{(l)} I_0 \cos(\omega_0 t - \delta_0) \quad (1.02)$$

where the spatial response function,  $S_l^{(l)}$ , over the stellar disk is

$$S_l^{(l)} = 2\sqrt{2l+1} \int_0^{\pi/2} P_l(\cos \theta) \cos \theta \sin \theta d\theta \quad (1.03)$$

which can be calculated directly by integration for low  $l$ , or by a recursion otherwise. The required predicted precision is  $\sim 20 - 50 \mu\text{mag}$ , or  $\delta I/I \sim 1.5 \times 10^{-6}$  (Kjeldsen and Bedding 1995). The background noise for intensity observations of the Sun is about  $\delta I/I \sim 0.14$ , and the present sensitivity is about a tenth of a magnitude (Harvey 1988).

The advantages, or benefits, of photometric observations are: 1. detectable oscillations do not require sharp stellar spectrum lines, which implies the measurements

are independent of stellar rotation; and 2. photometric methods have the potential for micromagnitude accuracy and can even be used on faint stars (Brown and Gilliland 1994). This is the method that will be employed by many of the future space missions, and specifically by both the MOST and MONS missions.

Assume for the moment one wanted to perform ground-based observations; the fundamental limiting noise source is atmospheric scintillation:

$$\delta I/I = (0.09 D^{-2/3} X^{1.75} e^{-h/h_o}) / \sqrt{2 t_{\text{int}}} \quad (1.04)$$

with  $\delta I/I$  being the rms noise in the measured relative intensity,  $D$  is the telescope aperture in cm,  $X$  is the airmass,  $h$  is the altitude,  $h_o$  is the atmospheric scale height, and  $t_{\text{int}}$  is the exposure time in seconds (Young 1967; 1993).

Equation 1.04 illustrates the underlying reason why photometric searches must be performed in space. Observations from anywhere on the Earth will result in a high relative intensity error. One must have a large collecting area on the top of a mountain and be able to observe for weeks on end.

The reason for the long observing time requirements is shown in Figure 1.3 (Christensen-Dalsgaard 1998). This figure is a simulation of a time series where the target has multiple observations. The plots clearly display why longer integration times are required; short observing times are severely under-sampled. By any feasible standards weeks of uninterrupted integration time is not possible from the ground, and any such long-term observations are limited by interrupted viewing. Therefore, like many branches of astronomy, photometric searches for non-radial oscillations should be space-based. It is only in space that there is the possibility of obtaining the desired  $\mu\text{mag}$

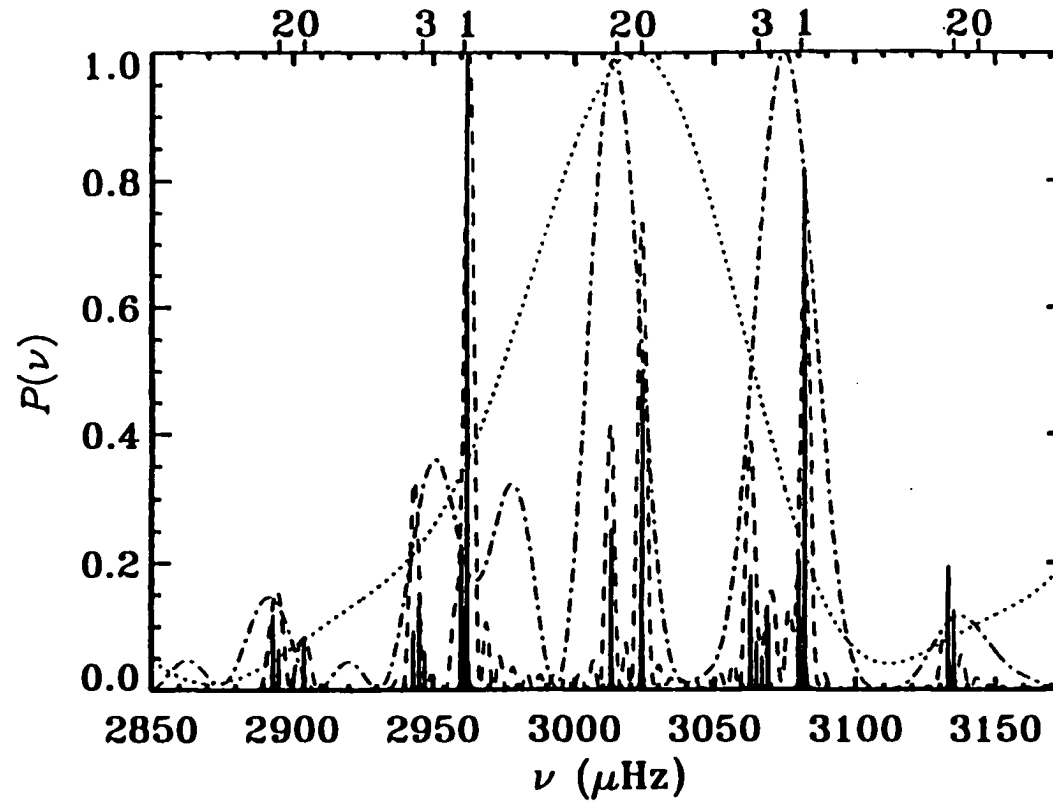


**Figure 1.3** Power spectra of simulated time series of duration 600 h (—), 60 h (---), 10 h (.....), and 3 h (-.-.-). The power is on an arbitrary scale and has been normalized to a maximum value of 1. The location of the central frequency for each group of rotationally split modes, as well as the value of the degree, are indicated on the top of the diagram (Christensen-Dalsgaard 1998).

precision predicted by scaling from the solar case (see § 1.5, Kjeldsen and Bedding 1995).

#### 1.4.2 Observational Methods: Doppler-Shift, Velocity Measurements

Another method to obtain a star's pulsation properties is through observing velocity oscillations by measuring the Doppler shift of spectral lines. The Doppler shifts are a result of the influence of the oscillations on the photospheric gases. Such observations are only sensitive to the line-of-sight component of velocity. Hence, such observations are sensitive to low degree modes with periods less than an hour whose velocity is approximately in the radial direction. Similar to equation 1.01, the velocity of the oscillation can be written as,

$$V(\theta, \phi; t) = \sqrt{4\pi} \operatorname{Re} \left[ V_o Y_l^m(\theta, \phi) e^{[-i(\omega_o t - \delta_o)]} \mathbf{a}_r \right] \quad (1.05)$$

where  $\mathbf{a}_r$  is the unit vector in the radial direction. Whole-disk Doppler velocity observations can then be written as,

$$v(t) = S_l^{(v)} V_o \cos(\omega_o t - \delta_o) \quad (1.06)$$

where  $S_l^{(v)}$  is the velocity response function that takes into account the projection of the velocity onto the line-of-sight (Christensen-Dalsgaard 1998):

$$S_l^{(v)} = 2\sqrt{2l+1} \int_0^{\pi/2} P_l(\cos \theta) \cos^2 \theta \sin \theta \, d\theta \quad (1.07)$$

The work done by ground-based instruments using the Doppler-shift method has a few advantages over photometry for detecting the very small oscillations amplitudes. For example, the velocity method results in a large contrast between the pulsation signal and the convective noise from the star (Christensen-Dalsgaard and Frandsen 1988), thus

implying a better signal-to-noise ratio. Second, because of the nearly radial propagating property of the velocity oscillations, motion near the stellar limb is orthogonal to the line-of-sight and does not contribute to the velocity data. Doppler shift measurements then have a smaller surface for spatial averaging and result in readily detectable  $l = 3$  modes in the velocity data (Peri 1995). The required precision in the wavelength shifts are  $\delta\lambda/\lambda \sim 10^{-10}$ . This can also be seen from Eq. 1.07 and arises from the extra  $\cos\theta$  term (as compared to Eq. 1.03). Presently it is possible to obtain velocity measurements  $\sim \text{cm s}^{-1}$ , but the desired sensitivity is to be able to detect velocity measurements  $\sim 15 \text{ cm s}^{-1}$  (Harvey 1988).

The Doppler method is also sensitive to the rotation of the star (unlike photometry), which can be seen as line-splitting in the spectra. If many modes can be observed, the line splitting allows for the detection and the interpretation of internal rotation. Interpretation of the velocity data must then take into account such splitting.

However, accurate measurements of the small wavelength shifts ( $\delta\lambda/\lambda \sim 10^{-10}$ ) require high spectral resolution (sharp line profiles), low background and instrumental noise, and bright nearby sources (Brown and Gilliland 1994). There is a fundamental limit to the precision of the obtainable data using this technique; it results from photon counting statistics (Brown 1990) and is formulated by,

$$\delta v_{rms} = \frac{cw}{\lambda d (N_{pix} N_{lines} I_c)^{1/2}} \quad (1.08)$$

where  $c$  is the speed of light,  $w$  is the width of the spectrum line which includes any (instrumental, stellar) line broadening process,  $\lambda$  is the central wavelength,  $d$  is the fractional line depth,  $N_{pix}$  is the number of wavelength samples obtained across the line

width,  $N_{lines}$  is the number of spectral lines observed, and  $I_c$  is the continuum intensity in the measurement expressed as the number of detected photons. For the solar  $p$ -modes the background noise is  $\sim 330 \text{ m s}^{-1}$  (Harvey 1988). The most promising instrument for velocity measurements is an echelle spectrograph (Brown and Gilliland 1994; Peri 1995). The instrument provides high resolution over a broad range of wavelengths, resulting in the simultaneous measurement of hundreds or thousands of lines. The Doppler-shift method, like photometry, suffers from interrupted viewing which adds aliases to the data. Ground-based Doppler-shift measurements have the potential to detect stellar non-radial oscillations if a long integration time is used. However, conclusive evidence of non-radial oscillations has yet obtained with that method.

#### 1.4.3 Observational Methods: Balmer Line Equivalent Widths

This is a relatively new method developed by Kjeldsen *et al.* (1995). Like differential photometry, the method exploits the fact that stellar oscillations affect the temperature of the stellar surface. Hence the temperature fluctuations are measured via changes in the equivalent widths of the Balmer lines. Model atmosphere calculations (Kurucz 1979) give the change in width with temperature to be approximately:

$$\delta w/w \approx 6 \delta T/T \quad (1.09)$$

The change in equivalent width is measured in parts per million (ppm).

The successful application of the method could lead to a surge of oscillation measurements from the ground because such measurements are insensitive to atmospheric scintillation. The acquisition of data is hampered only by photon noise, and only moderate spectral resolution is required. That improves the signal-to-noise ratio and

does not require extreme instrumental stability. Observations of this type, though, will work best only for isolated bright stars.

## 1.5 Scaling Solar Oscillations

Before discussing examples of the aforementioned observing techniques, I will take a moment to discuss what is expected from stars other than the Sun. Solar type stars are believed to oscillate in a similar fashion to the Sun, and that leads to the possibility of predicting stellar pulsation properties by scaling the effects of solar pulsation. There have been thorough derivations of the scaled pulsation equations (Christensen-Dalsgaard and Frandsen 1983; Edmonds *et al.* 1992; Kjeldsen and Bedding 1995) and the results summarized below are taken primarily from Kjeldsen and Bedding (1995, hereafter KB95).

The large frequency spacing,  $\Delta\nu_o$ , is the difference between frequencies adjacent in radial order  $n$  (refer to § 2.3.1). It is directly proportional to the square root of the mean density of the star (134.9  $\mu\text{Hz}$  is the solar value determined observationally):

$$\Delta\nu_o = \frac{(M/M_{sun})^{1/2}}{(R/R_{sun})^{3/2}} \times 134.9 \mu\text{Hz} \quad (1.10)$$

The solar oscillations have a maximum power at a frequency,  $\nu_{\max}$ , of about 3000  $\mu\text{Hz}$ . Using that value and the notion that  $\nu_{\max}$  should scale with the acoustic cutoff frequency (§ 2.2.4; Brown *et al.* 1991),  $\nu_{ac}$  (Eq 2.12), one estimates that for a particular star:

$$\nu_{\max} = \frac{M/M_{sun}}{(R/R_{sun})^2 \sqrt{T_{eff}/5777(\text{K})}} 3050 \mu\text{Hz} \quad (1.11)$$



For the Sun, maximum power is observed for modes with radial order  $n \equiv 21$ . That information and Equation 1.11 yield an approximate radial order of maximum power:

$$n_{\max} \equiv \left( \frac{M/M_{\text{sun}}}{(T_{\text{eff}}/5777\text{(K)})(R/R_{\text{sun}})} \right)^{1/2} \times 22.6 - 1.6 \quad (1.12)$$

Another useful quantity is the velocity of the oscillations,

$$v_{\text{osc}} = \frac{L/L_{\text{sun}}}{M/M_{\text{sun}}} \times (23.4 \pm 1.4 \text{ cm/s}) \quad (1.13)$$

where the dependence of the oscillation amplitudes to the luminosity and mass were shown in models by Christensen-Dalsgaard and Frandsen (1983). The above equation assumes the star's driving mechanism (convection zone turbulence) is analogous to the solar case. The fundamental understanding of the driving mechanism(s) is not complete, so the above equation should be used with some caution.

Note that only the mass, radius, and effective temperature of the star (in solar units) are required for the predictions. The scaled values for any star should be used as an approximation only and can be subject to large uncertainties if the stellar properties are not accurately known.

## 1.6 Successful and Failed Non-radial Oscillation Observations

Observational asteroseismology is based on the assumption that there exist discrete frequencies on stars other than the Sun. Theoretical considerations and scaling from the solar case predict promising and accurate results for Sun-like stars (Christensen-Dalsgaard 1983, KB95). Sun-like stars are stars on or near the main-sequence with relatively shallow convective zones so as to generate  $p$ -mode oscillations by similar

excitation mechanisms (Heasley *et al.* 1996, Chapter 2 of this work). Solar-type stars include a broad range of stars with similar spectral type (i.e. Sun-like but in any evolutionary state).

Unfortunately asteroseismology will probably never be as detailed as helioseismology (in terms of the number of observable frequencies). Asteroseismology suffers from imprecise knowledge of stellar parameters (mass, radius, composition, etc.), complicated stellar physics (e.g. crude convection models), and high-quality oscillation data are difficult to obtain (Kjeldsen and Bedding 2000).

That has not, however, discouraged many researchers from attempting observations with ground-based instruments. Although in most cases the evidence for stellar non-radial oscillations is circumstantial, recent observations with refined instruments have proven more successful. The sections below discuss attempts made over the past decade to observe stellar non-radial pulsations, and the development of the data gathering and analysis techniques.

### 1.6.1 Arcturus

Arcturus ( $\alpha$  Boo), a K2 III red giant, is the brightest star in the northern hemisphere. That makes it a prime candidate for observation. However, its evolved state means any observable oscillations will most likely be at the radial  $l = 0$  mode, have large amplitudes and long periods, which require very long integration times. The strongest case for observed oscillations is from Belmonte *et al.* (1990).

Over a period of 11 days, Belmonte *et al.* accumulated about 82 hours of data at the 4.2 m William Herschel Telescope of the Observatorio del Roque de los Muchachos

in April-May 1988. They claim the identification of acoustic oscillations of several modes ranging from  $\nu \sim 1$  to  $80 \mu\text{Hz}$  with a peak at  $4.3 \mu\text{Hz}$ . Their analysis revealed frequency spacings of  $\Delta\nu_0 \sim 5 \mu\text{Hz}$  or  $2.3 \mu\text{Hz}$ .

The work came under scrutiny by KB95, who admit a possible agreement with predictions ( $\Delta\nu_0 = 0.9 \pm 0.2 \mu\text{Hz}$ ) and a periodicity that could be of stellar origin, but argue that solar-like oscillations have not been observed to any degree of certainty.

One of the main reasons for their conclusions is that the length of the time series is too short for  $p$ -mode detection. Hence, the proposed Belmonte *et al.* detections result from the data cleaning process. Simulations and analysis by KB95 show that the process moved all the power into discrete frequencies. The result of Belmonte *et al.*, though, can be used to set an upper limit in the peak amplitude. KB95 determine a peak amplitude of  $\sim 30 \text{ m s}^{-1}$  from the same data, and conclude the Arcturus observations provide a challenge to predictions. A more detailed discussion of giant star pulsations is given in Chapter 5 for  $\beta$  Gem.

### 1.6.2 Procyon ( $\alpha$ CMi)

One of the key elements required to transform the observed oscillation spectrum into refined stellar parameters is an accurate stellar model. Recall that inversion techniques require the identification of many frequencies, while asteroseismology can only obtain a few low degree modes, so stellar models are needed as a reference. The early analysis of oscillations for Procyon suffered from a discrepancy in the star's assumed mass, but that is a problem where asteroseismology would help.

Brown *et al.* (1991) obtained velocity data suggestive of  $p$ -mode oscillations, and found the power in the signal was situated between 300 and 1400  $\mu\text{Hz}$  with a rms velocity of  $2.5 \text{ m s}^{-1}$ . Brown *et al.* did not claim concrete evidence that a  $p$ -mode oscillation had been observed (as it could have been explained by noise), but suggested that it was the best explanation of the data.

The fundamental parameters for Procyon,  $\pi = 287 \pm 4 \text{ mas}$  (Strand 1951, Hipparcos gives  $285.93 \pm 0.88 \text{ mas}$ ),  $L/L_{\odot} = 7.1 \pm 1.0$ ,  $T_{\text{eff}} = 6500 \pm 100 \text{ K}$  (Guenther and Demarque 1993), and  $R/R_{\odot} = 2.10 \pm 0.16$  (KB95), are all reasonably well determined. It is Procyon's mass determination that was not accurately calculated.

One would think that the binary nature of the Procyon system (with a white dwarf) would allow a well-established mass for the star. Observations by Irwin *et al.* (1992) resulted in an astrometric mass of  $M = 1.751 \pm 0.051 M_{\odot}$ , consistent with  $1.74 \pm 0.04 M_{\odot}$  determined by Strand (1951). However, the detailed computational stellar evolutionary models of Guenther and Demarque (1993) indicate that a mass of  $M = 1.751 \pm 0.051 M_{\odot}$ , along with Procyon's observed composition, are just barely consistent with its position on the HR-diagram. A match is only accomplished when the models are pushed to the edge of the error box defined by the mass and metallicity determinations. They suggest that a mass of about  $M \sim 1.50 M_{\odot}$  more accurately represents Procyon's observed pulsation parameters. A more detailed  $p$ -mode detection could be used to refine the star's mass and composition further.

The problem of Procyon's mass was resolved with the information from Girard *et al.* (2000)<sup>1</sup> using Wide Field Planetary Camera (WFPC2) images. They obtained a new

---

<sup>1</sup> The results were first released by Girard *et al.* (1996) for the AAS conference proceedings.

astrometric mass of  $M = 1.497 \pm 0.037 M_{\odot}$  for the primary star, in very good agreement with the theoretical stellar and pulsation models of Guenther and Demarque (1993).

The latest observational search for non-radial oscillations on Procyon was made in November 1998 by Martić *et al.* (1999, hereafter M99). A concurrent analysis by Barban *et al.* (1999, hereafter B99) compares theoretical stellar models and time series simulations to the data given in M99. The observations by M99 spanned ten days. The Doppler measurements were obtained with the ELODIE echelle spectrograph on the 1.93 m telescope at L' Observatoire de Haute Provence.

M99 confirm the stellar origin of the oscillations proposed by Brown *et al.* (1991), since they observed an excess of power between 500 – 1500  $\mu\text{Hz}$ . They were able to place an upper limit of 0.50 – 0.60  $\text{m s}^{-1}$  for the amplitude oscillations, with a frequency cutoff of  $\nu_{\text{ac}} \sim 1500 \mu\text{Hz}$  and a (most probable) large frequency spacing of  $\Delta\nu_0 \sim 55 \mu\text{Hz}$ .

With the new determination of Procyon's mass, the predicted oscillation parameters are:  $\nu_{\text{osc}} = 111 \pm 17 \text{ cm/s}$  (Eq 1.13),  $\nu_{\text{max}} = 1000 \mu\text{Hz}$  (Eq 1.11), and  $\Delta\nu_0 = 54 \pm 6 \mu\text{Hz}$  (Eq 1.10), in general agreement with the results of M99. In further support are the conclusions of B99 that the measurements of M99 agree well with the time series simulations under the same observational conditions. B99 confirm a periodic pattern in the Fourier spectrum and interpret, not confirm, it as the large frequency spacing. The analysis of the data is complicated by the single-site window function; which basically means there were gaps in the signal (Kjeldsen and Bedding 2000). B99 propose concrete that evidence can be obtained with current Doppler instruments using multi-site observations, i.e. long term, uninterrupted viewing.

Stimulated by the recent oscillation results and the notion that Procyon will be observed by the future MOST and MONS missions, Chaboyer *et al.* (1999) produced a grid of stellar models and a subsequent analysis of the pulsation spectra. Such an analysis can be used to interpolate the interior structure of the star and to test the stellar evolution model when a defined pulsation spectrum is observed. The same motivation led to the work done in this thesis. Much of the research here follows the same reasoning and method incorporated by Chaboyer *et al.* (1999).

### 1.6.3 $\alpha$ Cen A

The  $\alpha$  Cen system is an obvious candidate for observing solar-like oscillations. The primary,  $\alpha$  Cen A, is of spectral type G2 V (solar type),  $\alpha$  Cen is also the nearest system to the Sun. Its binary nature and proximity greatly assist the determination of accurate stellar parameters:  $M = 1.09 \pm 0.01 M_{\odot}$ ,  $L/L_{\odot} = 1.45 \pm 0.03$  (Demarque *et al.* 1986);  $T_{\text{eff}} = 5770 \pm 20$  K (Soderblom 1986); which give  $R/R_{\odot} = 1.21 \pm 0.02$ . When these values are scaled by the solar case, one predicts:  $v_{\text{osc}} = 31.20$  cm/s;  $v_{\text{max}} = 2300$   $\mu\text{Hz}$ ;  $n_{\text{max}} = 20$ ; and  $\Delta\nu_0 = 105.8 \pm 2.7$  (KB95; Edmonds *et al.* 1992 gives  $\Delta\nu_0 = 107.9$   $\mu\text{Hz}$ ).

Early observations by Brown and Gilliland (1990) and Edmonds (1993) were not able to achieve a noise level needed to observe the predicted velocity, but did set a strong upper limit. The earliest case for a positive detection was made by Pottasch *et al.* (1992) using the 3.6 m telescope of the European Southern Observatory over 6 consecutive nights in April 1990.

Pottasch *et al.* claimed to find amplitudes on the order of 3 – 5 times solar ( $v_{\odot} = 23.4 \pm 1.4 \text{ cm/s}$ )<sup>2</sup>, high for a star so similar to the Sun. Their calculations of the mean separation between modes,  $\sim 55.3 \pm 3.6 \text{ } \mu\text{Hz}$  ( $= \Delta\nu_0/2$ ), is on the order of predictions, but as pointed out by KB95, the observations did not give good evidence of solar-like oscillations. Rather, the work by Pottasch *et al.* resulted in an upper limit to  $\alpha \text{ Cen A}$ 's  $p$ -mode oscillation velocity.

The argument given by KB95 to explain the strong, evenly-spaced peaks is again based on the incorrect interpretation of the data, i.e. the data can be explained by periodic noise fluctuations. Another argument is that there is not enough power to account for the noise and the signal. The frequency range claimed by Pottasch *et al.* (1992), 2250 – 3450  $\mu\text{Hz}$ , does not exhibit excess power relative to the rest of the spectrum.

Later observations by Kjeldsen *et al.* (1999) set an upper limit for the oscillation amplitudes of about 1.4 times solar, leading them to claimed only tentative evidence for  $p$ -mode detection. Their method involved measuring Balmer-line equivalent widths using two telescopes over six nights of observation.

Perhaps the most promising results to date originated independently from Schou and Buzasi (2000) and Bouchy and Carrier (2001; hereafter BC2001). Schou and Buzasi performed a time-series analysis of photometric data taken with the Wide-Field Infrared Explorer (WIRE) satellite. They see evidence for solar-like  $p$ -mode structure in their spectrum.<sup>3</sup>

---

<sup>2</sup> KB95 take the average of 23.0, 21.0, 24.0, and 25.5 cm/s of Grec *et al.* 1983, Isaak *et al.* 1989, Jiménez *et al.* 1990, and Libbrecht and Woodward 1991, respectively.

<sup>3</sup> This information comes from the abstract of Schou and Buzasi (2000) for the AAS meeting. To date no journal publication has resulted.

BC2001 report on successful observations of velocity amplitudes using the CORALIE echelle spectrograph (Queloz *et al.* 2000) on the 1.2 m Swiss telescope at the ESO La Silla Observatory. The observations were made recently during 5 nights in May 2001 and the data consist of 1260 high precision radial velocity measurements with a typical signal-to-noise ratio in the range of 300 - 420 (at 550 nm).

Their resulting power spectrum exhibits many peaks in the range of 1700 – 3000  $\mu\text{Hz}$  over a broad envelope (analogous to Figure 1.1). A *comb response* of the power spectrum (a method to search for periodicity in the data hampered with daily gaps; see also the discussion on page 29) gives an average of the large spacing of  $\langle \Delta v_o \rangle = 105.7 \mu\text{Hz}$ . They estimate an average mode amplitude by using a simulated time series generated with an artificial signal plus noise using their window function (the same method adapted from KB95). Several of the simulations give  $\langle v_{\text{osc}} \rangle \approx 35 \text{ cm s}^{-1}$  and  $v_{\text{max}} \approx 2360 \mu\text{Hz}$ .

The results presented by BC2001 are in very good agreement with predictions for  $\alpha$  Cen A:  $v_{\text{osc}} = 31.1.0 \text{ cm s}^{-1}$ ,  $v_{\text{max}} = 2300 \mu\text{Hz}$ , and  $\Delta v_o = 105.8 \pm 2.7 \mu\text{Hz}$ . Such high resolution measurements can also be used in conjunction with stellar models (Guenther and Demarque 2000; hereafter GD2000) to constrain the fundamental parameters of  $\alpha$  Cen A; see discussion below.

In anticipation of the successful detection of global *p*-modes oscillations on  $\alpha$  Cen A (and B), GD2000 generated a grid of detailed stellar models incorporating all of  $\alpha$  Cen A's observational uncertainties. The models were constructed using the Yale Stellar Evolution Code with Rotation (YREC; Guenther *et al.* 1992a; see § 2.5 of this work) and subsequently pulsed using Guenther's (1994) pulsation code (§ 2.6). The best models for



$\alpha$  Cen A produce an average of the large and small frequency spacing of  $101 \pm 3 \mu\text{Hz}$  and  $4.6 \pm 0.4 \mu\text{Hz}$ , respectively (refer to § 2.3.1. for discussion on the small frequency spacing). The theoretical pulsation spectrum for modes of  $l = 0, 1, 2, 3$  are calculated and presented in Table 5 of GD2000.

The fundamental parameters of  $\alpha$  Cen A are fairly well determined, so the present and future observations can be applied to test stellar structure theory. The inferred radius of  $\alpha$  Cen A is related to the  $p$ -mode oscillation data, which in turn can be used to test convective transport theory. Equally important, the  $p$ -mode frequencies can be used to infer an age for the star. Pulsation models, such as those produced in GD2000 and in this work, can be used to generate relations like those in Figure 1.4, a plot of  $p$ -mode frequencies as a function of age (GD2000). Interpolation on to the observed values for  $\nu$  and  $n$  can result in a reliable age determination.

Supplementing the observations of  $\alpha$  Cen by BC2001, were measurements obtained during the same period by T. Bedding and collaborators using the UCLES spectrograph on the 3.9 m Anglo Australian Telescope, and with the UVES spectrograph on the 8.2 m Very Large Telescope (this information is given in BC2001). Their findings are yet to be released, but it should be possible to use them to construct a  $p$ -mode spectrum based on the multi-site data (not to mention with the results of the future MONS observations), further refine the spectral window and explore  $\alpha$  Cen A's oscillation spectrum in even greater detail.

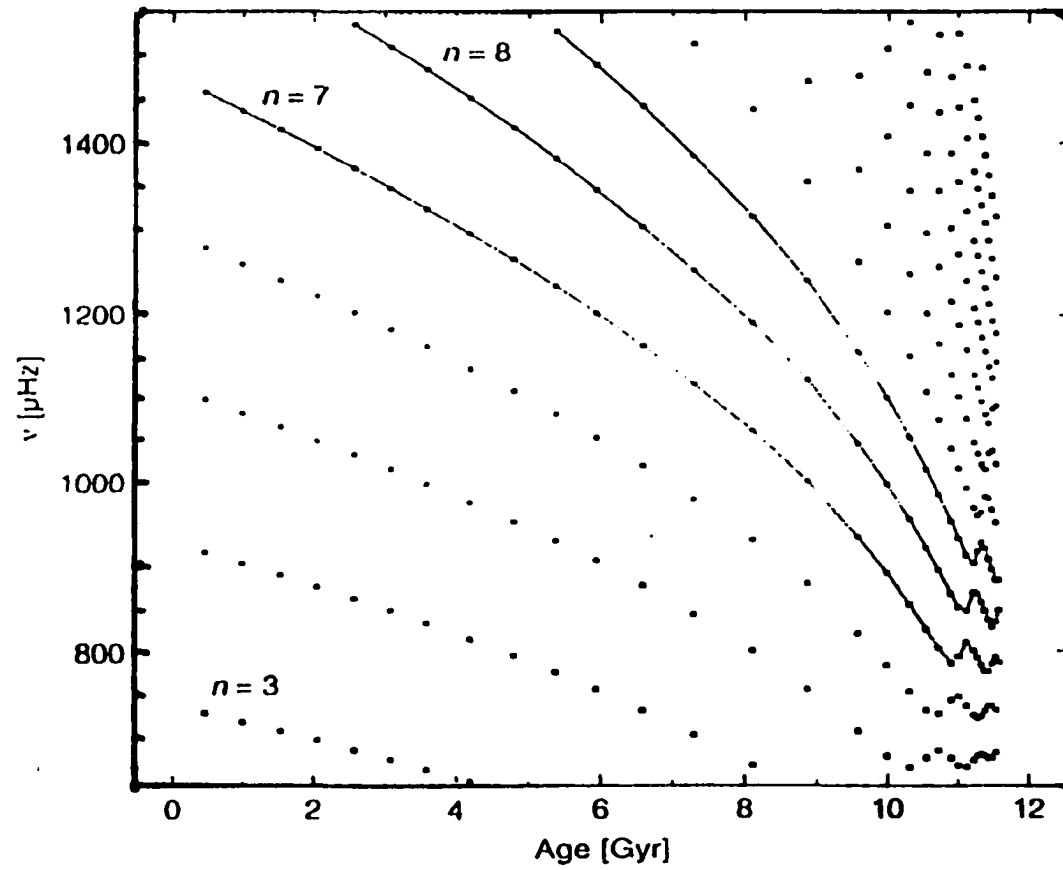


**Figure 1.4** Several  $l = 1$  p-mode frequencies of an evolving  $1 M_{\odot}$  star of solar composition, plotted against age. Lines have been drawn through the  $n = 7, 8$ , and  $9$  data points. Information of this type allows for the potential age determination with the addition of  $p$ -mode observations (from Guenther and Demarque 2000).

#### 1.6.4 $\eta$ Boo

$\eta$  Boo (G0 IV;  $L = 9.5 \pm 0.7 L_{\odot}$  Harrington *et al.* 1993;  $T_{\text{eff}} = 6050 \pm 60$  K Bell and Gustafsson 1989;  $M = 1.6 \pm 0.2 M_{\odot}$  Kjeldsen *et al.* 1995) has not been a target for an asteroseismological telescope for very long, or very often. Two independent observations resulted in totally different findings, one successful and one failed. However, all model calculations are in agreement with the claimed successful observations.

Kjeldsen *et al.* (1995; hereafter KBVF) turned the 2.5 m Nordic Optical Telescope (La Palma) on  $\eta$  Boo for six nights in April (22-28) 1998. Using the Balmer-line-equivalent-width technique (§ 1.4.3), KBVF were able to determine an excess of power centred at about 850  $\mu\text{Hz}$ . That is shown in Figure 1.5, the power spectrum (PS) which was determined using a discrete Fourier transform. The upper panel shows their window function (PS of sampling function). Figure 1.6 shows the strong side lobes produced by the daily gaps at splittings of  $\pm 1/\text{day} = 11.57 \mu\text{Hz}$  (KBVF).

After the application of a *comb response* function (Figure 1.6 KBVF) to the smoothed PS to identify regularity, a modified version of the CLEAN algorithm (Roberts *et al.* 1987) was applied for the identification of the oscillation frequencies contained in the power spectrum. They claimed to identify 13 possible oscillation modes, and using asymptotic theory (§ 2.3) they derived average large spacing values for three modes of degree  $l = 0, 1, 2$ :  $\Delta\nu_{l=0} = 40.6 \pm 0.3 \mu\text{Hz}$ ;  $\Delta\nu_{l=1} = 40.1 \pm 0.7 \mu\text{Hz}$ ; and  $\Delta\nu_{l=2} = 39.9 \pm 0.4 \mu\text{Hz}$ . Their average oscillation signal, 45 ppm, corresponds to an amplitude of about 1.6  $\text{m s}^{-1}$  if  $\eta$  Boo were observed in radial velocity (a large telescope would be needed to detect that given  $\eta$  Boo's apparent magnitude of,  $V = 2.68$ ).

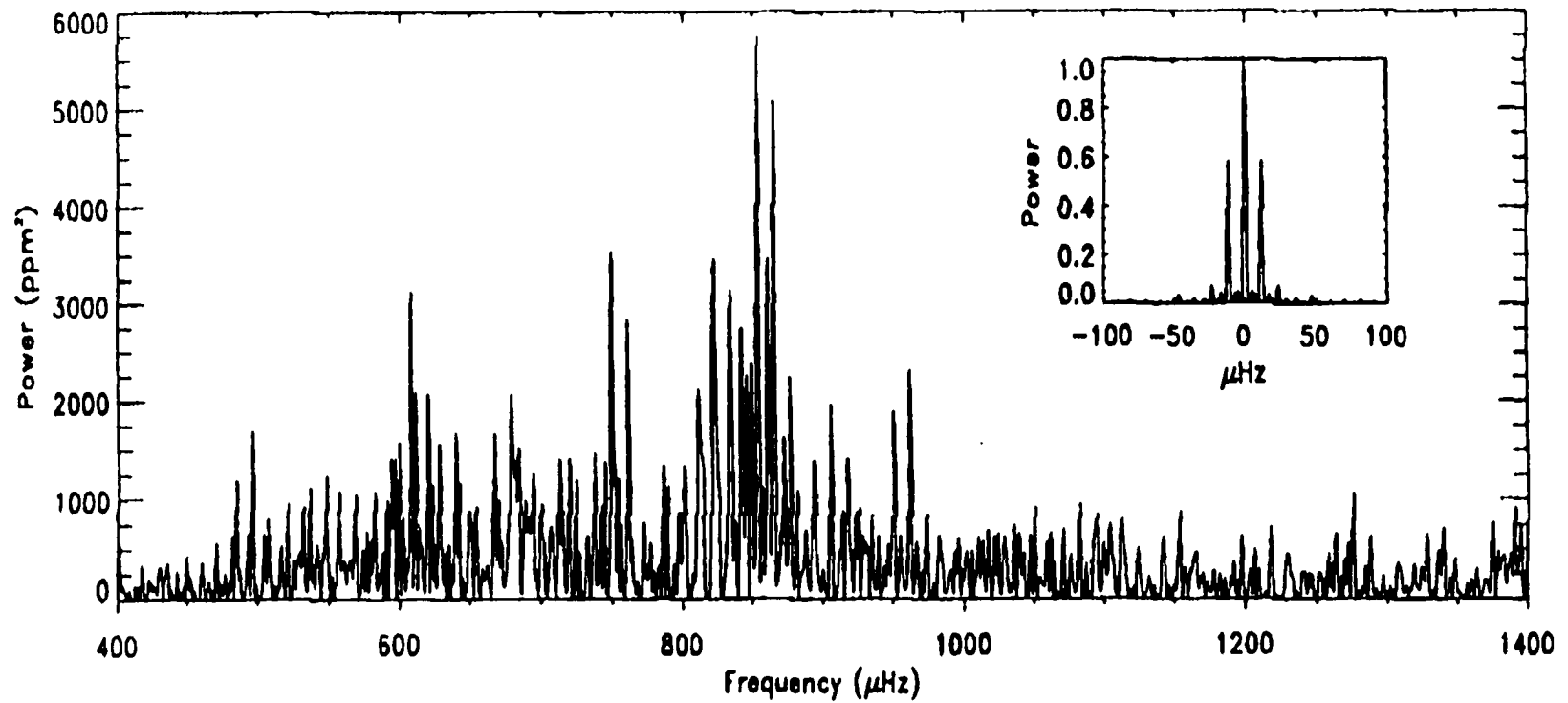


**Figure 1.5** Power spectrum of equivalent width measurements for  $\eta$  Boo. The inset shows the window function. Note the clear power excess around 850  $\mu\text{Hz}$  (KBVF).

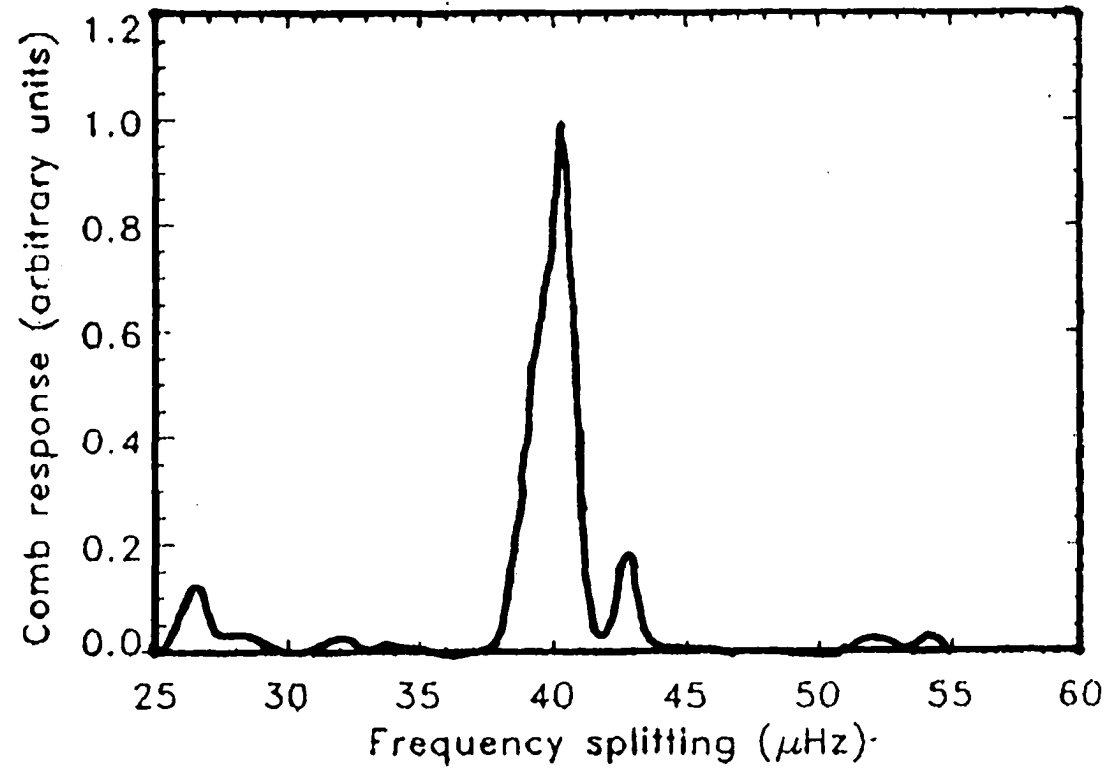


**Figure 1.6** A *comb response* of the power spectrum for the  $\eta$  Boo data. Note the side-lobes resulting from the daily gaps. The comb response searches for regularity in the PS, and indeed there is a single peak at  $\Delta\nu = 40.3 \mu\text{Hz}$  (KBVF).

The CLEANed spectrum also reveals the possible identification of modes which are propagating in avoided crossings; i.e. frequencies resulting from the interference between  $p$  and  $g$ -modes, and thus do not obey the asymptotic relation (discussed in more detail in Chapter 4,  $\beta$  Hydri). If future, higher resolution observations (e.g. MONS) can confirm the existence of these bumped (excited) modes, it would be the first detection of its kind which would yield information on the deep stellar interior.

Support for the KBVF findings comes in the form of theoretical models and simulations by Christensen-Dalsgaard *et al.* (1995; hereafter CDBK), Guenther and Demarque (1996; hereafter GD96), and predictions using the derivations of KB95 ( $\Delta\nu_0 = 36 \pm 3 \mu\text{Hz}$ ).

CDBK produced stellar evolution and pulsation calculations for  $\eta$  Boo, and compared their results with the KBVF observations. The models coincide very well with the observations. The  $l = 0$  and 2 modes and the small frequency spacing are readily identifiable. The six observed frequencies for the  $l = 1$  mode also agree well with models. Probably one of the most interesting findings was the correlation between the theoretical avoided crossings and those speculated by the data of KBVF. The large irregular peaks may be the result of a resonance with a region just outside the stellar core, where the modes behave like trapped gravity waves (CDBK). This is an indication of the observable effects which are directly related (induced by) to the core environment, which would be of great interest to the astrophysical community.

The approach taken by GD96 was a direct application of how the  $p$ -mode observations can be used to aid in constraining the physical parameters of  $\eta$  Boo. They assume that the observations are real, even though they have not yet been confirmed (see

below). Even if the observations are shown to be false, the work done by GD96 are still useful as a template for future successful observations.

GD96 generated a grid of stellar evolution models for the trigonometric parallax range of 85.80 – 91.80 mas and metallicity  $Z = 0.025 - 0.035$ . The models were tuned to  $\eta$  Boo's position on the theoretical HR-diagram. They were able to draw conclusions that  $\eta$  Boo has exhausted its core hydrogen and is in the shell contraction phase evolving towards the giant branch. Their pulsation analysis reproduced the observations, and of even greater significance was the reproduction of the observed mode bumpings (avoided crossings). That is only possible if the stellar models and  $\eta$  Boo are evolutionary equivalent because the mode bumping spectrum is sensitive to small perturbations in the model parameters (GD96).

Their best fit to the data was for  $M = 1.55 M_{\odot}$ ,  $\pi = 89.50$  mas, age  $\sim 2.3$  Gyr, and a surface helium abundance of  $Y \approx 0.280$ . The largest source of uncertainty is  $\eta$  Boo's metallicity. Based on the observed parallax [ $87.0 \pm 3.4$  mas; Yale Parallax Catalogue (van Altena, Lee, and Hoffleit 1995)] and  $p$ -mode spectrum, the models with  $[Fe/H] = 0.33$  are more accurate than the adopted metallicity of  $[Fe/H] = 0.19$  (Tomkin, Lambert, and Balachandran (1985), Edvardsson *et al.* 1993).

Interestingly, the parallax is restricted to  $89.5 \pm 0.5$  mas (model with  $Z = 0.03$ ,  $\alpha = 1.7$ , and the weak condition  $1.5 < \Delta Y / \Delta Z < 3.5$ ) when the  $p$ -mode data are taken into account. The large dependence of the model parameters on parallax results in a strong test with theory when the accurate parallax is obtained by the Hipparcos mission is taken into account.

The Hipparcos mission determined a parallax of  $\pi = 88.17 \pm 0.75$  mas for  $\eta$  Boo. It is close to the restrictions that  $\pi = 89.5 \pm 0.5$  mas determined by GD96 and supports the conclusion that  $\eta$  Boo exhibits solar-like oscillations. However, the above parallaxes are not equal within uncertainty. Although to date no follow up theoretical analysis has been made, the Hipparcos results imply some slight theoretical changes to stellar models. Most likely the results of GD96 can be made to match the Hipparcos data with some fine tuning of the metallicity parameter  $Z$ . There is also the slight possibility that the discrepancy is a result of our understanding of convection, implying perhaps a change of mixing length parameter,  $\alpha$ , or a refined convection theory. In general the results of the models have been deemed excellent in conjunction with the Hipparcos determination (Bedding *et al.* 1998).

In an effort to confirm the  $p$ -mode observation by KBVF, Brown *et al.* (1997; hereafter B97) found no evidence for excess power at the frequencies reported by KBVF. The B97 Doppler-shift measurements were made using the Advanced Fiber Optic Echelle (AFOE) on the 1.5 m Tillinghast telescope at the Whipple Observatory during the nights of March 14 – 20, 1995.

Their velocity time series had an upper limit in amplitude of  $\sim 0.5 \text{ m s}^{-1}$ , 1/3 the velocity amplitude found by KBVF. B97 also found no single mode greater than  $2.5 \text{ m s}^{-1}$ , and determined the maximum allowable amplitude to be  $\sim 1.5 \text{ m s}^{-1}$ , slightly less than the  $1.6 \text{ m s}^{-1}$  amplitude average of KBVF. B97 offered three possible explanations for the differences. First, the interpretation of the data by one or both groups is in error (as a result of noise). As previously discussed, the correct treatment of noise is difficult to obtain since the noise in precision measurements is subtle and difficult to identify.



Secondly, there may be an incorrect calibration between the two methods: Doppler-shifts and Balmer line equivalent widths. Lastly the  $p$ -mode frequencies or amplitudes for  $\eta$  Boo could have changed in the year between observations. A shift of only a few  $\mu\text{Hz}$  would be enough to ruin the expected detection of power at the KBVF frequencies. The converse would, however, greatly improve the agreement. Such a possibility (oscillation spectrum changes over only a year) seems less likely, but it has been shown, at least for the Sun (Régulo *et al.* 1994), that low degree  $p$ -modes change frequency with the changing magnetic cycle (recall discussion in § 1.2.3 about the solar Tachocline). We should not rule out the possibility that the frequencies actually changed given that our knowledge of oscillation driving and damping mechanisms is limited (B97).

The findings of B97 are a setback to the search for solar-like oscillations on  $\eta$  Boo. On a positive note,  $\eta$  Boo is scheduled to be observed by the MONS mission; which could determine the star's non-radial oscillation spectrum to a very high precision.

#### 1.6.5 $\alpha$ Ursae Majoris ( $\alpha$ UMa)

Observation of  $\alpha$  UMa system were made by Buzasi *et al.* (2000) using the Wide-Field-Infrared-Explorer's (WIRE) on-board 52 mm-aperture star camera, the first space-based observations. The satellite is on a Sun-synchronous orbit, and  $\alpha$  UMa is only observable for less than half the orbit (40 of about 96 minutes), so the data consist of, literally, millions of observations of the K0 III giant star.

Similarly to KBVF, a discrete Fourier transform (DFT; Foster 1996) was used to search for periodicity. The CLEAN (Roberts *et al.* 1987) algorithm was performed to remove alias peaks from the over-sampled DFT. Their time series analysis revealed two

possible sets of peaks: one in the 2 – 50  $\mu\text{Hz}$  range and one centred around 200  $\mu\text{Hz}$ . They claim that the lower set of peaks represents a possible physical solution, and the other peaks are an alias. Scaling from the solar case, in conjunction with theoretical models of giant stars, predict a low frequency maximum,  $\nu_{\text{max}} \sim 18.0 \mu\text{Hz}$  (Equation 1.11), which is in agreement with the theoretical work of Guenther *et al.* (2000). Predictions also suggest  $\Delta\nu_0 \approx 1.82 \mu\text{Hz}$  (Equation 1.10), which is half the average value found by Buzasi *et al.* (2000):  $\langle\Delta\nu_0\rangle = 2.94 \mu\text{Hz}$ . That result can be explained if only even or odd valued radial order  $n$  modes are excited, but the simplest, and most likely, reason is that only the  $l = 0$  modes are excited. Hence, what is observed may be purely radial pulsation.

With the results of Buzasi *et al.* (2000), Guenther *et al.* (2000) were able, for the first time, to use the techniques of asteroseismology to probe the interior of a red giant. The interpretation that the observed frequencies are radial pulsations is supported by their models that have a radial order  $n = 0, 1$ , and 2. Guenther *et al.* (2000) are also able to derive a pulsation mass of,  $M = 4.25 \pm 0.25 M_{\odot}$  for  $\alpha$  UMa, which is in good agreement with the binary system's astrometric mass function (Söderhjelm 1999).

Guenther *et al.* claim only a tentative match of the observed frequencies to those determined in the model, and suggest that the low  $l$  non-radial modes claimed to be observed are all mixed modes ( $g$ -mode bumping/mixing) very closely spaced. The close spacing frequencies are going to have very small amplitudes as a result of the damping in the convective envelope, so detection is made very difficult by ground instruments. A detailed discussion of giant star pulsation is given in this work for  $\beta$  Gem (K0 III) in Chapter 5.

### 1.6.6 M67

Unfortunately, a search for solar-like oscillations on stars in the open cluster M67 by Gilliland *et al.* (1993; hereafter Gilliland93) gave only inconclusive results. However, the technique employed and the sheer size of the operation deserves to be mentioned.

The work by Gilliland93 was the first attempt to use multi-site observations with differential CCD photometry. It was an “all out” campaign with many collaborators using seven telescopes scattered around the globe. Among them were the Kitt Peak National Observatory 4 m, CFHT 3.6 m, and the Palomar 5 m telescopes, all used for intense observation. The observations took place over a one-week period in January 1992 for a total of 22 telescope nights and 156 hours.

The observations permitted a precision of 250  $\mu\text{mag}$  per minute, low noise levels, and a good window function that yielded about a 20  $\mu\text{mag}$  threshold (five times solar) for the brightest stars.

As previously stated, only suggestive evidence for global stellar oscillations in a handful of stars (Nos. 16, 27, 28, and 37 in particular) have been obtained to date. The best that can be done is a derivation of upper limits for the parameters of the stars listed in Table 6 of KB95.

The work done by Gilliland93 offers more than a few upper limits on a bunch of stars. The rigorous (yet risky) approaches used to date provide some lessons regarding data acquisition, reduction, and analysis for time-series differential CCD photometry. Gilliland93 suggested that future multi-site searches using the 10 m Keck telescope, and any upgrades made on the original network telescopes, could readily lead to a factor of two improvement in the sensitivity gain (the prediction did not include any possible

advancements in CCD technology). They suggested that future (next generation network) observations will be possible by 1997; merely an optimistic conclusion. To date no further multi-site observations have been made. That is not because people believe the technique will not work, but rather that it is more feasible and efficient to make observations from space.

## 1.7 Seismology in Space

Although current ground-based observations have been obtaining more reliable measurements, and techniques and analytical methods have been improving<sup>4</sup>, what is being offered from space-based observations is much more impressive. From space accurate wide-band photometry can be performed in the absence of atmospheric scintillation. The window function, one of the primary reasons ground-based observations are usually labeled as “suggestive” or “circumstantial”, will be excellent (low side-lobes) and the results will be unaffected by weather (Kjeldsen and Bedding 2000). Thus, even a small aperture telescope will produce much more useful results than the largest ground-based instruments.

There are currently a few forthcoming space missions devoted to obtaining data for a wide variety of stars in a variety of evolutionary stages. COROT (**C**onvection, **R**otation, and planetary **T**ransits) is mainly a French/European project (Baglin *et al.* 1998) that will do photometry from a low-Earth orbit. It will be able to observe two small ( $\sim 12^\circ$  wide) star fields for approximately five months each. The telescope consists of a 25 cm aperture. In addition, after launch in 2004, COROT will search for extra-solar

planets via the transit method, making it a highly anticipated mission (<http://www.astrsp-mrs.fr/www/corot.html>). Two other missions, one scheduled for launch soon and one in development, are more intimately related to this thesis and are discussed below.

### **1.7.1 MOST (Microvariability and Oscillations of STars)**

If everything goes as planned, the Canadian-made MOST mission satellite will be in orbit sometime between late 2002 and early 2003. Soon thereafter the satellite, termed Microsat, will commence observations of a wide variety of solar-type, metal-poor subdwarfs (see Shkolnik 2000), rapidly oscillating Ap (roAp) stars, and Wolf-Rayet stars.

Unprecedented photometric precision will be obtained with Microsat which has an aperture of only 15 cm. The orbit will be a Sun-synchronous, circular orbit with an inclination of  $98.6^\circ$ , an altitude of 785 km, and a continuous viewing zone (CVZ) of  $\sim 54^\circ$  for stars with a declination between  $-18^\circ$  and  $+36^\circ$ . That configuration allows stellar candidates to be observed for up to  $\sim 40$  days. The mission scientist is Dr. Jaymie Matthews (Matthews *et al.* 2000) at the University of British Columbia (<http://www.astro.ubc.ca/MOST/>).

### **1.7.2 MONS (Measuring Oscillations in Nearby Stars)**

This is a Danish-led project with contributions from Australia and other countries (Kjeldsen, Bedding, and Christensen-Dalsgaard 2000; <http://astro.ifa.au.dk/MONS>). In its early phases of construction, the Rømer satellite will have an aperture size of about 40 cm and will observe stars from a highly elliptical geostationary transfer orbit. Its orbital

---

<sup>4</sup> Heasley *et al.* (1996) suggested that the prospects are still good and that high resolution measurements can/will be made with single site observations.

period of 12 hours and altitude varying from 600 km to 40 000 km will permit long-term observations of nearly any nearby star. Similar to COROT, the MONS Rømer satellite also has planet detection capability.

# Chapter 2

## Theory and Model Descriptions

### 2. Introduction

The theory of stellar nonradial pulsations is not unlike the classical description of oscillations in an organ pipe or a vibrating string. The complexity arises with the application of spherical harmonics to match the physical structure of a star, and the appropriate application of the stellar and pulsation hydrodynamic equations. The following information is taken primarily from the lecture notes of Christensen-Dalsgaard (1998).

This chapter is designed to be an introduction to basic nonradial oscillation theory. Some of the topics that will be discussed include: spherical harmonics, linear oscillation theory, the different types of modes, and asymptotic  $p$ -mode theory.

### 2.1 Fundamental Principles

A small perturbation on a spherically symmetric static (non-rotating) star can be used to approximate a non-radial oscillation. The time-dependent eigenfunction used to describe the perturbation for a star, in which its equilibrium state is constant, is

$$\Psi(r, \theta, \phi, t) = \psi_{nl}(r) Y_l^m(\theta, \phi) e^{i\omega_{nl}t} \quad (2.01)$$

where  $\Psi$  represents the radial, pressure, gravitational potential, and the first derivative of the gravitational potential variations.  $Y_l^m(\theta, \phi)$  are the spherical harmonics,

$$Y_l^m(\theta, \phi) = (-1)^m C_{nl} P_l^m(\cos \theta) e^{im\phi} \quad (2.02)$$

where  $\omega_{nl}$  is the angular frequency of the propagating wave,  $P_l^m$  is a Legendre function of degree  $l$  and azimuthal order  $m$ , and the normalization constant  $C_{nl}$  is related to the amplitude of pulsation and is given by:

$$C_{nl} = \frac{(2l+1)(l-m)!}{4\pi(l+m)!} \quad (2.03)$$

such that

$$\int_{\text{sphere}} |Y_l^m|^2 = 1 \quad (2.04)$$

In the spherical harmonic representation,  $\theta$  is the co-latitude (i.e. angular distance from the polar axis) and  $\phi$  is the longitude.

The harmonic degree,  $l = 0, 1, 2, 3, \dots$ , is the number of nodal lines on the stellar surface, and  $m = -l, -l+1, \dots, 0, 1, 2, \dots, l$ , is the number of longitudinal nodal lines. The internal nodal lines, called the radial order  $n$ , is the number of nodes along a radial path to the stellar center. The nonradial oscillations are linearly independent in  $n$  and  $l$ , and  $(2l+1)$ -fold degenerate in  $m$ . Classical radial pulsation is the special case for  $l = 0$ . For  $l \neq 0$ , the oscillations cause the star to deviate from spherical symmetry.

Various depictions of nonradial oscillations for different combinations of  $l$  and  $m$ , resulting from the use of spherical harmonics, are shown in Figure 2.1. Note the deviations from symmetry and the increasing complexity with increasing  $l$  and  $m$ .



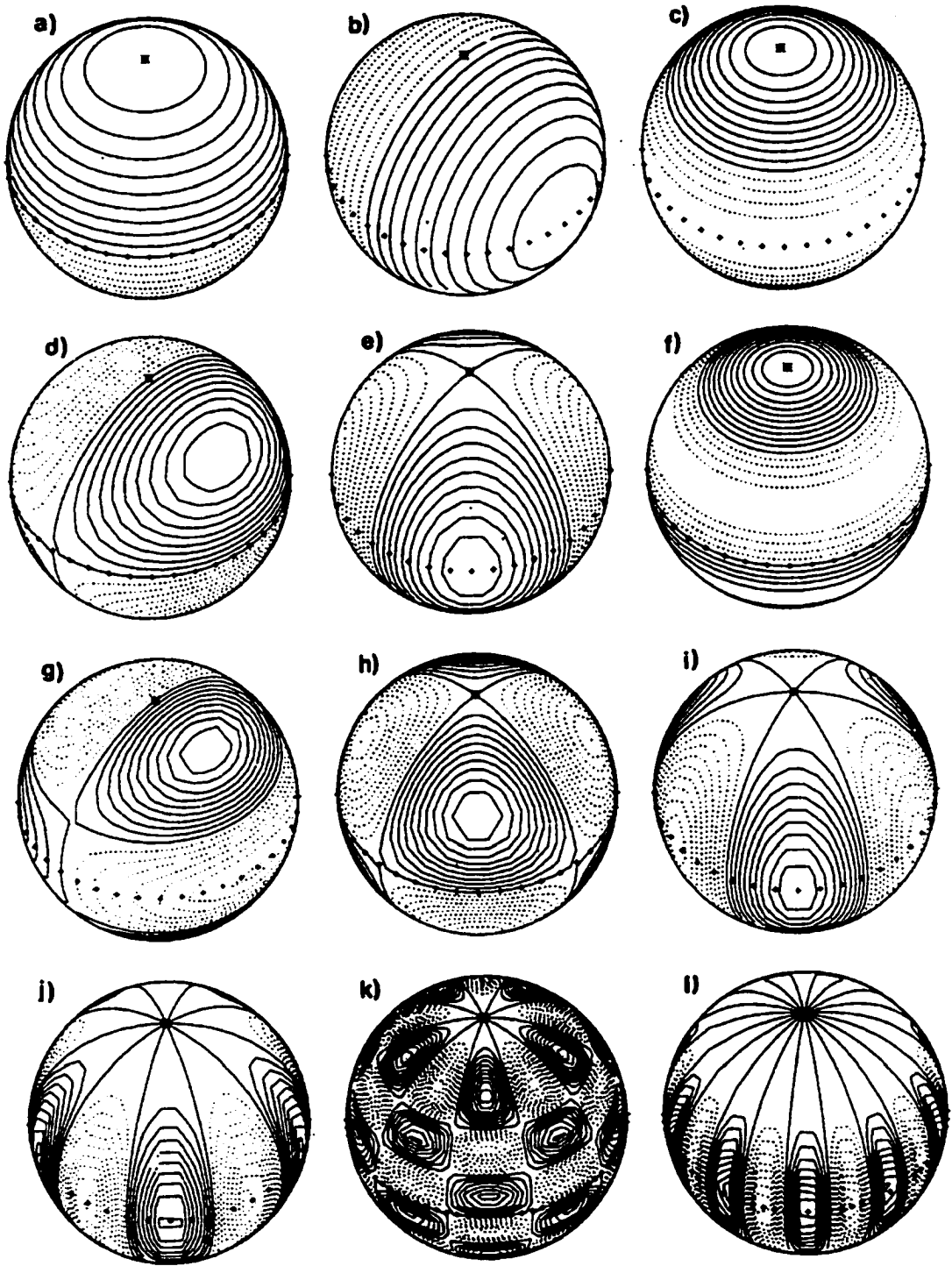


**Figure 2.1.** Contour plots of the spherical harmonics (Equation 2.02). Positive contours are represented by solid lines, and negative contours by dashed lines (phase factor  $(-1)^m$  has been suppressed for simplicity). The equator is shown by “+++++”. The cases illustrated are: a)  $l = 1, m = 0$ ; b)  $l = 1, m = 1$ ; c)  $l = 2, m = 0$ ; d)  $l = 2, m = 1$ ; e)  $l = 2, m = 2$ ; f)  $l = 3, m = 0$ ; g)  $l = 3, m = 1$ ; h)  $l = 3, m = 2$ ; i)  $l = 3, m = 3$ ; j)  $l = 5, m = 5$ ; k)  $l = 10, m = 5$ ; l)  $l = 10, m = 10$ .

## 2.2 Linear Theory

Because oscillation amplitudes are small compared to the stellar radius and the reasonable assumption that stars are spheres makes it convenient to write the pulsation modes in the form,

$$\xi_{nlm}(r, \theta, \phi, t) = \sum_{nlm} \xi_{nl}(r) Y_l^m(\theta, \phi) e^{-i\omega_{nl}t} \quad (2.05)$$

a product of a function of radius  $\xi_{nl}(r)$ , and a spherical harmonic.  $\xi_{nl}(r)$ , for example, is  $\delta r/r$ , where  $\delta r$  is the small radial amplitude variation. Equation 2.05 is complex so only the real part is taken as the oscillation frequency solution. The sign of the imaginary part is important since it reveals information about the type of oscillation: whether it is driven ( $\text{Im}(\omega_{nl}) < 0$ ) or damped ( $\text{Im}(\omega_{nl}) > 0$ ) over time.

The angular frequency  $\omega$  in Equation 2.05 for a specific mode is,

$$\omega_{nl} = 2\pi\nu_{nl} \quad (2.06)$$

where  $\nu_{nl}$  is the frequency, also known as the circular frequency. It is  $\nu_{nl}$  which is commonly used in the literature, describing important frequencies like the solar 5-minute oscillations and the acoustic cutoff frequency (§ 2.2.4) in the solar atmosphere.

### 2.2.1 Lamb and Brunt-Väisälä Frequencies

The Lamb frequency  $L_l$  and the Brunt-Väisälä frequency,  $N$  can characterize the vibrational properties of a star.

The square of the Lamb frequency (also called the critical acoustic frequency) is directly proportional to a quadratic relation involving the harmonic degree  $l$ , the adiabatic

index  $\Gamma_1$ , pressure  $P$ , and is inversely proportional to the square of the distance from the centre  $r^2$ , and the density  $\rho$ . For the local conditions at a distance  $r$  from the centre of the star the Lamb frequency is given by:

$$L_l^2 \equiv \frac{l(l+1)\Gamma_1 P}{r^2 \rho} = \frac{l(l+1)c_s^2}{r^2} = (k_h c_s)^2 \quad (2.07)$$

where  $c_s$  is the local speed of sound and  $k_h$  is the horizontal wave number. Physically  $L_l^{-1}$  is the time required for a sound wave to transverse one horizontal wavelength,

$$\lambda_h = \frac{2\pi r}{\sqrt{l(l+1)}} \quad (2.08)$$

of the disturbance along the circumference of a circle of radius,  $r$ , about the stellar centre. i.e. the sound wave travels a distance  $\lambda_h$  in the interval  $2\pi/L_l$ .

The Brunt-Väisälä frequency,  $N$ , is the angular frequency with which a fluid element of gas may oscillate vertically about an equilibrium position under the restoring force of gravity. The formula is given by,

$$N^2 = g \left[ \frac{1}{\Gamma_1} \frac{d \ln P}{dr} - \frac{d \ln \rho}{dr} \right] \quad (2.09)$$

with  $g$  being the local acceleration of gravity.

The two frequencies play an important role for non-radial oscillations since they define regions where wave propagation can occur. Regions where wave propagation cannot occur are called *evanescent zones*. That is displayed in Figure 2.2, a schematic of a model with a polytropic of index 4 with  $l = 2$  and  $\Gamma_1 = 5/3$  (information from Scuflaire 1974). This *propagation diagram* plots a dimensionless angular frequency squared,  $\omega^2$ , versus the radius fraction,  $r/R$ . The plot defines the region of acoustic ( $p$ -mode, see

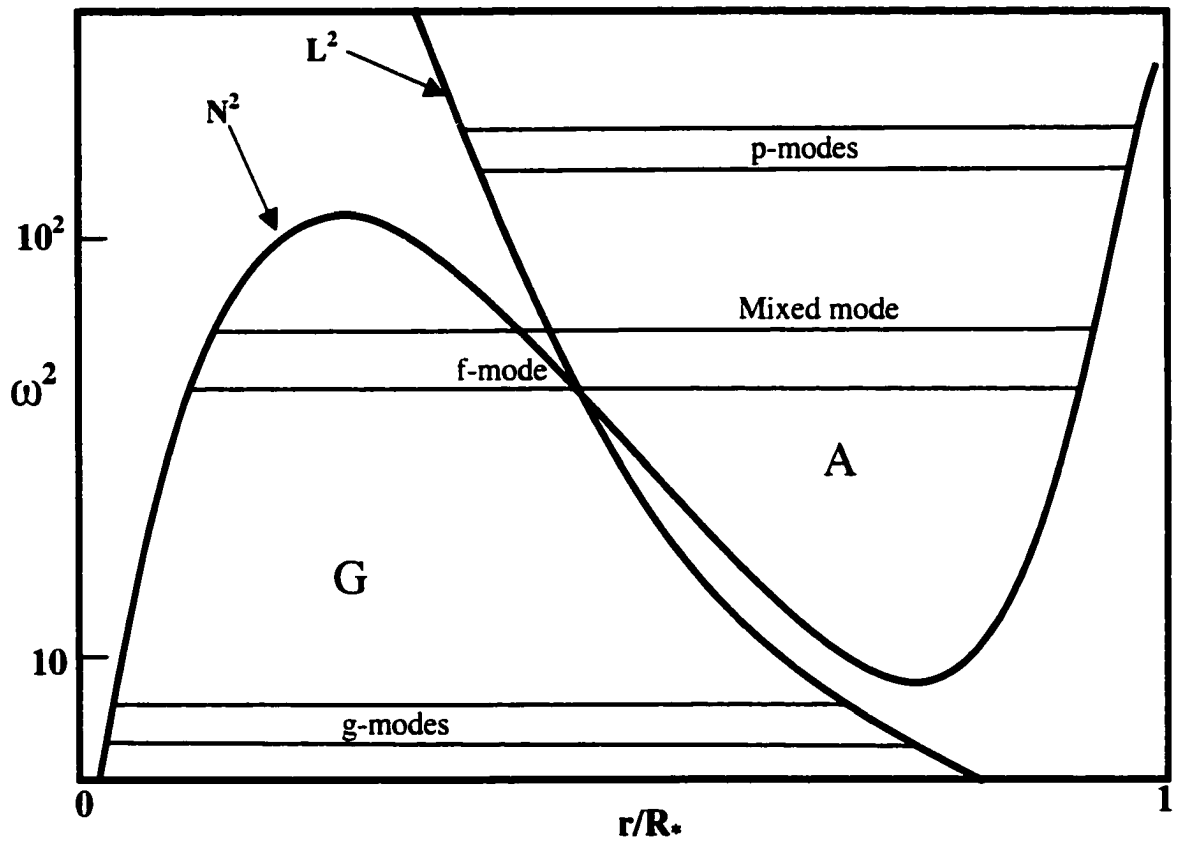


**Figure 2.2** Schematic of a dimensionless propagation diagram. The square of the frequency is plotted vs. radius fraction. The acoustic (A) and gravity (G) regions are not clearly separated, resulting in mixed modes.

below) wave propagation (region A in Figure 2.2), and gravity ( $g$ -mode) wave propagation (region G in Figure 2.2). Acoustic ( $p$ -modes) and gravity ( $g$ -modes) wave propagation dominate the areas defined by  $\omega_n^2 > L_1^2 N^2$  and  $\omega_n^2 < L_1^2 N^2$  respectively, elsewhere the modes are evanescent.

### 2.2.2 General Definitions of $p$ , $g$ , & $f$ -modes

The relation of the Lamb and Brunt-Väisälä frequencies to the physics of the stellar interior leads to an important result:  $g$ -mode propagation is confined predominantly to the inner region, and  $p$ -mode propagation is found, for the majority of the frequencies, in the outer layers of the star. In addition, it is possible for some modes to behave like gravity modes in the stellar interior and like acoustic waves in the outer envelope of the star, such modes are called *mixed* (or *bumped*) *modes*.

Mode mixing can significantly hamper the determination of frequency spacings in stars that have evolved off the main-sequence. That is because the cores of such stars have higher densities than when the star was on the main-sequence. That high density results in  $g$ -modes propagating at higher frequencies, and the frequencies are on the order of acoustic wave frequencies. The kinetic energy of a  $g$ -mode oscillation in its propagation zone (Figure 2.2) can have the same order of magnitude for a  $p$ -mode oscillation. The result is that the oscillation behaves like a trapped acoustic wave in the envelope, and like a trapped gravity wave in the stellar core (p. 143-148 of Unno *et al.* 1989).

### 2.2.3 Turning (Reflection) Points

The depth that acoustic  $p$ -mode waves will penetrate, to first approximation, is solely determined by the variation of sound speed,  $c_s$ , with radius. More specifically, the wave will reflect when its horizontal velocity equals the local speed of sound. The horizontal velocity increases with increasing depth in a star because of the increase in the local pressure. In general, the asymptotic location of the turning point is written in terms of the Lamb frequency,  $L_l(r_t)$ , equated to the angular frequency:

$$L_l = \omega_{nl}$$

or

$$\frac{c_s^2(r_t)}{r_t^2} = \frac{\omega_{nl}^2}{l(l+1)} \quad (2.10)$$

The turning point,  $r_t$ , is a function of  $l$  and  $\omega_{nl}$ .

The reflection can be understood by taking the mode as a superposition of propagating acoustic waves. Figure 2.3 is a representation of this. As the wave propagates deeper into the star, the wavefronts accelerate because of the increase in the local speed of sound because of the increase of pressure with depth. The result is a refraction in the direction of propagation from the radial direction, and when the oscillation is reflected at the surface a spherical acoustic cavity is created. Figure 2.4 plots the eigenfunction (radial component of the velocity), with a density scale factor for resolution in the centre, versus the radius fraction for specific  $p$ -modes. The concentration of the energy density is located mainly in the outer regions of the star for high  $l$ -modes, and the arrow indicates the location of the turning point for the specified

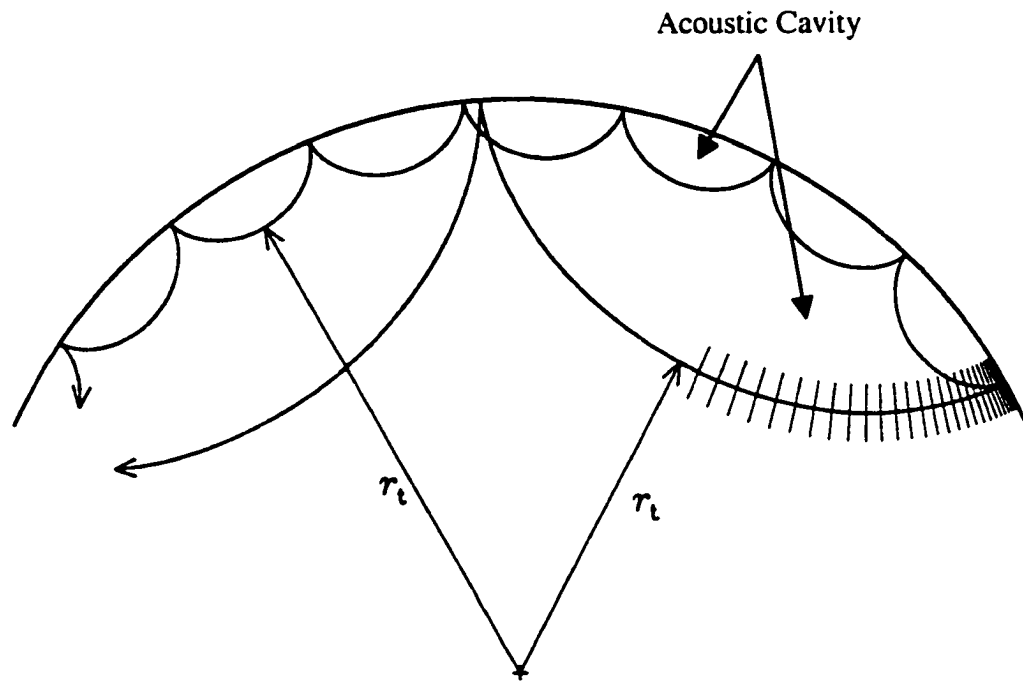


**Figure 2.3.** Propagation of acoustic waves, corresponding to modes with  $l = 30$ ,  $\nu = 3$  mHz (deeply penetrating waves) and  $l = 100$ ,  $\nu = 3$  mHz (waves near the surface). Lines orthogonal to the path of propagation illustrate the wave fronts. Note at least two turning points are required for the existence of an acoustic cavity.

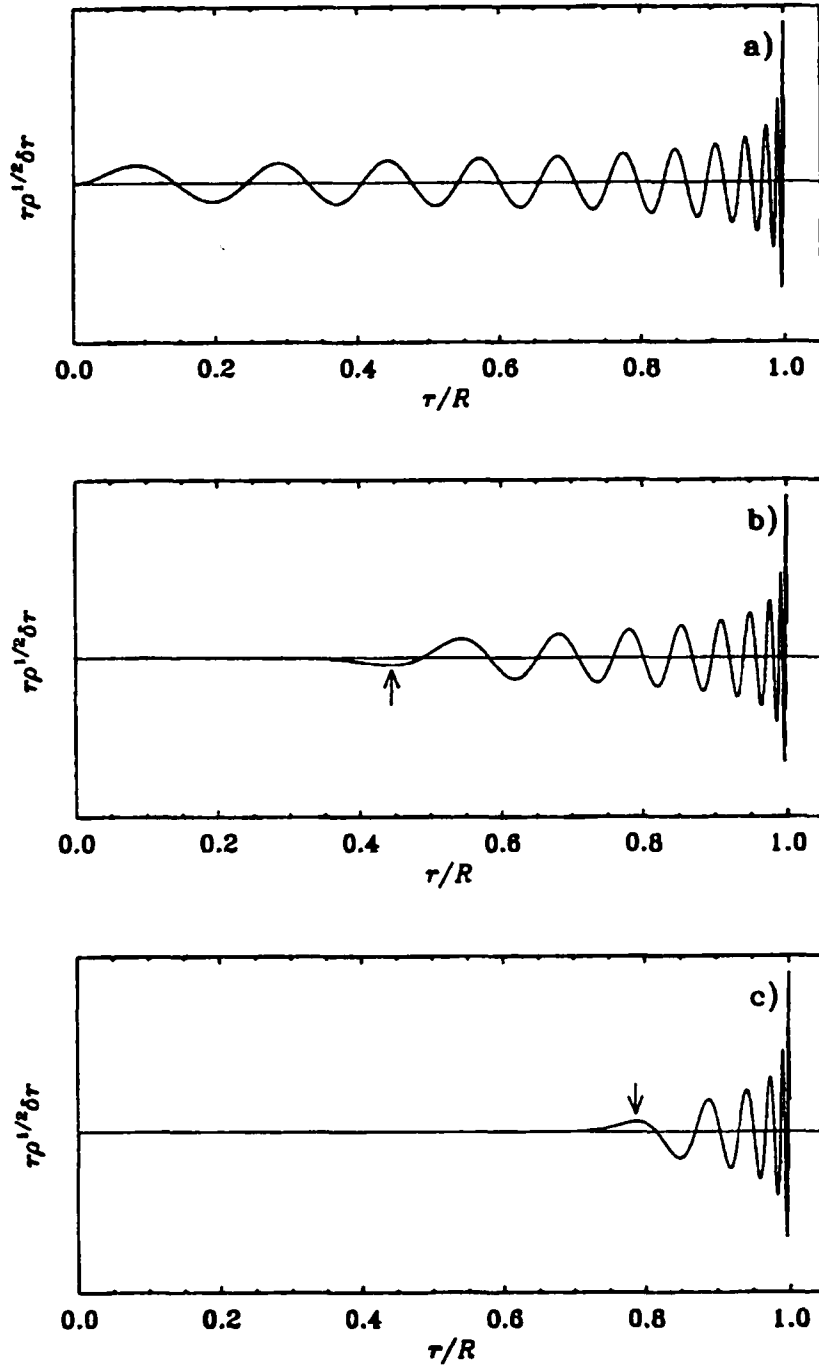


**Figure 2.4.** Eigenfunctions for selected  $p$ -modes in a normal solar model, with a)  $l = 0$ ,  $n = 23$ ,  $\nu = 3310 \mu\text{Hz}$ ; b)  $l = 20$ ,  $n = 17$ ,  $\nu = 3375 \mu\text{Hz}$ ; c)  $l = 60$ ,  $n = 10$ ,  $\nu = 3234 \mu\text{Hz}$ . Arrows mark the asymptotic location (§ 2.3) of the turning points,  $r_t$ . Note the increase in energy density, hence oscillation amplitudes, in the outer regions of the star.



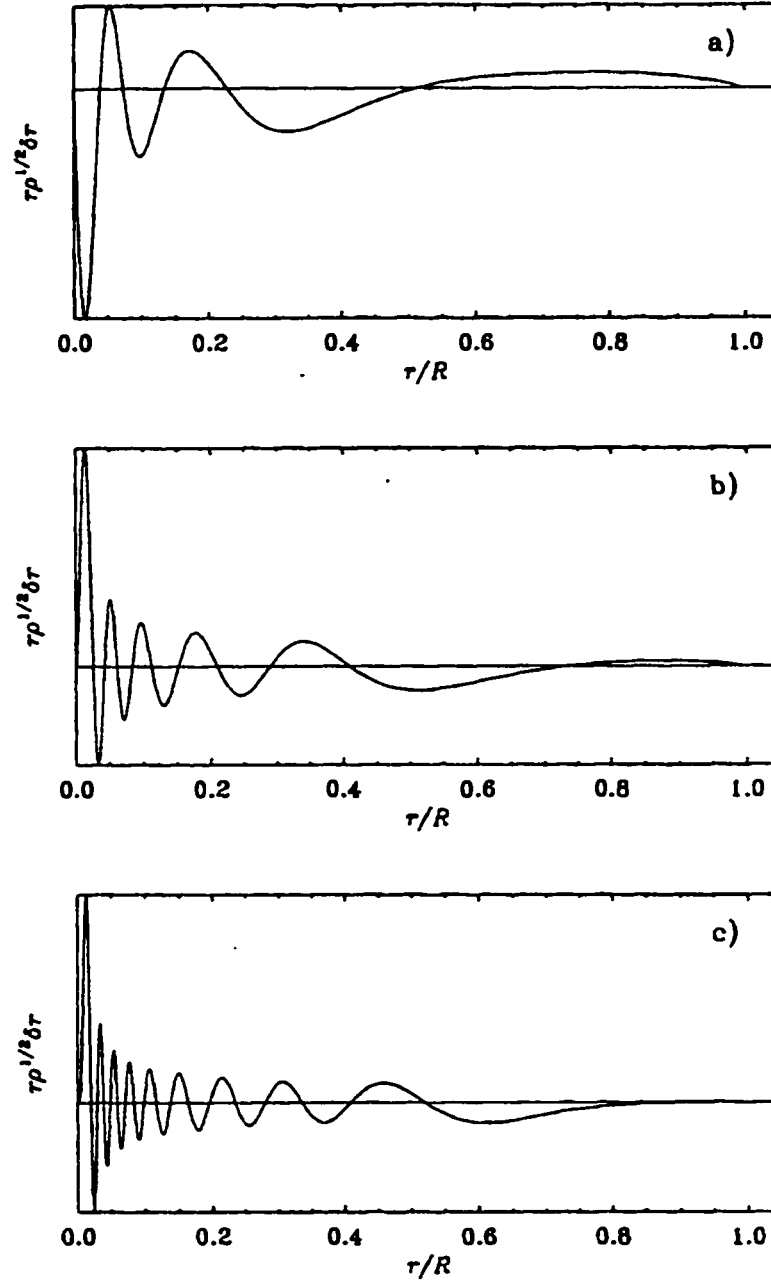


**Figure 2.5.** Eigenfunctions for selected  $g$ -modes in a normal solar model, with a)  $l = 1$ ,  $n = -5$ ,  $\nu = 110 \mu\text{Hz}$ ; b)  $l = 2$ ,  $n = -10$ ,  $\nu = 104 \mu\text{Hz}$ ; c)  $l = 4$ ,  $n = -18$ ,  $\nu = 106 \mu\text{Hz}$ . Note that the energy density, hence amplitudes, are greatest in the central regions of the star.

mode. Accurate determinations of the frequencies can give information about the physical nature of the star, through helioseismic inversion, above the turning point.

The locations of the inner turning points and surface reflection layers are very sensitive to the physical properties of the stellar model, and inspections reveal that the coefficients of the eigenfunctions are determined by the equilibrium variables  $\rho$ ,  $p$ ,  $\Gamma_1$ ,  $g$  (acceleration because of gravity) as a function of radius,  $r$ . However, only the functions  $\rho(r)$  and  $\Gamma_1(r)$  are independent, so adiabatic oscillations are determined solely by those functions.

Similarly to  $p$ -modes, the turning point for  $g$ -modes is determined by the condition incorporating the Brunt-Väisälä and angular frequencies.

$$N = \omega_{nl}$$

or

$$\sqrt{g \left[ \frac{1}{\Gamma_1} \frac{d \ln P}{dr} - \frac{d \ln \rho}{dr} \right]} = 2\pi v_{nl} \quad (2.11)$$

The majority of  $g$ -mode turning points are located deep in the stellar interior.

Figure 2.5 (analogous to Figure 2.4) shows that higher amplitude  $g$ -modes are located near the stellar core and are almost non-existent near the stellar surface (especially for modes of high harmonic degree).

## 2.2.4 Acoustic Cutoff

Similar to the turning point in the stellar interior, an oscillation must be reflected at the stellar surface to create the cavity (Figure 2.3). The reason for the surface reflection is analogous to that of light reflecting off the inside of a prism.

There is, however, a frequency maximum that an mode can have, and above which it simply dissipates into the atmosphere. It is called the acoustic cutoff frequency, given by (for an isothermal atmosphere and constant mean molecular weight,  $\mu$ ),

$$\omega_{ac} = \frac{c_s}{2H} = \frac{\Gamma_1}{2c_s} \quad (2.12)$$

where  $H$  is the pressure scale height in this simplified case.

$$H_p = -\frac{dr}{d \ln P} \quad (2.13)$$

The cutoff frequency is where the scale height becomes small relative to the wavelength of the oscillation, i.e. large frequencies. For the Sun ( $H \sim 120$  km) the acoustic cutoff frequency works out to be about 5000  $\mu\text{Hz}$ , or a period of about 3 minutes. For an example in this work see Chapter 4 on  $\beta$  Hydri, Figure 2.6. Here  $\omega_{ac} \sim 1414$   $\mu\text{Hz}$  and effects the results for frequencies with radial order  $n \geq 25$ .

## 2.3 Asymptotic Theory

References to asymptotic theory can be found in almost any research paper about asteroseismology. A few such papers are Brown & Gilliland (1994), Guenther *et al.* (1992b) for solar  $g$ -modes, Christensen-Dalsgaard and Frandsen (1988), Unno *et al.* (1989), Cox (1980), and Tassoul (1980).

Basically, asymptotic theory provides useful formulae describing the lowest order dependencies of the oscillation frequencies. One of the underlying assumptions for the application of asymptotic theory is that the radial order be much greater than the harmonic degree,  $n \gg l$ . That simplifies matters greatly since observational

asteroseismology is currently only sensitive to frequencies of low harmonic degree,  $l = 0, 1, 2, 3$ . Higher values of  $l$  suffer a cancellation effect (sign/Doppler changes) across the disk-integrated starlight since the star is unresolved by the telescope.

### 2.3.1 Asymptotic Formula for $p$ -modes

From the asymptotic analysis of Tassoul, we have to first order that the  $p$ -mode frequencies of high radial order  $n$  and low harmonic degree  $l$  are given by:

$$\nu_{nl} = \frac{\omega_{nl}}{2\pi} \equiv \left( n + \frac{l}{2} + \frac{1}{4} + \alpha \right) \Delta\nu \quad (2.14)$$

where  $\alpha$  is a phase constant resulting from the inclusion of the outer (surface) turning point, hence  $\alpha$  is determined by the physical properties of the outer layers of the star. Frequencies ( $\nu_{nl}$ ) will not be observed right away because it takes a longer integration time to identify them ( $\sim 2$  weeks).  $\Delta\nu$  is the large frequency spacing, which will be identified in the observational data obtained by the MOST and MONS missions. Physically, the large frequency spacing is the sound travel time between the centre and the stellar surface,

$$\Delta\nu = \left[ \int_0^R \frac{dr}{c_r} \right]^{-1} = \nu_{nl} - \nu_{n-1,l} \quad (2.15)$$

Asymptotic theory predicts a uniform spacing,  $\Delta\nu$  (Equation 2.15) in  $n$  for frequencies of low degree modes. In addition, modes with the same  $n + l/2$  value are almost degenerate:

$$\nu_{nl} \equiv \nu_{n-1,l+2} \quad (2.16)$$

Equation 2.14, however, is not quite complete in that deviations from the equation can be used to infer stellar structure. What must be considered is the variation of  $c_s$  in the core (Gough 1986). Using such information Tassoul (1980) analyzed the oscillation equations to higher-order and obtained:

$$\nu_{nl} = \frac{\omega_{nl}}{2\pi} \equiv \left(n + \frac{l}{2} + \frac{1}{4} + \alpha\right) \Delta\nu - (AL^2 - \delta) \frac{\Delta\nu^2}{\nu_{nl}} \quad (2.17)$$

where,

$$A = \frac{1}{4\pi^2 \Delta\nu} \left[ \frac{c_s(R)}{R} - \int_0^R \frac{dc_s}{dr} \frac{dr}{r} \right] \quad (2.18)$$

This gives the small frequency spacing:

$$\delta\nu_{nl} \equiv \nu_{nl} - \nu_{n-1, l+2} \equiv -(4l+6) \frac{\Delta\nu}{4\pi^2 \nu_{nl}} \int_0^R \frac{dc_s}{dr} \frac{dr}{c_s} \quad (2.19)$$

It is convenient to write the spacing frequencies averaged over  $n$ ,

$$\langle \delta\nu_{nl} \rangle_n \equiv (4l+6) D_o \quad (2.20)$$

where,

$$D_o \equiv -\frac{1}{4\pi^2 x_o} \int_0^R \frac{dc}{dr} \frac{dr}{r} \quad (2.21)$$

with  $x_o$  being a suitable reference value for a polynomial fit to the quantity  $x - x_o$ , where  $x = n + l/2$ .

If and when the small spacing is observed,  $D_o$  is usually determined from Equation 2.20, which approximates to:

$$D_o = \frac{\delta\nu}{6} \quad (2.22)$$

The factor  $4l$  in Equation 2.20 can be neglected because the wave vector is almost vertical (except near the core) and independent of horizontal structure, i.e. the harmonic degree  $l$  behaves as a radial mode ( $l = 0$ ).

It is the small frequency spacing that is very sensitive to the conditions in the stellar core.  $\delta\nu_{nl}$  is determined mainly by the sound speed gradient, which is a function of composition and hence the state of evolution of the star (i.e. age).  $\delta\nu_{nl}$  decreases with age since the sound speed gradient,  $dc_s/dr$ , is positive and increases with age because of the increase in the mean molecular weight,  $\mu$ , with evolution; recall for an ideal gas:

$$c_s = \frac{k_B T}{\mu m_H} \text{ so, as age } \uparrow, \frac{dc_s}{dr} \uparrow \Rightarrow \delta\nu_{nl} \downarrow \quad (2.23)$$

Successful observations of  $\Delta\nu_{nl}$  and  $\delta\nu_{nl}$ , along with accurate stellar models, may allow the determination of the evolutionary state and mass of a star (Christensen-Dalsgaard 1987; Ulrich 1986, 1988).

## 2.4 Driving and Excitation Mechanisms

Now that the nomenclature of the stellar pulsations is established, I will give a brief overview of what drives and excites the oscillation modes. Non-radial oscillations do not last forever and not all modes are excited at a specific time, which leads to different possible driving mechanisms. My specific interest is in the solar oscillations, since they are what are expected to be observed on solar-type stars.

### 2.4.1 $\epsilon$ Mechanism

First suggested by Eddington (1926), one of the driving mechanisms for oscillations is a thermodynamic heat engine. The core of a star is a place where perturbations in the energy generation rate,  $\epsilon$ , can drive oscillations. Unno *et al.* (1989) gave a detailed discussion of the specific contributions of the energy generation reactions (p-p chain, CNO, etc), and the instability of the lower order  $g$ -modes due to the  $\epsilon$ -mechanism (from Christensen-Dalsgaard *et al.* 1974; Shibahashi *et al.* 1975).

Christensen-Dalsgaard (1998) provides a detailed explanation of the instability of the modes tied to the energy generation rate. A mode is driven (damped) in regions where the work integral,  $dw/dr$ , is positive (negative), and is explained by the operation of a normal heat engine. The compression of gas in the core causes an increase in the release of energy; the gas then expands back toward equilibrium, which cools the gas and lowers the energy production; the system again collapses towards equilibrium. Both effects drive the oscillations, but such oscillations are difficult to detect since they are smaller in amplitude (and located in the deep interior) than their five-minute oscillation counterparts.

### 2.4.2 $\kappa$ - Mechanism

The  $\kappa$ -mechanism, also called the *Eddington valve*, results from an increase in opacity with compression. If and when the gas becomes more compressed, the flux of radiation outward is more strongly absorbed, increasing the pressure, which moves the entire layer upward where it cools and releases the stored energy. Such heating of the gas contributes to the excitation of the oscillations (Christensen-Dalsgaard 1998).

The simplest expression for opacity is Kramers Law (H. A. Kramers in 1923 using classical physics and the Rosseland mean; e.g. Hansen and Kawaler 1994):

$$\kappa = \kappa_o \frac{\rho}{T^{3.5}} \quad (2.24)$$

where  $\kappa_o$  is a constant. The opacity usually decreases with compression because of the strong temperature dependence.

There do exist regions in a star where the density increase is large enough to increase the opacity; they are called partial ionization zones. Such regions were first identified by Zhevakin (1963), and the calculations which followed by Kippenhahn and Baker (1965) and Cox (1968) showed that there exists a layer of partially ionized atoms in such zones. When this layer is compressed, the work done on the gas causes more ionization instead of increasing the temperature. When the layer expands, a similar process occurs because of electron recombination. The cyclic process amplifies stellar oscillations and is responsible for the instability strip in the HR-diagram.

### 2.4.3 Five-Minute Oscillations: Turbulent Convection

The above excitation mechanisms can occur in many types of stars, but a third mechanism of special interest to this work is the excitation of the solar five-minute oscillations. Such global oscillations are expected to be observed on the solar-type targets of MOST and MONS (or any solar-type star for that matter). Unno *et al.* (1989, § 42 p. 365) give a detailed discussion of the excitation mechanism, and much of the information below comes from their work. Today we believe some form of stochastic excitation by turbulent convection is responsible for driving the  $p$ -modes. The possibility of a stochastic process was first examined by Goldreich and Keeley (1977), and later by



Kumar, Franklin, and Goldreich (1988). The method is similar to when oscillations of a system are excited at resonant frequencies and maintained by Brownian motion of individual particles. The energy of the oscillations is in agreement with observations and can explain the five-minute oscillation amplitudes (Goldreich and Kumar 1988).

It is generally assumed that the stochastic process is acoustic noise in the Sun's (star's) resonant cavity, which is generated by the high speed convective motions within a few scale heights of the solar surface (Goldreich and Kumar 1990; Cox *et al.* 1991; Kumar and Lu 1991). It follows that all stars with vigorous surface convection zones should harbour some type of five-minute oscillations. Recent numerical models of solar convection by the Yale convection group do show how  $p$ -modes can be excited by convection (Guenther, private communication).

Recently, Samadi and Goupil (2001) implemented a generalized theoretical formulation for excitation by turbulent convection. Although not three-dimensional (it is in the works; Samadi 2000), the formulation permits investigations of various possible spatial and temporal spectra of stellar convection. Their work yields the oscillation amplitude of a stellar mode when it is stochastically excited by turbulent convection. Applying the formulation to the Sun shows that the entropy source significantly contributes to the stochastic excitation of the modes (Samadi, Goupil, and Lebreton 2001).

Nigan and Kosovichev (1999) used the Michelson Doppler Imager on board the Solar and Heliospheric Observatory (SOHO) to search for the actual source of the solar acoustic modes. Their results are exciting since they estimate the source to be a very thin, superadiabatic layer of turbulent convection about  $75 \pm 50$  km below the

photosphere. To obtain such information they compared the theoretical power spectra of both velocity and pressure with the SOHO observations. Their finding is in agreement with the notion that the five-minute oscillations are of high frequency and have turning points very near the solar surface (Kumar and Lu 1991).

One last thing that should be mentioned is the fate of an oscillation. Just how long a perturbation lasts depends on the competition between the driving and damping mechanisms (Christensen-Dalsgaard *et al.* 1989). Solar  $p$ -modes have lifetimes on the order of 10 hours to 10 days for high and low  $l$ , respectively (Chen *et al.* 1996).

## **2.5 Yale Stellar Evolution Code with Rotation: YREC**

In order to produce any kind of pulsation spectrum, a detailed stellar structure model is required. That task was accomplished using YREC in its non-rotating format (Prather 1976; Pinsky 1988; Guenther *et al.* 1992a, b; Guenther, Kim, and Demarque 1996). YREC solves the time-independent stellar structure equations (derived in Schwarzschild 1958; and Clayton 1968).

The code uses the Henyey relaxation method, which iterates an initial model to specified tolerances, to solve the boundary value problem. Approximately 600-750 shells are used to model the interior and envelope region of a main-sequence star; the more evolved the star the higher the number of shells. The atmosphere model is kept simple. For this work I use a gray atmosphere, but YREC is capable of using the Krishna Swamy (1966)  $T - \tau$  relation. For each interior shell in the model, the nuclear reaction network is solved.

### **2.5.1 Opacities**

The latest version of YREC implements the Lawrence Livermore National Laboratory (LLNL; Rogers 1986; Rogers, Swenson, and Iglesias 1996) OPAL opacities and equation-of-state. For each stellar metallicity value used, the EOS for the interior was interpolated from the above opacity tables. Cooler envelopes and atmospheres ( $\log T < 4.0$ ) utilized the Alexander 95 (Alexander and Ferguson 1994) opacity tables. The OPAL opacities include all stages of ionization and excitation.

### **2.5.2 Diffusion**

The models generated here utilized YREC's capability to implement diffusion or non-diffusion of helium and heavy elements. The concept of including diffusion of helium was first proposed by Michaud (1970), and its importance in stars with thick convection zones was made evident in Michaud (1986). The inclusion of helium and heavy element diffusion produces a more accurate agreement between the theoretical and observed pulsation spectra of the standard solar model (Däppen and Gough 1986; Antia and Basu 1994; Guenther and Demarque 1997). The implications of diffusion are discussed in the pulsation results of  $\epsilon$  Eridani and  $\beta$  Hydri (recall that all  $\beta$  Gem models do not include diffusion of any elements).

### **2.5.3 Convection**

To date there still does not exist a theory that rigorously describes the convection phenomenon that occurs in many stars. That is unfortunate because it is probably turbulent convection itself that is responsible for the observed five-minute oscillations.

The most common technique employed to model convection is mixing length theory, first introduced by Böhm-Vitense (1958). It is a very crude approximation, and assumes that convective energy is carried a mixing length  $l$  (not to be confused with the harmonic degree  $l$ ) in a convective bubble that instantaneously dissipates through radiative diffusion. The distance the bubble will rise is proportional to the pressure scale height,  $H_p$  (Equation 2.13), which gives the parameterization:

$$l = \alpha H_p \quad (2.25)$$

where  $\alpha$  is termed the mixing length parameter.

The value of  $\alpha$  is sensitive to the choice of the model parameters (atmosphere model,  $T_{\text{eff}}$ , luminosity, diffusion, etc.), and is determined empirically. The standard solar model (SSM) has a mixing length parameter  $\alpha = 2.087$  (Guenther and Demarque 2000), and was determined using the latest opacity tables, a Krishna Swamy model atmosphere, and diffusion of helium and heavy elements.

This thesis does not employ the SSM or a Krishna Swamy model atmosphere, and because there is no means to produce a unique value of  $\alpha$  for each star, a new solar mixing length parameter was calibrated for a gray atmosphere for both the diffusion and non-diffusion cases. The task is easily handled by the solar calibration feature of YREC, which automatically produces a model with a solar mass, luminosity, and effective temperature by tuning  $\alpha$  to match the observational luminosity, effective temperature, and composition ( $Z/X = 0.0245$ ; Grevesse *et al.* 1996). After a few iterations a solar mixing length parameter is determined for each case of diffusion and non-diffusion, and it is these values which are implemented in the stellar models described in this work:  $\alpha_{\text{diff}} = 1.73141$ , and  $\alpha_{\text{nondiff}} = 1.6047$ .

The calibration function of YREC also works the other way — taking a mixing length parameter and producing a tuned stellar model of a given luminosity and effective temperature by adjusting the composition. It is this calibration feature that was used to produce the stellar models presented here. The mixing length parameters was calibrated for the Sun and used for the stellar models. Note, however, that the giant star  $\beta$  Gem was treated slightly differently; see Chapter 5 for further details.

## 2.6 The Pulsation Code

The non-radial, non-adiabatic pulsation code of Guenther (1994) was used to produce a spectrum spanning the modes  $l = 0, 1, 2$ , and averaged over  $1 \leq n \leq 30$ . The code has the capability of producing higher order modes, but only the lower order modes will be observable.

The pulsation code utilizes the stellar structure output of YREC and operates in five steps (see Guenther 1994 for more specific details):

1. After an initial guess for the  $l$ -value and oscillation frequency are given, the code calculates the turning point (Equation 2.10) from the stellar model's run of sound speed.
2. The linearized adiabatic equations of stellar oscillations are solved using the Henyey method. The outer boundary conditions are removed. The process produces an initial guess for the adiabatic frequencies. The equations are given in Unno *et al.* (1989, § 14).
3. The solution from Step (2) is used to solve the complete set of linearized equations. The solution is converged by the method of relaxation.

4. Next the work integral,  $W(r)$ , and kinetic energy,  $w_k$ , are calculated:

$$W(r) = -4\pi^2 r^2 \text{Im}((\delta p^*) \xi_r) , \quad (2.26)$$

$$w_k = \frac{1}{2} \omega_{ad}^2 \int_0^M |\delta r|^2 dm \quad (2.27)$$

where  $\delta p$  is the Lagrangian pressure variation and  $\xi_r$  is the radial component of the displacement vector  $\delta \mathbf{r}$ . That produces the non-adiabatic eigenfunctions in conjunction with the results from Step (3). The work integral represents the amount of energy gained at the surface by the oscillation over the adiabatic cycle. A positive work integral implies mode excitation, and a negative value implies that the mode is damped.

5. With the eigenfunctions of Step (4), the complete eigenfunctions for the non-adiabatic frequencies are calculated from the equations of Saio and Cox (1980) governing the non-adiabatic, non-radial oscillations of a static star.

The non-adiabatic iteration may converge to the incorrect mode (i.e. higher or lower  $n$ ) if the non-adiabatic frequency differs from the adiabatic frequency by more than the large frequency spacing between the modes. The effects of the non-adiabatic treatment increases with frequency because of the large concentration of nodes near the stellar surface from eigenfunctions with high frequencies.

# Chapter 3

## $\epsilon$ Eridani

### 3. Introduction

At a distance of about 3.22 parsecs, the K2 V star  $\epsilon$  Eridani (HIP 16537, HD 22049) is one of our solar system's nearest neighbors. Even though its proximity allows for the possibility of accurate data measurements of say luminosity, there is a large scatter in the various derived physical parameters. This chapter will review the current fundamental parameters of  $\epsilon$  Eridani as well as derive new ones that are to be used for stellar modeling and seismology analysis. Aside from discussing the controversy over some of  $\epsilon$  Eridani's observational parameters, this chapter is also used as a guide for the methodology applied in analyzing the MOST and MONS target stars discussed in this work.

### 3.1 Magnitude, Colours, and Parallax

For the ensuing analysis of the K2 V star  $\epsilon$  Eridani, only the apparent magnitude, B-V, and parallax were required. Refer to Table 3.1 for a summary of the data from the literature.

**Table 3.1** Observational parameters.

$m_v (\pm \Delta m_v)$	$B-V (\pm \Delta(B-V))$	$\pi'' (\pm \Delta\pi)$	Reference
3.73 (0.03)	(N/A)	0.303 (0.004)	Guenther & Demarque (1986)
3.728 (0.039)	0.885 (0.024)	0.3046 (0.0046)	Soderblom & Däppen (1989)
3.72 (N/A)	0.881 (0.007)	0.31075 (0.00085)	Hipparcos

I used the Hipparcos values, but note that the Hipparcos value for the apparent visual magnitude  $V$  is taken from the literature and the  $B-V$  is their own value after it is adjusted to the UBV system. The Hipparcos catalogue did not give an uncertainty for the apparent magnitude, so I applied the uncertainty used by Soderblom and Däppen (1989) to take into account systematic errors. The resulting absolute visual magnitude calculated from the parallax and apparent magnitude is  $M_v = 6.18 \pm 0.04$ .

### 3.2 Effective Temperature, Surface Gravity, and Metallicity

The effective temperature of  $\epsilon$  Eridani is probably its most precisely known parameter. Many published values do not vary by more than 100 K about the  $T_{\text{eff}}$  value of 5100 K. Krishna Swamy (1966), Hearnshaw (1974), Guenther & Demarque (1986) (hereafter GD86), Bell & Gustafsson (1989), Soderblom & Däppen (1989), and Drake & Smith (1993) are a few of the authors who have used effective temperature values in the range of  $5000 \leq T_{\text{eff}} \leq 5200$  K. The majority quote a photometrically determined effective temperature, and it was only Krishna Swamy (1966) and Drake & Smith (1993) who determined  $T_{\text{eff}}$  spectroscopically. This work adopts Drake and Smith's (1993, hereafter DS93) value of  $T_{\text{eff}} = 5180 \pm 50$  K.

The surface gravity of  $\epsilon$  Eridani is not a crucial parameter for the purpose of the project. Stellar evolution models generate a value for the surface gravity given the computationally determined mass and radius of the star. The only knowledge required is an approximate range of values for the surface gravity to be used as a guide in determining the bolometric correction (§ 3.3). Table 1 in DS93 lists some of the



previously determined values for  $\log g$  which range from 4.1 – 4.8. The value of  $\log g = 4.75 \pm 0.1$  determined by DS93 was used as the reference value when interpolating the Green *et al.*(1987) colour tables to derive the bolometric correction.

Unlike the general agreement for the value of  $\epsilon$  Eridani's effective temperature, its estimated metallicity can be found to vary from  $[\text{Fe}/\text{H}] = +0.10$  to  $-0.50$  in the literature. GD86 used a value of  $-0.19 \pm 0.30$  to account for the different solutions of  $-0.19$ ,  $-0.31$ , and  $-0.20$  from Oinas (1974b), Hearnshaw (1974), and Steenbock and Howleger (1981) respectively. Similarly, Soderblom and Däppen (1989), hereafter SD89, adopted  $[\text{Fe}/\text{H}] = -0.23$  and used  $Z$  values of 0.01-0.04 ( $Z_{\odot} = 0.0188$ ) for their respective models.

As with the choice of effective temperature and surface gravity, this project will again use the work of DS93. With the Fe I and Fe II lines in a spectroscopic analysis of  $\epsilon$  Eridani, DS93 retrieve a value of  $[\text{Fe}/\text{H}] = -0.09 \pm 0.05$ , or  $Z/X = 0.02 \pm 0.006$  ( $(Z/X)_{\odot} = 0.0245 \pm 0.007$  (Grevesse *et al.* 1996)).

### 3.3 Bolometric Correction and Luminosity

The bolometric correction for  $\epsilon$  Eridani (and all target stars) was obtained by linearly interpolating the colour-corrections table from Green *et al.* (1987) in  $B-V$ ,  $T_{\text{eff}}$ , and  $[\text{Fe}/\text{H}]$ . The data from Green *et al.* (1987) and  $\epsilon$  Eridani's parameters are given in Table 3.2. The interpolation of the 3-dimensional colour table is calculated as an example below.

The process for determining the bolometric correction is outlined in detail in the example below. The derived bolometric correction,  $\text{B.C.} = -0.216 \pm 0.009$ , falls nicely

between the values obtained by Johnson (1966) and Hayes (1978) of  $-0.207$  and  $-0.315$  magnitude, respectively.

The uncertainty in the bolometric correction was obtained by separately interpolating the colour-correction tables at the extreme of the  $B-V$ ,  $T_{\text{eff}}$ , and  $[\text{Fe}/\text{H}]$  values. The final result for the uncertainty is then the square root of the sum of the squares of each separately determined uncertainty [i.e. interpolate using  $B-V + \Delta(B-V)$ , then  $B-V - \Delta(B-V)$  and recording the range of values].

**Table 3.2** Top: Colour-Correction data from Green *et al.* (1987). The lower table contains the required parameters for  $\epsilon$  Eridani. See text for the calculations.

$[\text{Fe}/\text{H}]$	$T_{\text{eff}}$ (K)	$\text{Log } g$	B.C.	U-B	B-V	V-R	R-I
0.00	5000	4.00	$-0.232$	0.568	0.883	0.487	0.439
0.00	5000	4.50	$-0.281$	0.630	0.919	0.517	0.451
0.00	5500	5.50	$-0.174$	0.420	0.834	0.447	0.387
0.00	5500	6.00	$-0.191$	0.510	0.893	0.464	0.391
$-0.50$	5000	4.00	$-0.253$	0.418	0.835	0.469	0.441
$-0.50$	5000	4.50	$-0.277$	0.464	0.859	0.490	0.449
$-0.50$	5500	5.50	$-0.136$	0.207	0.756	0.415	0.386
$-0.50$	5500	6.00	$-0.129$	0.257	0.795	0.426	0.392

---

**Interpolation Required Values**

---

B-V.....	$0.881 \pm 0.007$ mag
$T_{\text{eff}}$ .....	$5180 \pm 50$ K
$[\text{Fe}/\text{H}]$ .....	$-0.09 \pm 0.05$

---

The first step is to determine the metallicity range such that  $\epsilon$  Eridani's metallicity lies in between. Then, at each metallicity a temperature range is defined, and subsequently for each temperature a  $B-V$  range. If  $\epsilon$  Eridani's  $B-V$  colour does not fall between two of the table's  $B-V$  values, then the last two  $B-V$  values are used. The following example will clarify the process, and the results are summarized in Table 3.3 following the example.

$$\frac{(-0.281) - (-0.232)}{(-0.919) - (0.883)} = \frac{(-0.281) - (B.C_1)}{(0.919) - (0.881)}$$

Start at  $[\text{Fe}/\text{H}] = 0.00$  and  $T_{\text{eff}} = 5000$  with the first interpolation in B–V. This gives the first bolometric correction.

$$B.C_1 = -0.229$$

$$\frac{(-0.191) - (-0.175)}{(0.893) - (0.834)} = \frac{(-0.191) - (B.C_2)}{(0.893) - (0.881)}$$

Interpolate in B–V at high end of  $T_{\text{eff}} = 5500$  and same  $[\text{Fe}/\text{H}]$ .

$$B.C_2 = -0.188$$

$$\frac{(-0.188) - (-0.229)}{(5500) - (5000)} = \frac{(-0.188) - (B.C_3)}{(5500) - (5180)}$$

Interpolate in  $T_{\text{eff}}$  using  $B.C_1$  and  $B.C_2$  to produce bolometric correction at  $[\text{Fe}/\text{H}] = 0.00$ .

$$B.C_3 = -0.214$$

$$\frac{(-0.289) - (-0.277)}{(0.891) - (0.859)} = \frac{(-0.289) - (B.C_4)}{(0.891) - (0.881)}$$

Begin same process but for data at the  $[\text{Fe}/\text{H}] = -0.50$ . Here  $T_{\text{eff}} = 5000$ .

$$B.C_4 = -0.285$$

$$\frac{(-0.129) - (-0.136)}{(0.795) - (0.756)} = \frac{(-0.129) - (B.C_5)}{(0.795) - (0.881)}$$

Interpolate in B–V at  $T_{\text{eff}} = 5500$ .

$$B.C_5 = -0.114$$

$$\frac{(-0.114) - (0.285)}{(5500) - (5000)} = \frac{(-0.114) - B.C_6}{(5500) - (5180)}$$

Interpolation in  $T_{\text{eff}}$ .

$$B.C_6 = -0.224$$

$$\frac{(-0.224) - (-0.214)}{(-0.50) - (0.00)} = \frac{(-0.224) - (B.C_{\text{final}})}{(-0.50) - (-0.09)}$$

Interpolation in the  $[\text{Fe}/\text{H}]$  values which produces the final bolometric correction for  $\epsilon$  Eridani. This value is used to calculate  $M_{\text{bol}}$  and the luminosity.

$$\Rightarrow B.C_{\text{final}} = -0.216$$

**Table 3.3** Summary of parameters calculated with the derived bolometric correction. This is the luminosity that will be used for stellar modeling.

<b>Results of Bolometric Correction Determination</b>	
B.C.....	$-0.216 \pm 0.009$
$M_v$ .....	$6.18 \pm 0.040$
$M_{bol}$ .....	$5.97 \pm 0.041$
$\log L/L_{\odot}$ .....	$-0.471 \pm 0.017$
$R/R_{\odot}$ .....	$0.724 \pm 0.020$

### 3.4 Mass

A review of the search a stellar companion in orbit about  $\epsilon$  Eridani proved inconclusive, and the only possibility for the system to escape detection by speckle interferometry and radial velocity measurements is for it to be nearly face-on (Guenther 1987). The Hipparcos catalogue also does not list  $\epsilon$  Eridani as being a member of a multiple system. Without a stellar companion,  $\epsilon$  Eridani's mass can only be determined by comparison with stellar models.

Drake and Smith (1993), hereafter DS93, obtained a mass,  $M = 1.0 \pm 0.3 M_{\odot}$  from the following observational data:  $T_{eff} = 5180$  K,  $\log g = 4.75 \pm 0.1$ , and  $\log L/L_{\odot} = -0.48 \pm 0.04$  determined by SD89. These stellar parameters are consistent with a  $0.80 M_{\odot}$  theoretical ZAMS model from VandenBerg and Bridges (1984). The process of mass determination assumes  $\epsilon$  Eridani has an age of zero Gyr (i.e. the starting model is used and no evolution takes place). DS93 adapt SD89's age estimate of less than one billion years, and since low mass stars take longer to reach the ZAMS it is justified for them to assume an age of zero Gyr for ZAMS fitting.

Detailed stellar evolution model fitting of  $\epsilon$  Eridani was carried out by GD86 and SD89, who found masses of  $0.80 M_{\odot}$  and  $0.78 M_{\odot}$ , respectively, for their best-fit models.

Their models were generated to test  $\epsilon$  Eridani's observed  $p$ -mode and characteristic frequency spacing (§ 3.5) observationally determined by Noyes *et al.* (1984). The general consensus is that the mass of  $\epsilon$  Eridani is less than one solar mass, and I adopt  $M = 0.78 \pm 0.02 M_{\odot}$  to cover the range of values determined by the above authors.

### 3.5 Seismology: Age and Mixing Length Parameter

The first, and to date, only observation of global oscillations on  $\epsilon$  Eridani was made by Noyes *et al.* (1984). The  $p$ -mode oscillations were measured from the intensity variations of the chromospheric Ca II H and K lines, found to be on the order of several hundred times larger than solar, and the period of the oscillations were on the order of 10 minutes, twice as long as the 5-minute oscillations observed on the Sun. The subsequent power spectra revealed a large frequency spacing of,  $\Delta\nu_0 = 172 \pm 5 \mu\text{Hz}$ .

The large frequency spacing permits for a detailed seismological study of  $\epsilon$  Eridani. As mentioned in § 3.4, GD86 and SD89 carried out two such studies, and whose objectives were to produce a stellar model that fit the photometric data and compare the model and observed seismological data.

**Table 3.4** Input parameters used by SD89 and GD86.

Parameter	SD89	GD86
$M_{\text{bol}}$ .....	$5.94 \pm 0.09$	$5.85 \pm 0.04$
$\log L/L_{\odot}$ .....	$-0.48 \pm 0.04$	$-0.44 \pm 0.02$
$\log R/R_{\odot}$ .....	$-0.12 \pm 0.05$	determined
$\log T_{\text{eff}}$ .....	$3.699 \pm 0.008$	$3.700 \pm 0.0016$
$T_{\text{eff}}$ (K).....	$5000 \pm 100$	$5000 \pm 200$
Z.....	0.01–0.02	0.01–0.04
Y.....	0.24–0.26	0.23–0.24
X.....	0.73–0.75	0.74–0.76

GD86 started by generating an assortment of models varying in both mass and metallicity (see Table 3.4 for input parameters). However, their results, models 1–6 and 9 in Table 3.5, were not consistent with the observed frequency spacing  $\Delta\nu_0$ , and in some cases the age of the universe. In order to constrain  $\epsilon$  Eridani's age within  $\sim 12$  Gyr, GD86 had to introduce the mixing length parameter,  $\alpha$ , into their parameter space. The mixing length parameter had to be changed from the (then) solar value of  $\alpha = 1.37$  to a lower value  $\alpha \sim 1.00$ . The new value directly effects  $\epsilon$  Eridani's physical and chemical evolution, resulting in a larger radius and age, and a lower large frequency spacing (e.g. compare models 3 & 8 in Table 3.5 where the parameters only vary by  $\alpha$ ). With this change, their best-fit model (#7) gives  $M = 0.80 M_{\odot}$ ,  $Z = 0.02$ ,  $Y = 0.236$ ,  $\alpha = 1.00$ ,  $\Delta\nu = 170.5 \mu\text{Hz}$ , and an age of 11.48 Gyr. Their only constraint, besides the observational data, was the age of the universe. SD89, however, constrained their models to be less than one Gyr.

On the basis of  $\epsilon$  Eridani's chromospherically active atmosphere (Middelkoop *et al.* 1981) and rapid rotation rate,  $P = 12.16 \pm 0.08$  days (Hallam and Wolff 1981), SD89 restricted their models to be younger than one (1) billion years old. The choice has drastic effects on the value of the mixing length parameter if the models are to stay within the boundaries of the observed data (Table 3.4).

The best-fit results found by SD89 are summarized in the bottom section of Table 3.5. The upper limit age constraint of 1 Gyr greatly reduces the mixing length parameter to  $0.50 \leq \alpha \leq 0.60$ , well below solar (current  $\alpha_{\odot} = 2.087$  Guenther & Demarque 2000). Unless the observed characteristic frequency spacing by Noyes *et al.* (1984) is in error as a result of very large amplitudes as claimed by SD89 and KB95,  $\epsilon$  Eridani can only be

**Table 3.5** Stellar Model Characteristics and results for  $\epsilon$  Eridani. Top: GD86 with  $T_{\text{eff}}$  and  $T_c$  in K, and  $\rho_c$  in  $\text{g/cm}^3$ . Bottom: Best fit results of SD89.

Model #	$M/M_{\odot}$	$m_{\text{bol}}$	$\log T_{\text{eff}}$	Z	Y	$\alpha$	Convective Envelope Mass Fraction $M/M_{\odot}$	Log $T_c$	Log $\rho_c$	$\Delta\nu$ ( $\mu\text{Hz}$ )	Age (Gyr)	Radius ( $R_{\odot}$ )
1	0.75	5.85	3.70696	0.02	0.236	1.37	0.056788	7.135922	7.135922	175.0	21.61	0.770
2	0.80	5.85	3.70924	0.02	0.230	1.37	0.053490	7.101300	7.101300	185.0	11.97	0.763
3	0.85	5.85	3.71288	0.02	0.236	1.37	0.051025	7.066150	7.066150	196.7	1.37	0.750
4	0.70	5.85	3.71880	0.01	0.236	1.37	0.043748	7.142158	7.142158	183.4	23.66	0.729
5	0.75	5.85	3.72247	0.01	0.236	1.37	0.041096	7.102340	7.102340	196.4	11.97	0.718
6	0.80	5.85	3.72483	0.01	0.236	1.37	0.038618	7.067850	7.067850	207.2	2.38	0.710
7	0.80	5.85	3.69879	0.02	0.236	1.00	0.044015	7.101074	7.101074	170.5	11.48	0.800
8	0.85	5.85	3.70187	0.02	0.236	1.00	0.041014	7.068296	7.068296	181.4	2.05	0.788
9	0.80	5.90	3.70817	0.02	0.236	1.37	0.054403	7.088824	7.088824	189.9	9.27	0.749

$M/M_{\text{sun}}$	$\alpha$	Z	Y	Age(Gyr)	$\Delta\nu(\mu\text{Hz})$
0.77	0.50	0.01	0.26	1	172
0.78	0.55	0.01	0.26	1	172
0.80	0.60	0.01	0.26	1	172

modeled using a sub-solar mixing length. The value depends on the age constraints imposed.

SD89 calculated more models (limited by the age constraint) with typical solar-scale mixing lengths and found large frequency spacing values around  $\Delta\nu = 213 \mu\text{Hz}$  (see Table 5 of SD89). This is in much better agreement with predictions,  $\Delta\nu = 204 \pm 18 \mu\text{Hz}$  (KB95; Equation 1.10), and with the results of this work (Table 3.7). KB95 pointed out that no recognizable  $p$ -mode signature is found, and the large frequency spacing was determined from only a few peaks in the power spectrum.

How old then is  $\epsilon$  Eridani? To this date there exist a wide range of possible answers, and I will be exploring the age range in detail. The stellar models generated in this work were not restricted in age. A variety of ages, and subsequent pulsation spectra, were considered for models of different initial parameters. One of the goals of this thesis is to generate a possible seismological age indicator for  $\epsilon$  Eridani.

### 3.6 Stellar Evolution Models

Observations of  $\epsilon$  Eridani revealed a large range of values in both mass and composition. To account for that I generated many models to obtain the maximum spread in parameter space. A summary of the model parameters is listed in Table 3.6. The metal abundance  $Z$  is chosen to cover the range of values used by GD86 and SD89.

**Table 3.6.** Model parameters for  $\epsilon$  Eridani.

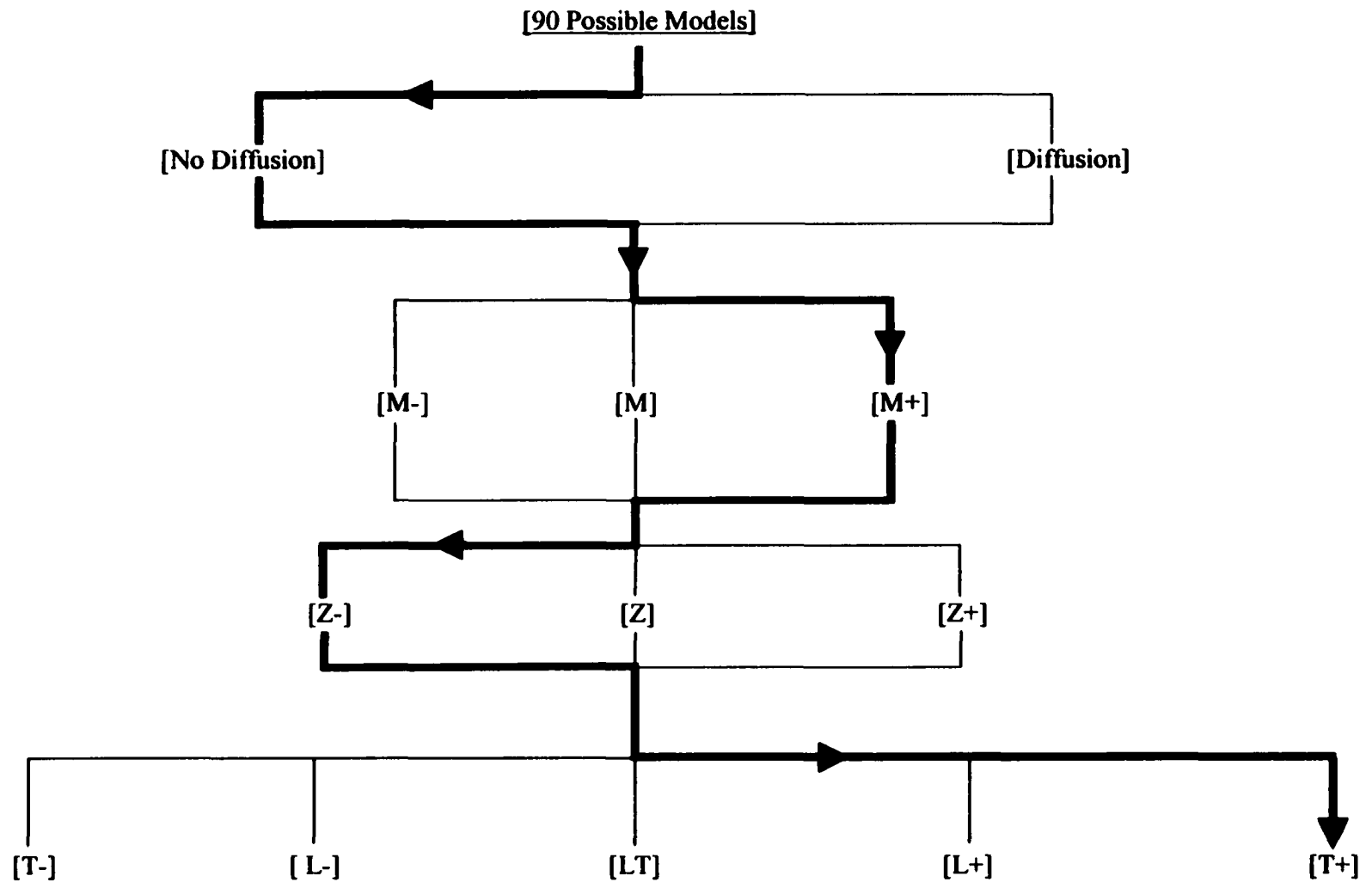
Parameter	Value
$M/M_{\odot}$ .....	$0.78 \pm 0.02$
$Z$ .....	$0.014 \pm 0.04$
$\log L/L_{\odot}$ .....	$-0.471 \pm 0.017$
$\log T_{\text{eff}}$ .....	$3.714 \pm 0.0042$



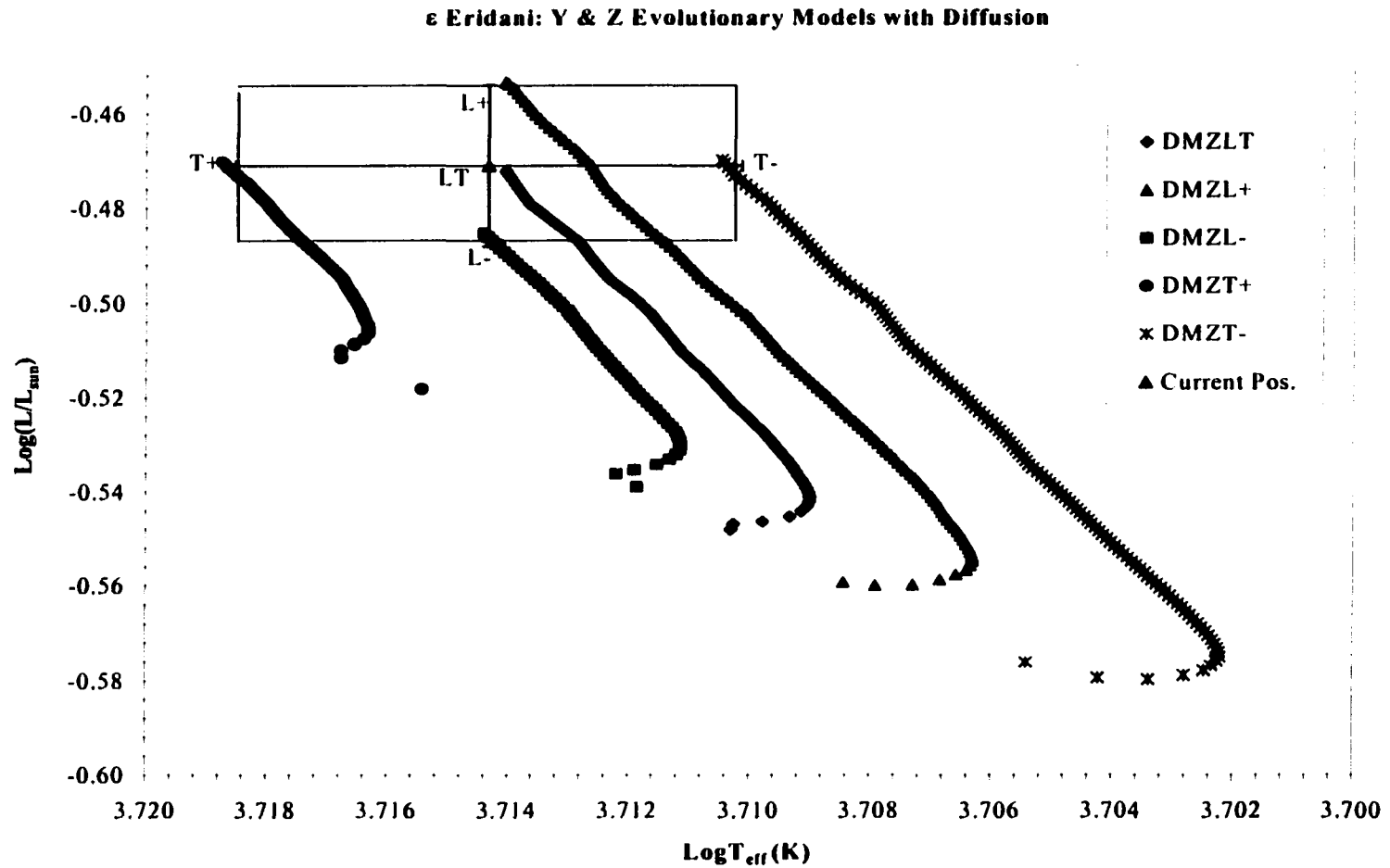
Because of the large number of models required, I use an acronym to reference each model if and when it is described in the text. Figure 3.1 is the “model tree”, which should be used as a guide in deciphering (and naming) the acronyms. Models can have either diffusion or no diffusion, then three values of mass, three values of metallicity for each mass, and one of five final positions on the HR-diagram for each metal abundance. For example the bold font path in Figure 3.1 generates the model *NDM+Z-T+*, the model evolved with no diffusion, high end of mass range, low metal abundance range, and to the extreme of the effective temperature at the reference luminosity. Note that models are evolved to the extreme of  $L$  or  $T_{\text{eff}}$  ( $L-$ ,  $L+$ ,  $T-$ , and  $T+$  in Figure 3.1), the reference  $L$  and  $T_{\text{eff}}$  (centre of observational error box,  $LT$  in Figure 3.1), and not both parameters at the same time. It is this detailed process which produces a large range of stellar evolution data, and subsequently a range of seismological data for  $\epsilon$  Eridani.

Figure 3.2 shows a set of evolutionary models, with diffusion, for a mass,  $M = 0.78M_{\odot}$ ,  $\alpha = 1.73141$ , and  $Z = 0.014$ . The models are automatically calibrated to within one percent of the desired luminosity and effective temperature (which means YREC automatically adjusts the  $X$  and  $Y$  composition to fit the model). The figure also shows how each MOST or MONS star will be modeled.  $\epsilon$  Eridani is still on the main sequence for all models, but note how the starting position, composition and evolution time must be adjusted to evolve the star to the desired HR-diagram position.

The generated models and their properties are given in Table 3.7. The first column (1) of Table 3.7 is the model reference code, i.e. the model parameters. All models in this table are DM (col. #1). Columns 2 – 13 are the model’s final hydrogen mass fraction, initial and final metallicity, age (Gyr), the logarithm of luminosity (solar



**Figure 3.1.** The “model tree” for simplifying model properties. The bold-line path is the model *NDM+Z-T+* (see text).



**Figure 3.2** Evolution models of  $\epsilon$  Eridani with:  $M = 0.78 M_{\odot}$ , and  $Z = 0.014$ .  $\epsilon$  Eridani's current position:  $\log L/L_{\odot} = -0.471 \pm 0.017$ ,  $\log T_{\text{eff}} = 3.714 \pm 0.0042$ . All models are calibrated to within 1% of the desired luminosity.

**Table 3.7.** Calibrated diffusion model output. There are 15 models total, which are evolved to  $\epsilon$  Eridani's luminosity and effective temperature limits. Refer to text for the column heading description. The model name is DM(Col. #1).

Diffusion Models, $M = 0.78 M_{\text{sun}}$					$\alpha = 1.731410$							
Mo.Ref.	$X_r$	$Z_r$	$Z_t$	Age	$\log L/L_{\text{sun}}$	$T_{\text{eff}}$ (K)	$\log g$	$\log P_c$	$\log T_c$	$\log D_c$	$X_c$	$Z_c$
Col. # 1	2	3	4	5	6	7	8	9	10	11	12	13
ZLT	0.7294	0.0140	0.0131	4.4672	-0.4722	5176	4.6106	17.2102	7.0925	2.0489	0.5257	0.0146
ZL+	0.7424	0.0140	0.0127	6.5177	-0.4533	5176	4.5918	17.2499	7.1036	2.1058	0.4538	0.0149
ZL-	0.7188	0.0140	0.0134	2.9374	-0.4851	5180	4.6250	17.1831	7.0850	2.0087	0.5815	0.0144
ZT+	0.7059	0.0140	0.0135	2.1528	-0.4701	5232	4.6273	17.1816	7.0869	1.9988	0.5994	0.0143
ZT-	0.7511	0.0140	0.0127	7.0921	-0.4697	5134	4.5938	17.2459	7.1003	2.1062	0.4509	0.0150
Z+LT	0.6884	0.0180	0.0173	3.1169	-0.4669	5192	4.6106	17.1975	7.0981	2.0269	0.5370	0.0186
Z+L+	0.7028	0.0180	0.0167	4.9936	-0.4515	5181	4.5918	17.2332	7.1080	2.0794	0.4685	0.0189
Z+L-	0.6812	0.0180	0.0175	1.8983	-0.4858	5178	4.6250	17.1707	7.0898	1.9895	0.5885	0.0183
Z+T+	0.6696	0.0180	0.0176	1.2972	-0.4715	5228	4.6273	17.1705	7.0919	1.9819	0.6028	0.0182
Z+T-	0.7130	0.0180	0.0166	5.5496	-0.4713	5129	4.5938	17.2276	7.1038	2.0789	0.4663	0.0190
Z-LT	0.7714	0.0100	0.0091	6.3116	-0.4703	5182	4.6106	17.2320	7.0898	2.0826	0.5002	0.0106
Z-L+	0.7827	0.0100	0.0089	8.4221	-0.4508	5184	4.5918	17.2729	7.1011	2.1402	0.4304	0.0108
Z-L-	0.7625	0.0100	0.0093	4.6898	-0.4859	5178	4.6250	17.2023	7.0813	2.0398	0.5573	0.0105
Z-T+	0.7464	0.0100	0.0095	3.4933	-0.4685	5237	4.6273	17.1982	7.0831	2.0247	0.5825	0.0103
Z-T-	0.7937	0.0100	0.0088	9.4047	-0.4680	5139	4.5938	17.2724	7.0983	2.1461	0.4214	0.0109

**Table 3.7 Continued. Seismology data.**

Mo.Ref.	Big, l=0 $\Delta v$ ( $\mu\text{Hz}$ )			Big, l=1 $\Delta v$ ( $\mu\text{Hz}$ )			Big, l=2 $\Delta v$ ( $\mu\text{Hz}$ )			Small, l=0 $\delta v$ ( $\mu\text{Hz}$ )		
	n=1-10	n=10-20	n=20-30	n=1-10	n=10-20	n=20-30	n=1-10	n=10-20	n=20-30	n=1-10	n=10-20	n=20-30
	14	15	16	17	18	19	20	21	22	23	24	25
ZLT	209.401	195.163	194.965	213.484	195.124	195.183	206.918	195.243	195.336	22.855	17.309	12.666
ZL+	200.789	188.809	188.958	203.248	188.809	189.017	198.730	188.892	189.291	20.930	15.479	10.953
ZL-	214.607	200.139	199.854	218.792	200.074	199.982	212.823	200.210	200.298	24.123	18.729	13.631
ZT+	215.272	201.013	200.660	219.564	200.941	200.805	214.820	201.089	201.131	24.439	19.355	14.196
ZT-	201.666	189.397	189.532	204.010	189.397	189.586	200.969	189.474	189.875	20.957	15.255	10.695
Z+LT	209.380	195.409	194.844	213.431	195.334	195.091	207.526	195.438	195.220	22.962	18.046	13.417
Z+L+	202.700	189.053	188.728	203.183	189.001	188.939	199.853	189.067	189.048	21.437	16.253	11.933
Z+L-	214.696	200.331	199.595	218.801	200.249	199.925	213.118	200.388	200.050	24.221	19.309	14.401
Z+T+	215.410	201.243	200.322	219.627	201.124	200.677	214.282	201.239	200.815	24.514	19.853	14.876
Z+T-	203.597	189.655	189.581	203.979	189.642	189.638	201.445	189.735	189.898	21.494	16.016	11.494
Z-LT	209.375	194.823	194.963	210.063	194.786	195.095	208.024	194.881	195.409	22.634	16.296	11.460
Z-L+	200.824	188.474	188.786	203.315	188.493	188.967	197.675	188.562	189.192	20.718	14.509	10.071
Z-L-	214.624	199.817	199.730	218.851	199.747	199.884	214.092	199.859	200.216	23.872	17.722	12.639
Z-T+	215.233	200.750	200.591	219.593	200.680	200.763	214.806	200.812	201.090	24.259	18.556	13.412
Z-T-	201.744	188.976	189.347	204.093	188.995	189.549	199.664	189.057	189.794	20.665	14.100	9.649

units), effective temperature (K), and acceleration of gravity ( $\text{cm s}^{-2}$ ), central pressure, temperature, density (c.g.s. units), and hydrogen and heavy metal mass fraction respectively. Non-radial pulsation data are given in columns 14 – 25 for respective large or small  $l$  values, large frequency spacing,  $\Delta\nu$ , small spacing,  $\delta\nu$ , and the radial order averages.

Out of a possible 45 diffusion models, 44 converged, while 43 of 45 non-diffusion models converged. By “not converged” I mean that the simulation itself blew-up, and “converged” models are those that successfully evolved to the desired HR-diagram position. The models that did not converge were NDM+Z+L-, NDM+Z+T+, and DM+Z+L-. There were many attempts to obtain convergence (time step reduction, composition adjustment), but the parameters used must have been an unphysical representation for the star.

### 3.7 Pulsation Model Results

For each model of  $\epsilon$  Eridani, non-radial, adiabatic, and non-adiabatic oscillation frequencies were calculated for low values of  $l$  (0, 1, and 2) and for  $n$  averages in the ranges of  $0 \leq n \leq 10$ ,  $10 \leq n \leq 20$ , and  $20 \leq n \leq 30$ . Radial order averages are used because we do not know which range of  $n$  will be observed, so a variety of  $n$  values are calculated. Figure 3.3 shows the large frequency spacing  $\Delta\nu$  plotted against  $n$  with  $l = 0$  for all diffusion models with mass,  $M = 0.78 M_{\odot}$ . Figure 3.4 is the same but for the non-diffusion case. Values of  $n < 5$  are not shown because of the irregularity in  $\Delta\nu$  at small values of radial order. At these values the asymptotic approximation begins to break down because of *mode bumping* or *mode mixing*.

**$\epsilon$  Eridani  $0.78 M_{\odot}$  Diffusion Models. Large Spacing,  $l = 0$**

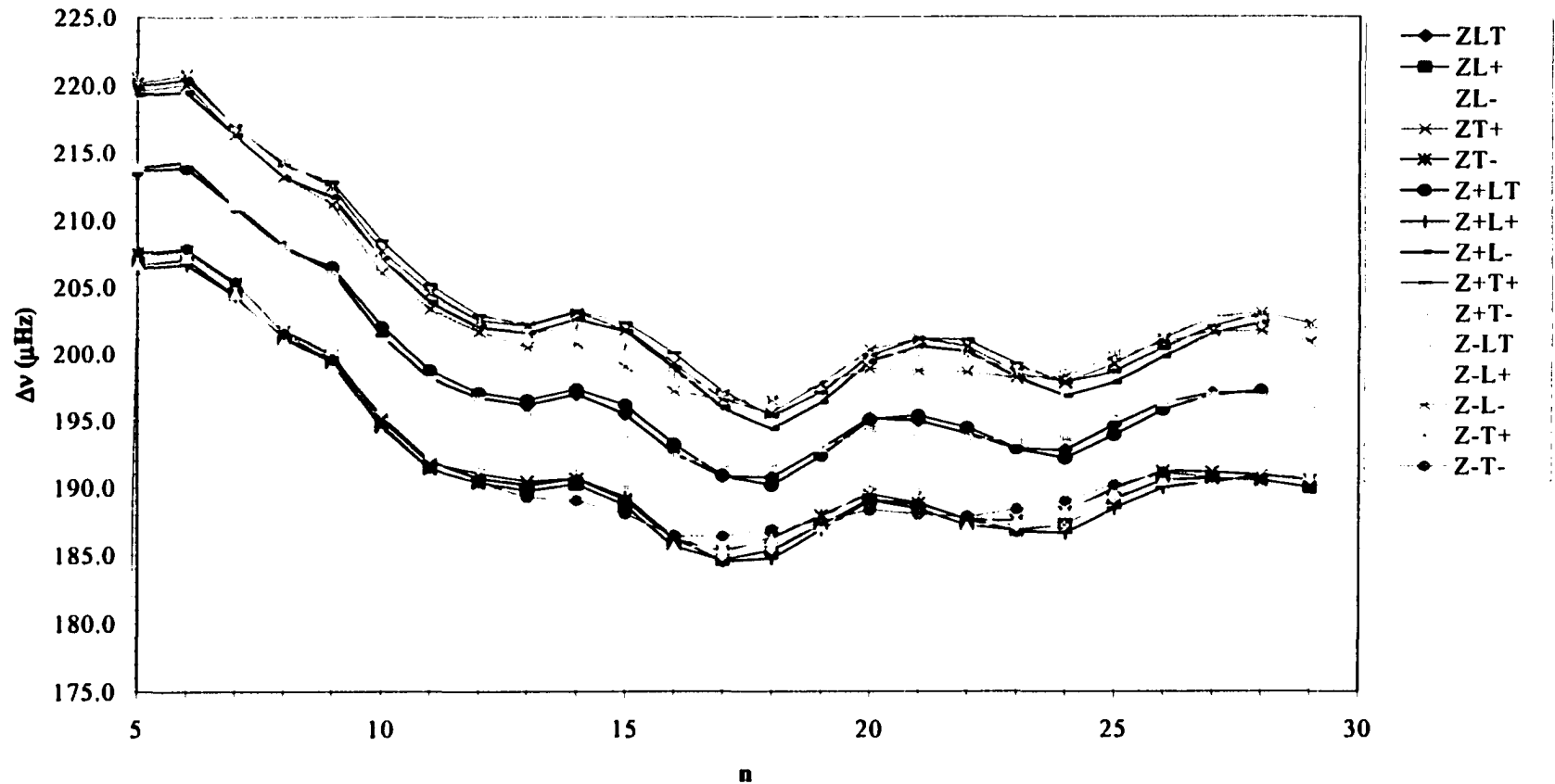


**Figure 3.3.** Large frequency spacing as a function of radial order  $n$ . Note the grouping of models. The “bands” are models of similar radii. The plot starts at  $n = 5$  since  $\Delta\nu$  is irregular for small values of the radial order. Refer to text or Table 3.7 for details of the individual models.

$\epsilon$  Eridani, Large Spacing  $l = 0$ , Non-diffusion,  $M=0.78 M_{\odot}$

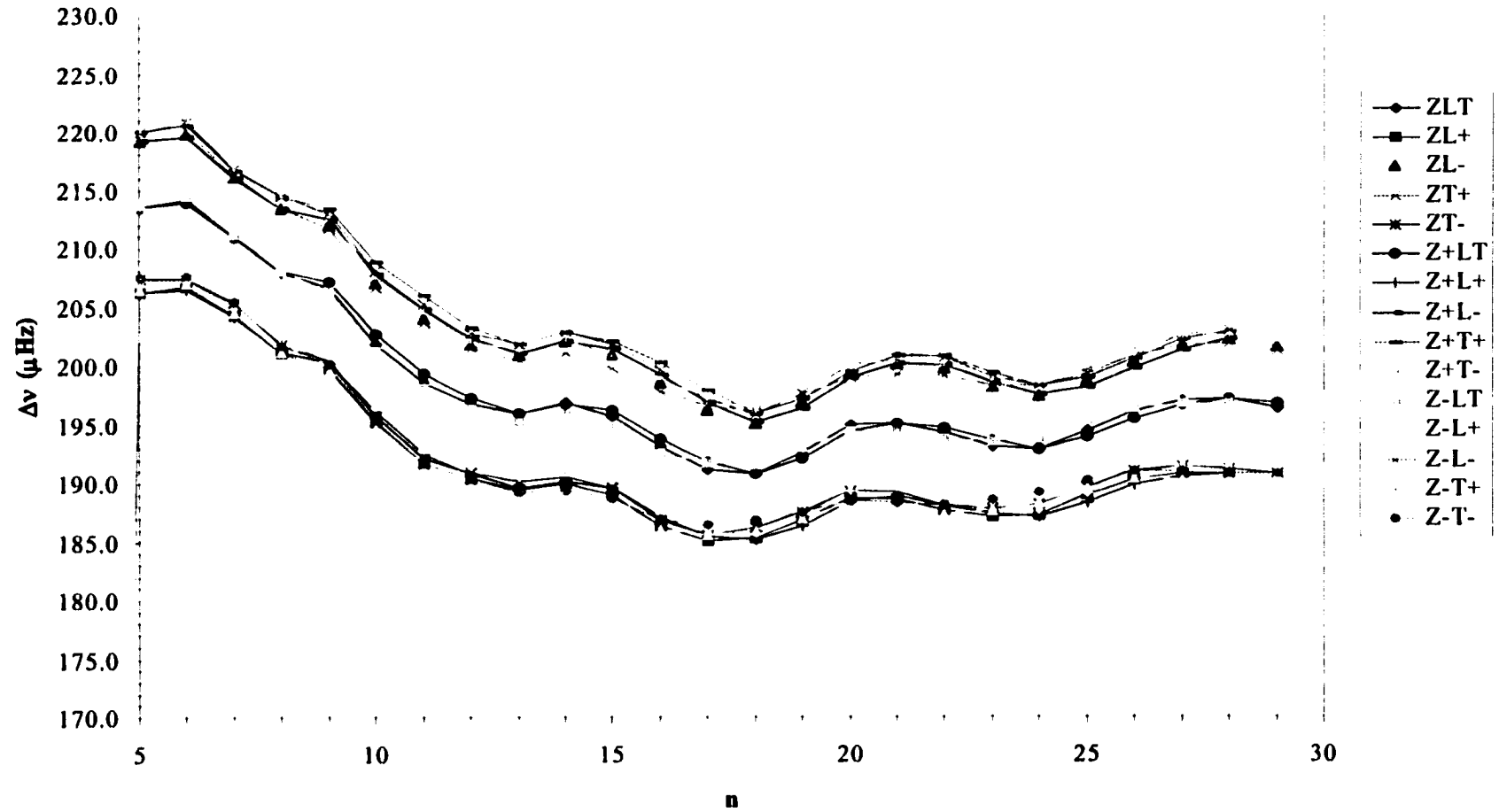


**Figure 3.4** Same as previous figure but for a models with no heavy element and helium diffusion.



The plots show a “grouping” of models with a spread about 2–3  $\mu\text{Hz}$  in width. The bands correspond to models with approximately equal radius, and occur because models were evolved to the extremes of  $\epsilon$  Eridani’s observational error box. The large spacing has a physical dependence on radius (or mass if the radius is known). The relation is shown in Figure 3.5,  $\Delta\nu$  vs.  $1/R_*$ , for the  $0.78 M_{\odot}$  diffusion models. As expected it is a very linear relation, but only for models with the same metal abundance (the models do not have the same composition). The plot indicates that changing the metal abundance of a model with a certain mass does not (greatly) change the slope, but shifts the relation slightly in the frequency spacing. Hence there is a direct (albeit weak) relationship between the composition and the large frequency spacing of a star.

The treatment of diffusion plays an important role for stellar evolution, especially in age and composition of the models. Helium or heavy elements that slowly diffuse to the core can “speed up” core evolution by increasing the mean molecular weight,  $\mu$ , and hence luminosity. However, Figures 3.3 and 3.4 show very little differences between the models with and without diffusion. That is not entirely unexpected since each model was evolved to the same position on the HR-diagram, hence the models have the same radius.

The large spacing value is more sensitive to the structure of the star (e.g. mass, radius), and it is the small spacing,  $\delta\nu$ , which is sensitive to the state of evolution of the star. Since  $\delta\nu$  varies with the gradient of the speed of sound, it is sensitive to the stellar core’s composition and age. The variation in  $\delta\nu$  with age ( $l = 0$ ) is shown for all models in Figures 3.6 (diffusion) and 3.7 (non-diffusion) for the reference mass  $0.78 M_{\odot}$ . The three values of  $\delta\nu$  for each age come from the groupings of the radial order averages,

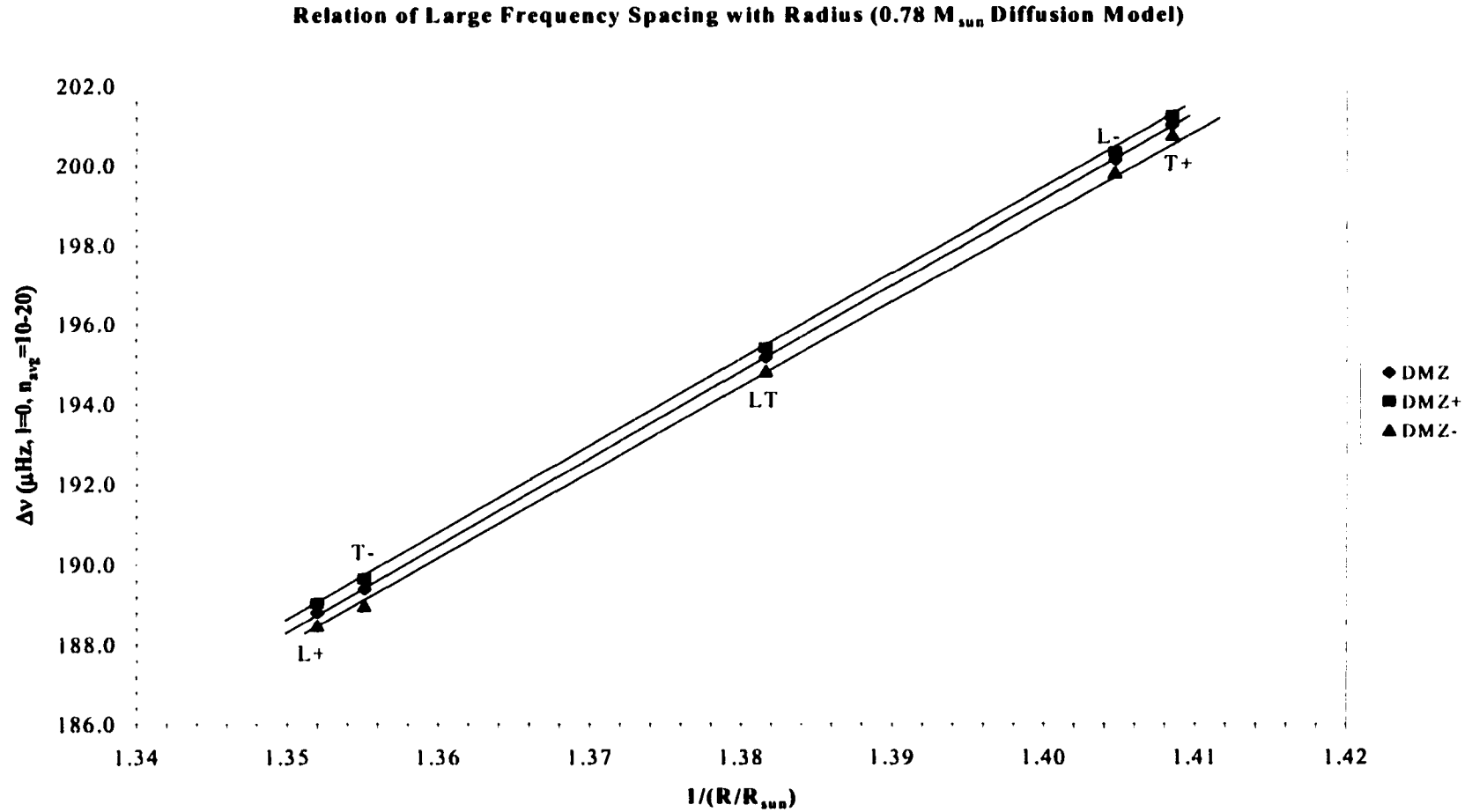


**Figure 3.5.** Plot showing the relationship between the large frequency spacing and stellar radius for selected  $\epsilon$  Eridani models. The lines correspond to models of equal metal abundance, and each group of three is the position on the HR-diagram to which the models were evolved.

$n_{avg}$ , and each average represents a model. Labels identifying the models are indicated with one label at each age, and the label applies to all models at that age.

The dependence of the small spacing with age is evident from Figures 3.6 and 3.7. The best-fit line (linear regression) is shown for each  $n_{avg}$ , and it fits the data very well. The results of the regressions made for all the  $\epsilon$  Eridani models are shown in Table 3.8. The last column in Table 3.8 is the correlation coefficient,  $R$ , of the linear regression. A value of  $R = 1$  ( $0 \leq R \leq 1$ ) represents a perfect result. Note the decrease in uncertainty with increasing  $n_{avg}$  values because of no or little mode bumping.

With that information it may be possible to reduce the uncertainty in  $\epsilon$  Eridani's age when the MOST or MONS missions have observed a small frequency spacing. It is possible, though, that the observed small frequency spacing will be different than the values suggested by the models that were calculated for  $\epsilon$  Eridani. It is not unexpected that the observations will yield frequency spacings outside of the range defined by the simulations. The uncertainty analysis will allow for the retrieval of stellar information for  $\epsilon$  Eridani, and the observations can be used to refine the stellar and pulsation models.

The difference between simulations with and without diffusion may be slight, but they are evident. Diffusion models have a different stellar core composition because heavy elements (Y & Z) settle to the centre. The process slightly accelerates stellar evolution since diffusion models take less time evolving to the same position on the HR-diagram. That possibly accounts for the different values of the linear regressions, and for the higher uncertainty in the low radial order averages.

The higher uncertainty (spread of data points about the regression line) indicates that at a low radial order the small frequency spacing is more sensitive to the stellar

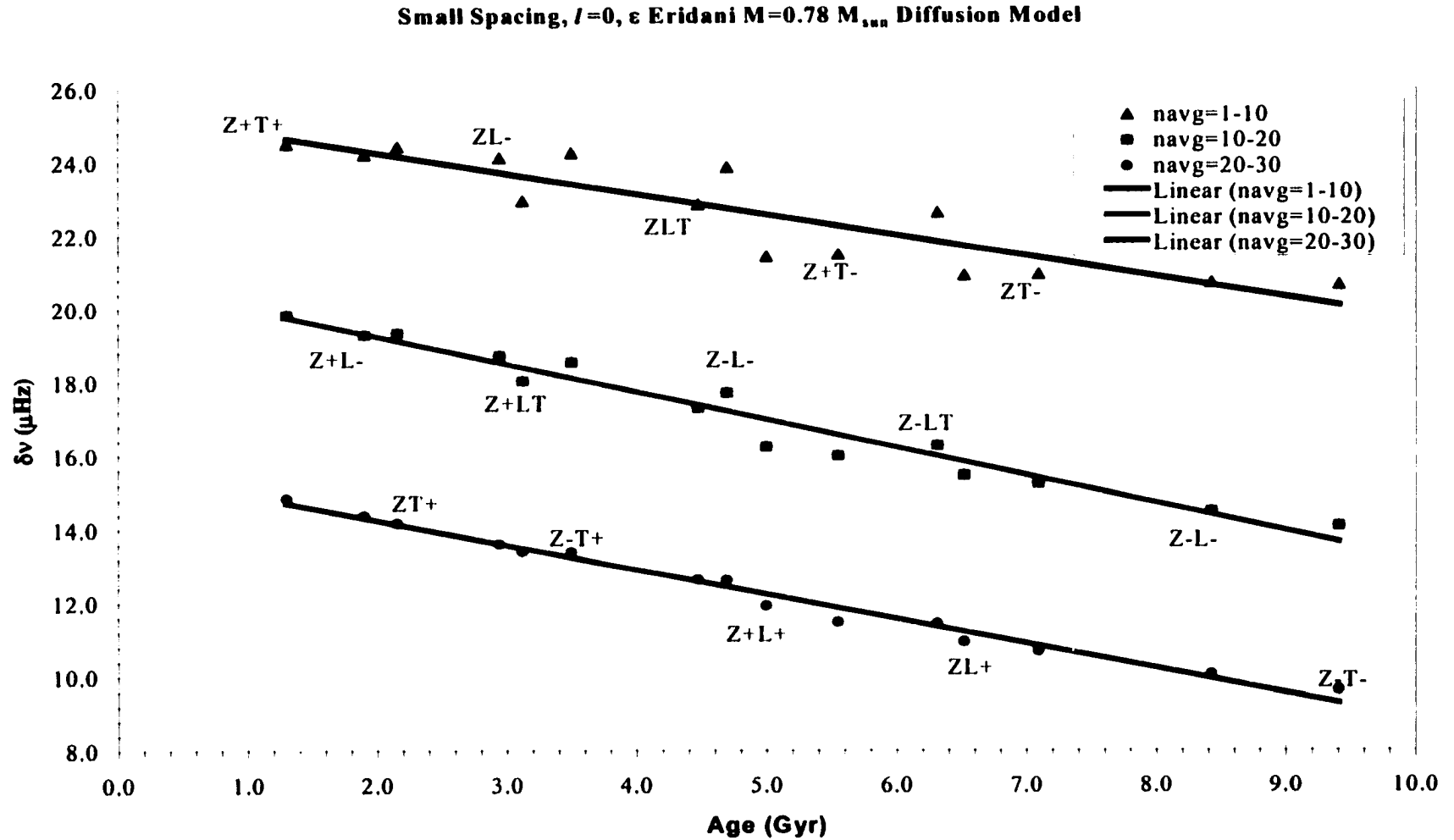


**Figure 3.6.** Relation of the small spacing,  $\delta\nu$ , with age. The letters by the data points are the diffusion model reference. Refer to Table 3.8 for a summary of the regression results. Note the scatter decreases with increasing radial order,  $n$ .

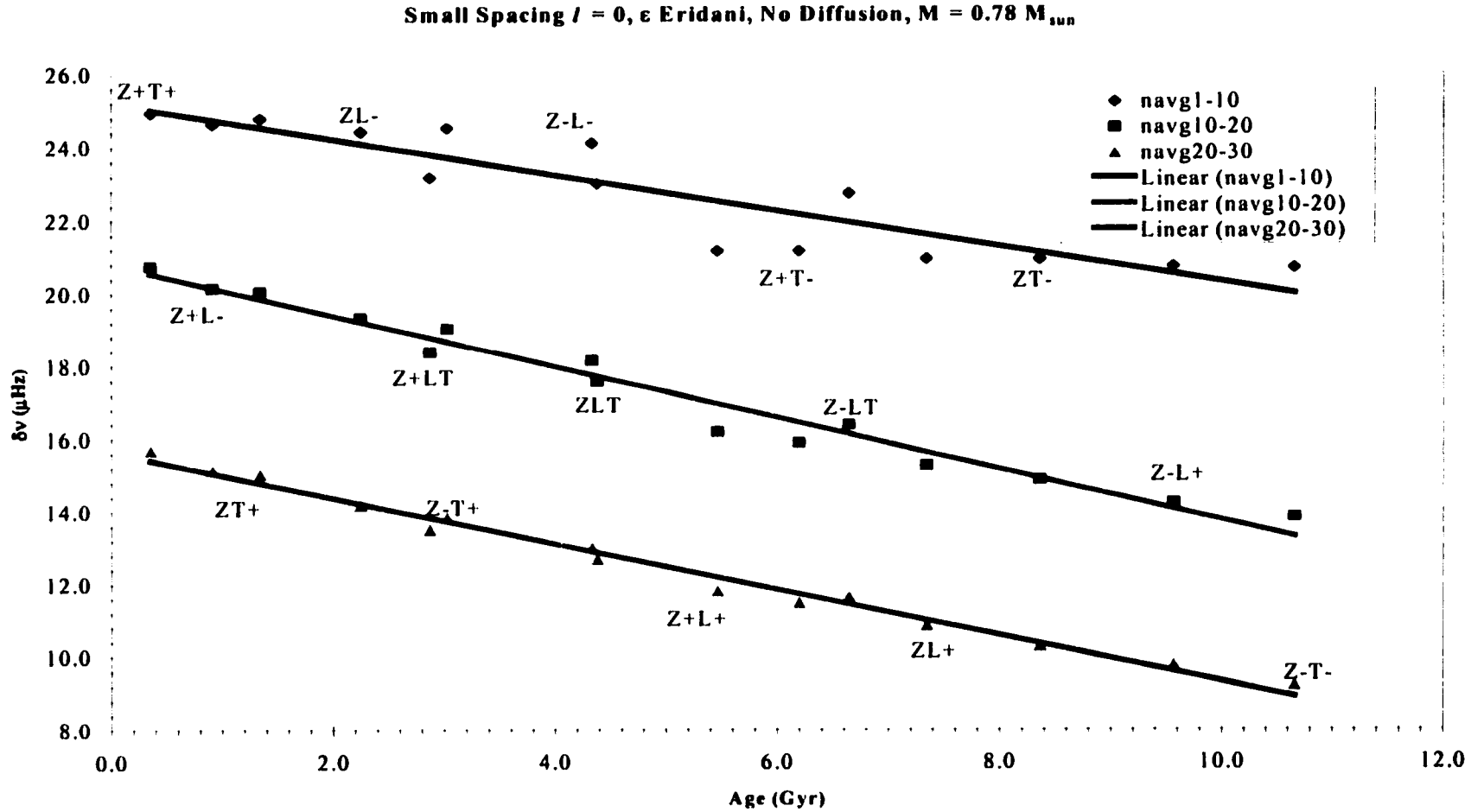


**Figure 3.7.** Same as Figure 3.6, but for non-diffusion models. A similar decrease in scatter with increasing radial order is seen for all models.

**Table 3.8** Linear regression results of  $\delta v$  variations with age for all models. The last column,  $R$ , is the correlation coefficient. The fifth column is the percent uncertainty of the slope value.

Mass	Diffusion	n(avg)	slope	% unc.	R
0.76 $M_{\text{sun}}$	yes	n(1-10)	-0.51874	16.22%	0.8632
	no	n(1-10)	-0.46053	12.29%	0.9143
	yes	n(10-20)	-0.70613	6.11%	0.9766
	no	n(10-20)	-0.64426	5.03%	0.9840
	yes	n(20-30)	-0.65268	3.90%	0.9903
	no	n(20-30)	-0.59873	3.12%	0.9937
0.78 $M_{\text{sun}}$	yes	n(1-10)	-0.560169	13.84%	0.8948
	no	n(1-10)	-0.4865502	12.43%	0.9125
	yes	n(10-20)	-0.75216	5.73%	0.9793
	no	n(10-20)	-0.701705	4.66%	0.9862
	yes	n(20-30)	-0.6690801	3.55%	0.9919
	no	n(20-30)	-0.6328053	3.12%	0.9937
0.80 $M_{\text{sun}}$	yes	n(1-10)	-0.6849217	15.32%	0.8830
	no	n(1-10)	-0.7128941	17.73%	0.8620
	yes	n(10-20)	-0.7862474	6.35%	0.9766
	no	n(10-20)	-0.77104101	6.49%	0.9776
	yes	n(20-30)	-0.686071	4.90%	0.9859
	no	n(20-30)	-0.661617	4.70%	0.9881

parameters and conditions in the core. The modes of low radial order are near the core, so the small spacing associated with such modes suffer from the effects of mode mixing.

The reason mode mixing occurs for low frequency  $p$ -modes is because the modes propagate to a deeper depth where the centrally trapped  $g$ -modes exist. For  $\epsilon$  Eridani that is shown in Figure 3.8, a propagation diagram. The Lamb frequency for an  $l = 1$  mode is also shown in Figure 3.8. The Brunt-Väisälä frequency does not have a high frequency peak, like the more evolved stars, which is why only the lower frequency  $p$ -modes are affected by any mode mixing. The most interesting feature of Figure 3.8 is the behavior of  $N$  near the outer envelope, since it drops to zero at the base of the convection zone, around  $0.7 r/R_*$ , and is erratic and goes to infinity at the surface.

Figure 3.9 is an example of one of  $\epsilon$  Eridani's many eigenfunctions. This depicts the radial displacement of an  $l = 0$ ,  $n = 9$ , and  $\nu = 3184.72 \mu\text{Hz}$  pure  $p$ -mode. The amplitude decreases with depth, and the turning point is around  $0.7 r/R_*$ , coincidentally near the base of the convection zone. The  $p$ -modes are trapped more effectively in the envelope with increasing  $l$  since the width of the evanescent zone increases (Unno *et al.* 1989).

### Brunt-Vaisala and Lamb Frequencies

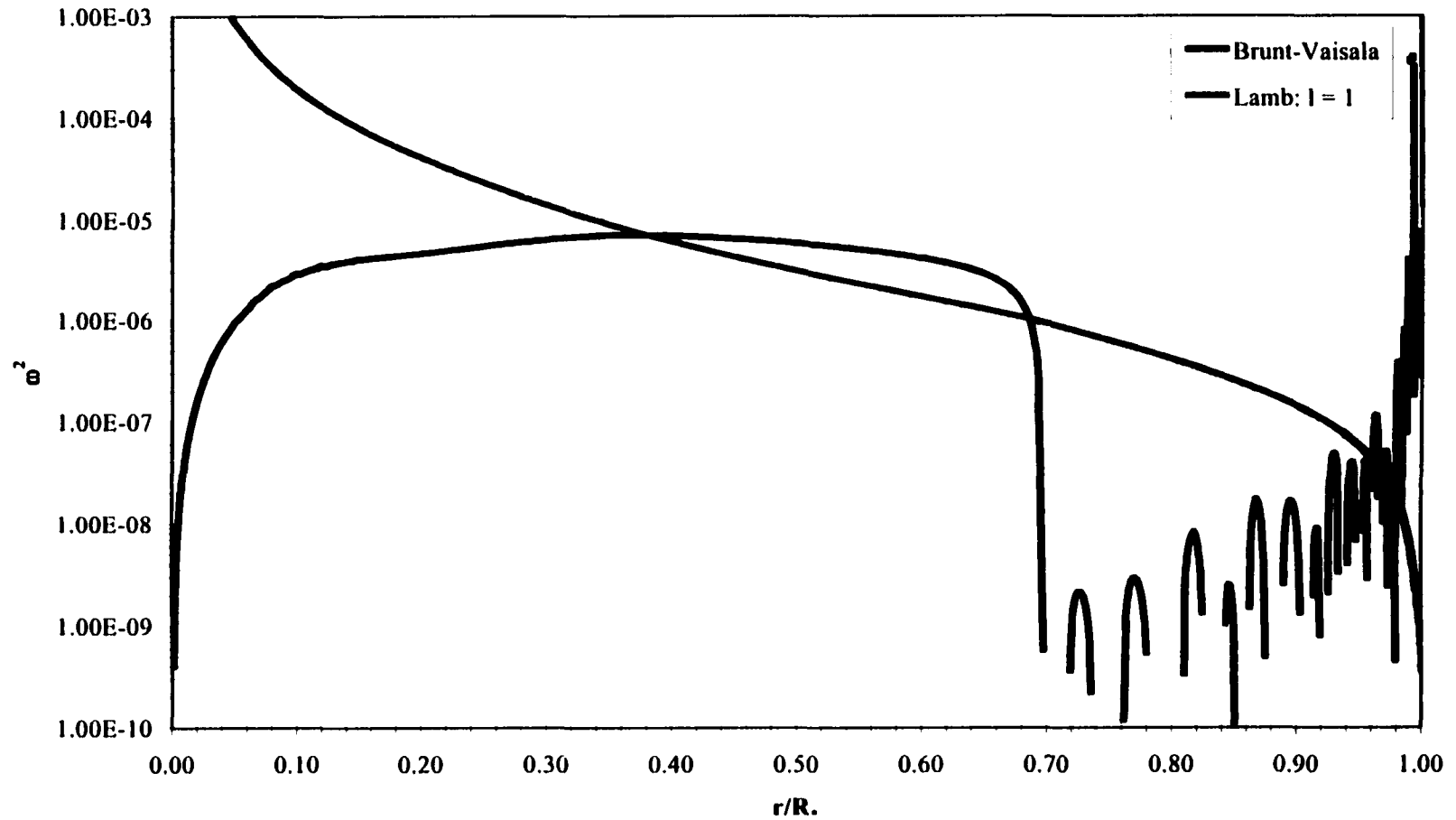


**Figure 3.8** Propagation diagram for the central model. This defines the regions of mode propagation. Mode mixing is less of a factor for a main-sequence star because of the relatively low Brunt-Väisälä frequency.



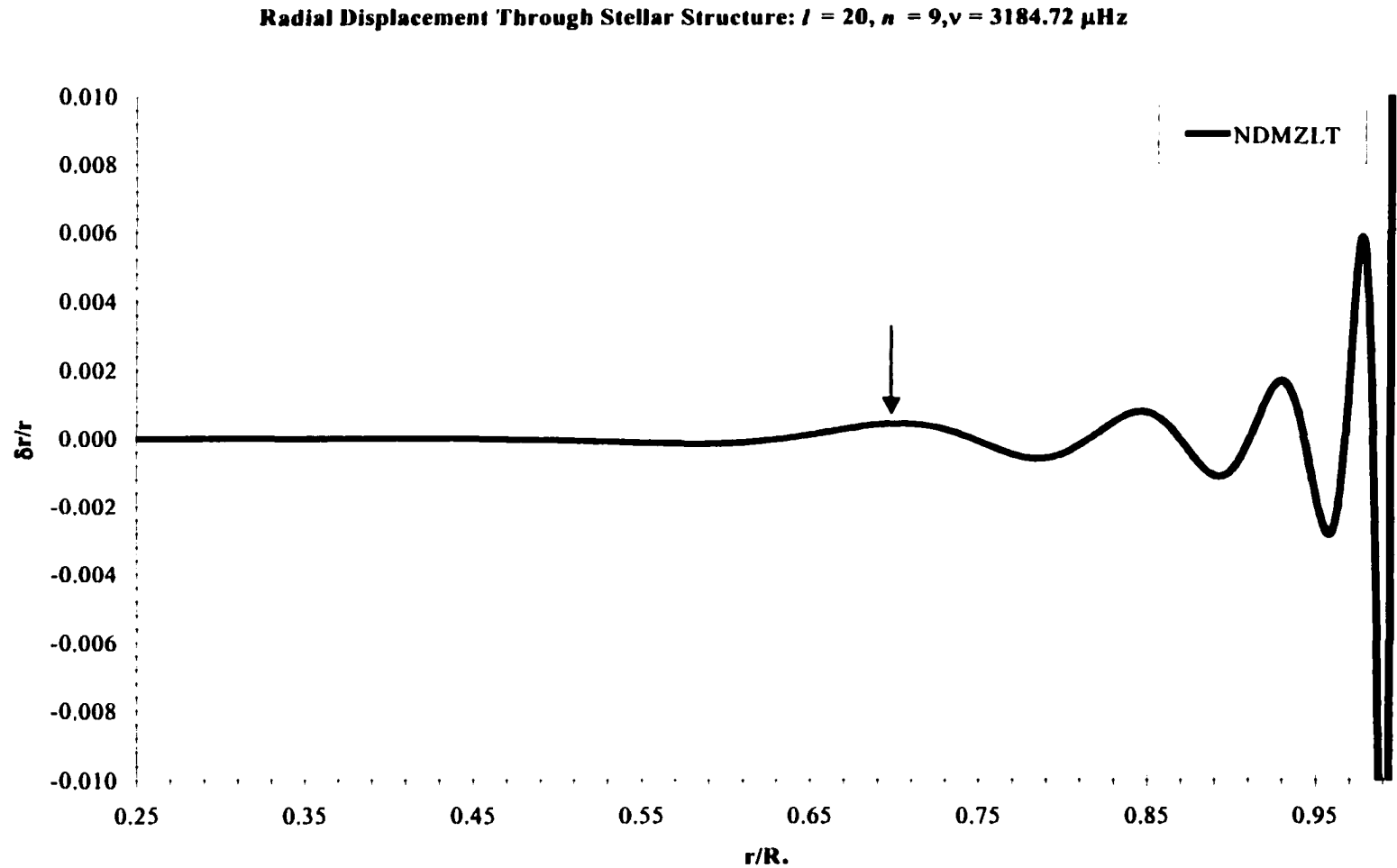


**Figure 3.9** Eigenfunction for an  $l = 20$  mode. This particular mode has a turning point near the edge of the convection zone. The mode is excited in the extreme outer layers of the star, and its amplitude decreases quickly with depth.

# Chapter 4

## $\beta$ Hydri

### 4. Introduction

$\beta$  Hydri is often referred to as the future Sun (Dravins *et al.* 1993a, b, c) because it is also of spectral type G2 but of luminosity class IV, a subgiant. Its proximity to our solar system (a distance of about 7.5 pc) makes it the closest subgiant and a prime laboratory for post-main-sequence evolution research.

The work of Dravins *et al.* (1993a, b, c) focused primarily on the (possible) future of solar activity. The three papers discussed  $\beta$  Hydri's evolution, lithium abundance, and photospheric structure (1993a); chromospheric activity and variability (1993b); transition region, corona, and stellar wind (1993c). Understanding stars like  $\beta$  Hydri enables us to better understand our own Sun and its physical properties.

This chapter will follow a similar format to chapter 3 discussing  $\epsilon$  Eridani. The most significant difference between the two stars is their state of evolution,  $\beta$  Hydri being the more evolved star. That allows for a detailed analysis of the pulsation spectrum for an evolved star, and a comparison with results for a younger (less evolved) star.

### 4.1 Magnitude, Colours, and Parallax

Since  $\beta$  Hydri is a bright, nearby star, it has been subject to much observation (Dravins *et al.* 1993a, b, c; Frandsen 1987; Dravins, Lindegren, and VandenBerg 1998;

and Bedding *et al.* 2001). All of the above authors use an apparent visual magnitude consistent with the Hipparcos catalogue value of  $2.82 \pm 0.02$ . I adopt the same value. It should be noted that the Hipparcos catalogue does not quote an uncertainty; I chose  $\pm 0.02$  since it takes into account  $m_v = 2.80$  mag used by the above authors and for any systematic errors.

The Hipparcos catalogue value was used for the colour index:  $B-V = 0.618 \pm 0.008$ . That value is the Hipparcos result tied to the UBV photometry system.

The General Catalogue of Trigonometric Stellar Parallaxes gives  $\beta$  Hydri's parallax as  $\pi = 153 \pm 7$  mas (Jenkins 1952). The value was updated, with the incorporation of new observations, to  $150.1 \pm 7.2$  (van Altena *et al.* 1995; approximately 20-25 observations over the past 70 years; van Altena private communication). The ground-based determinations stood alone until the space-based Hipparcos mission obtained a smaller and more precise parallax of  $\pi = 133.78 \pm 0.51$  mas. That is the value I used for all the observational parameter calculations.

## 4.2 Effective Temperature, Surface Gravity, and Metallicity

Estimates for  $\beta$  Hydri's effective temperature are very consistent in the literature. I used the value from Dravins *et al.* (1993a), who adopt  $T_{\text{eff}} = 5800 \pm 100$  K. Their value is based on effective temperatures of 5730,  $5880 \pm 100$ , 5860, and 5250 K derived by Hearnshaw (1972), Gehren (1981), Proust & Foy (1988), and Gratton & Ortolani (1986), respectively. Interestingly, the adopted value is equal to the solar effective temperature of  $T_{\text{eff}} = 5779 \pm 20$  K (Guenther and Demarque 2000) to within uncertainty.

The surface gravity, only important in determining the bolometric correction, was taken to be  $\log g \sim 4$  (solar value is 4.44). Some other  $\log g$  determinations are as follows: a grid of model atmospheres in conjunction with spectroscopic analysis produced values of 3.75 (Gratton & Ortolani 1986), 4.0 (Proust & Foy 1988), and 3.8 (Hearnshaw 1972). Gehren (1981), using parallax and photometry, obtained 4.15. Dravins *et al.* (1993a) simply adopt 3.84, a factor of four less than the solar value. Allende Prieto & Lambert (1999) obtained  $3.99 \pm 0.14$  by applying a transformation from the theoretical,  $\log g - T_{\text{eff}}$  plane to the observational  $M_v - (B-V)$  plane using the model isochrones of Bertelli *et al.* (1994).

Metallicity determinations in the literature do not agree as well as those for effective temperature, but what is in agreement is that  $\beta$  Hydri is metal deficient when compared to the Sun. That is consistent with  $\beta$  Hydri's age and evolutionary status, having formed earlier when the heavy metal resources were less abundant in the galactic disk.

Dravins *et al.* (1993a) adopted  $[\text{Fe}/\text{H}] = -0.20$  from the results of Rodgers & Bell (1963), Hearnshaw (1972), Gehren (1981), Rebolo *et al.* (1986), and Proust & Foy (1988), who all derived metallicity values in the range  $0.0 \leq [\text{Fe}/\text{H}] \leq -0.30$ .

In a more recent paper, Dravins, Lindegren, and Vandenberg (1998) explored the metallicity values in more detail by expanding their models to cover a metallicity range of  $-0.10 \leq [\text{Fe}/\text{H}] \leq -0.28$ . Their models fit  $\beta$  Hydri's position on the observational ( $M_v - T_{\text{eff}}$ ) HR-diagram within the star's observational uncertainty box. Based mainly on their work, I adopted  $[\text{Fe}/\text{H}] = -0.20 \pm 0.10$ , which implies  $Z/X = 0.015 \pm 0.006$ .

### 4.3 Bolometric Correction and Luminosity

As done with  $\epsilon$  Eridani, the bolometric correction was obtained through a linear interpolation of the Green *et al.* (1987) colour tables. The required input parameters are listed in Table 4.1.

**Table 4.1.** Required parameters for bolometric correction determination.

Colour Table Interpolation Values	
B-V.....	$0.618 \pm 0.008$
$T_{\text{eff}}$ .....	$5800 \pm 100 \text{ K}$
[Fe/H].....	$-0.20 \pm 0.10$

The results are summarized in Table 4.2. The large uncertainty associated with the bolometric correction (B.C. =  $-0.024 \pm 0.030$ ) results largely from the uncertainty in effective temperature. That value is  $\pm 0.026$ , and uncertainties from the colour index, B-V, and the metallicity, [Fe/H] contribute  $\pm 0.009$ , and  $\pm 0.012$ , respectively.

**Table 4.2.** Parameters calculated with the derived bolometric correction.

Results of Bolometric Correction Determination for $\beta$ Hydri	
$M_v$ .....	$3.45 \pm 0.022$
B.C.....	$-0.024 \pm 0.030$
$M_{\text{bol}}$ .....	$3.43 \pm 0.037$
$\text{Log } (L/L_{\odot})$ .....	$0.545 \pm 0.015$
$R/R_{\odot}$ .....	$1.86 \pm 0.072$

### 4.4 Mass and Age

There does not exist much ambiguity about  $\beta$  Hydri's mass. Being a subgiant,  $\beta$  Hydri's position on the HR-Diagram is such that the evolutionary models run nearly horizontal (see Figure 4.3 in § 4.6). The implication is that only a small number of models will evolve within the range of  $\beta$  Hydri's observational parameters making its

age and mass among the most precisely determined for a single star, i.e. not in a binary system (Dravins, Lindengren, and VandenBerg 1998).

The first detailed mass and age estimate for  $\beta$  Hydri was done by Dravins *et al.* (1993a). They computed many stellar evolutionary tracks using the stellar structure code described by VandenBerg (1983) and VandenBerg & Bell (1985). Interpolation between the stellar model tracks with  $M = 1.0 M_{\odot}$ ,  $[\text{Fe}/\text{H}] = -0.23$ ; and  $M = 0.90 M_{\odot}$ ,  $[\text{Fe}/\text{H}] = -0.23$ ; they derive a mass and age of  $M = 0.99 M_{\odot}$  and 9.5 Gyr, respectively.

The position of  $\beta$  Hydri on the HR-diagram used by Dravins *et al.* (1993a) was determined assuming a parallax  $\pi = 153 \pm 7$  mas (Jenkins 1952). As mentioned in section 4.1, that value is larger and less precise than the space-based determination of  $133.78 \pm 0.51$  mas by the Hipparcos mission.

The  $\sim 12.5\%$  decrease in parallax and the effect of precise data have a significant effect on the observational characteristics of  $\beta$  Hydri. The difference in stellar parameters resulting from such a change (recall  $m_v$  is constant) is summarized in Table 4.3. The most important implication is the 82.5% increase in luminosity, which effects  $\beta$  Hydri's position on the theoretical HR-diagram. Figure 4.1 shows the difference in stellar evolution resulting simply from two very different parallax determinations. Both models start with the same parameters at the ZAMS, and are calibrated to produce  $\beta$  Hydri's respective luminosity.

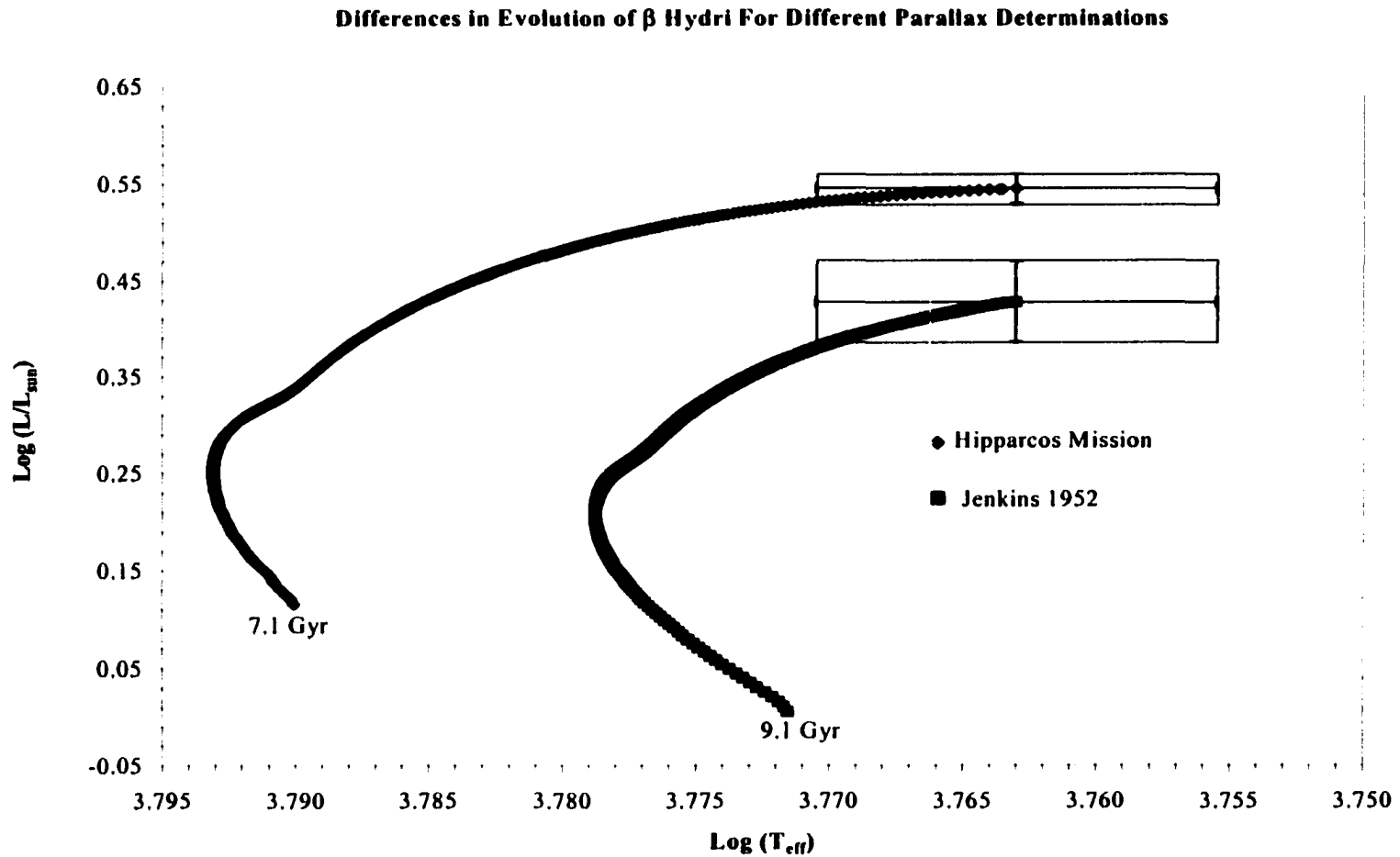


**Figure 4.1.** Differences in evolution as a result of the newly available parallax. The diffusion models were evolved and calibrated with YREC. Both models began their simulation with the same parameters ( $M = 1.10 M_{\odot}$ ,  $Z = 0.011$ ,  $\alpha = 1.73141$ ).

**Table 4.3.** Difference in stellar parameters resulting from the changes in parallax. The ages in this table were determined from YREC and not the Dravins *et al.* (1993) paper.

Parameters	Jenkins (1952)	Hipparcos
	$\pi = 153 \pm 7 \text{ mas}$	$\pi = 133.78 \pm 0.51$
Distance.....	$6.54 \pm 0.30 \text{ pc}$	$7.48 \pm 0.03 \text{ pc}$
$M_v$ .....	$3.74 \pm 0.10 \text{ mag}$	$3.45 \pm 0.02 \text{ mag}$
$L/L_\odot$ .....	$2.68 \pm 0.26$	$3.50 \pm 0.11$
Age .....	$\sim 9.1 \text{ Gyr}$	$\sim 7.10 \text{ Gyr}$

Realizing the significance of the new Hipparcos parallax, Dravins, Lindegren, and VandenBerg (1998) computed a new set of stellar evolutionary models for the star. Not only was  $\beta$  Hydri's position in the HR-plane pinpointed more precisely, but the stellar structure code (used in Dravins *et al.* 1993a) was upgraded as well. Some of the improvements included updated OPAL opacities (Rogers & Iglesias 1992), low-temperature opacities (Alexander & Ferguson 1994), the same nuclear reaction rates as in standard solar models (Bachall & Pinsonneault 1992, Guenther *et al.* 1992a), and an equation-of-state with Coulomb corrections and other non-ideal effects (VandenBerg *et al.* 2000; that paper was in preparation at the time Dravins *et al.* used its information).

Table 4.4 lists the results obtained by Dravins *et al.* (1998) when interpolating between the tracks using the new parallax. The last model in the table is their best-fit results. It is that model ( $M = 1.10 M_\odot$ ,  $Y = 0.270$ ,  $Z = 0.011$ , Age  $\sim 6.7 \text{ Gyr}$ ) upon which I based my choice of mass,  $M = 1.10 M_\odot$ . I chose an uncertainty of  $\pm 0.15 M_\odot$  ( $\sim 14\%$ ) to account for the mass range in Table 4.4.

The age inferred for  $\beta$  Hydri is thus reduced by about 3 Gyr from its previous estimate of 9.5 Gyr by Dravins *et al.* (1993a). Unlike  $\epsilon$  Eridani, there is little or no evidence supporting an age other than that determined by the aforementioned authors. In



section 4.6 I will discuss the age ranges determined in this work, and compare them to that of the age determined by the authors mentioned here.

**Table 4.4.** Information adapted from Dravins *et al.* (1998). The last model is their best fit. They determined the ages by interpolating between their tracks.

Z	Y	[Me/H]	Mass ( $M_{\odot}$ )	Age (Gyr)
0.0100	0.2716	-0.28	1.053	6.83
0.0125	0.2716	-0.20	1.095	6.52
0.0150	0.2716	-0.10	1.228	6.31
0.0125	0.2616	-0.20	1.109	6.64
0.0110	0.0270	-0.20	1.100	6.70

## 4.5 Previous Seismology

The quest for a positive identification of stellar non-radial oscillations has not been simple or straightforward. Observations are prone to large errors induced by inadequate equipment, interrupted viewing, and the Earth's atmosphere. The earliest search for solar-like oscillations on  $\beta$  Hydri suffered from the aforementioned setbacks. Frandsen (1987) adopted a method used by Andersen (1984) on the Sun. The method was based on the fact that the intensity changes resulting from temperature fluctuations are larger in the line cores than in the continuum. Unfortunately, their expected noise levels were not achieved, and Frandsen (1987) proclaimed that there was not much hope for any  $p$ -mode detection. Their power spectrum for the longest (11-hour) observation suffered from slow instrumental drifts. The work of Frandsen (1987) did result in an upper limit of  $\delta L/L \sim 5 \times 10^{-5}$  on intensity oscillations in the 5-minute range, and concluded that the instrumental set-up must be changed for accurate data retrieval.

Edmonds and Cram (1995) made a more rigorous attempt by generating a spectrum from CCD data. Their observations were still hampered with interruptions

during viewing (shorted by cloud). They clearly state that no conclusions of interest for theoretical studies can be made. Similarly to Frandsen (1987), Edmonds and Cram (1995) did obtain a new upper limit in the oscillations of about  $1 - 1.5 \text{ m/s}$  ( $\delta L/L \sim 2.2 \times 10^{-5}$ ), lower than the Frandsen (1987) limit.

Concrete evidence of solar-like oscillations did not emerge until recently from the work of Bedding *et al.* (2001, hereafter Bedding2001). Using the University College London Echelle Spectrograph (UCLES) at the coudé focus 3.9m Anglo Australian Telescope (AAT), Bedding2001 obtained a power spectrum for  $\beta$  Hydri. It is shown in Figure 4.2. The dashed lines represent the frequency spacings Bedding2001 found to best-fit the data, and the dotted lines are the  $\pm 1 \text{ day}^{-1}$  aliases.

From the property that low-degree oscillations are well approximated by the asymptotic relation (note that this is the formula Bedding2001 used in their analysis and is a version of the asymptotic equation 2.25),

$$\nu(n', l) = \nu_0 + \Delta\nu(n' + 1/2l) - l(l+1)D_0 \quad (4.01)$$

where  $D_0 = \delta\nu_0/6$ . Bedding2001 used a comb analysis to calculate a response function for all sensible values of  $\Delta\nu$ ,  $\delta\nu_0$ , and  $\nu_0$ . The asymptotic relation is written in the form of equation 4.01 because they searched for mode structure in the region of excess power. The quantity  $\nu_0$  is the frequency of a radial ( $l = 0$ ) mode within the region of maximum power for which  $n' = 0$ , and it replaces the  $1/4 + \alpha$  terms from equation 2.14 (§ 2.3).

Their search ranged over the values  $\Delta\nu = 45 - 80 \text{ } \mu\text{Hz}$  and  $D_0 = 0.5 - 2.0 \text{ } \mu\text{Hz}$ . They found two triplets of  $(\Delta\nu, D_0, \nu_0)$  that gave the best responses, which are referred to as solution A (56.2, 0.83, 1031.1)  $\mu\text{Hz}$  and solution B (60.3, 0.75, 1005.3)  $\mu\text{Hz}$ . The

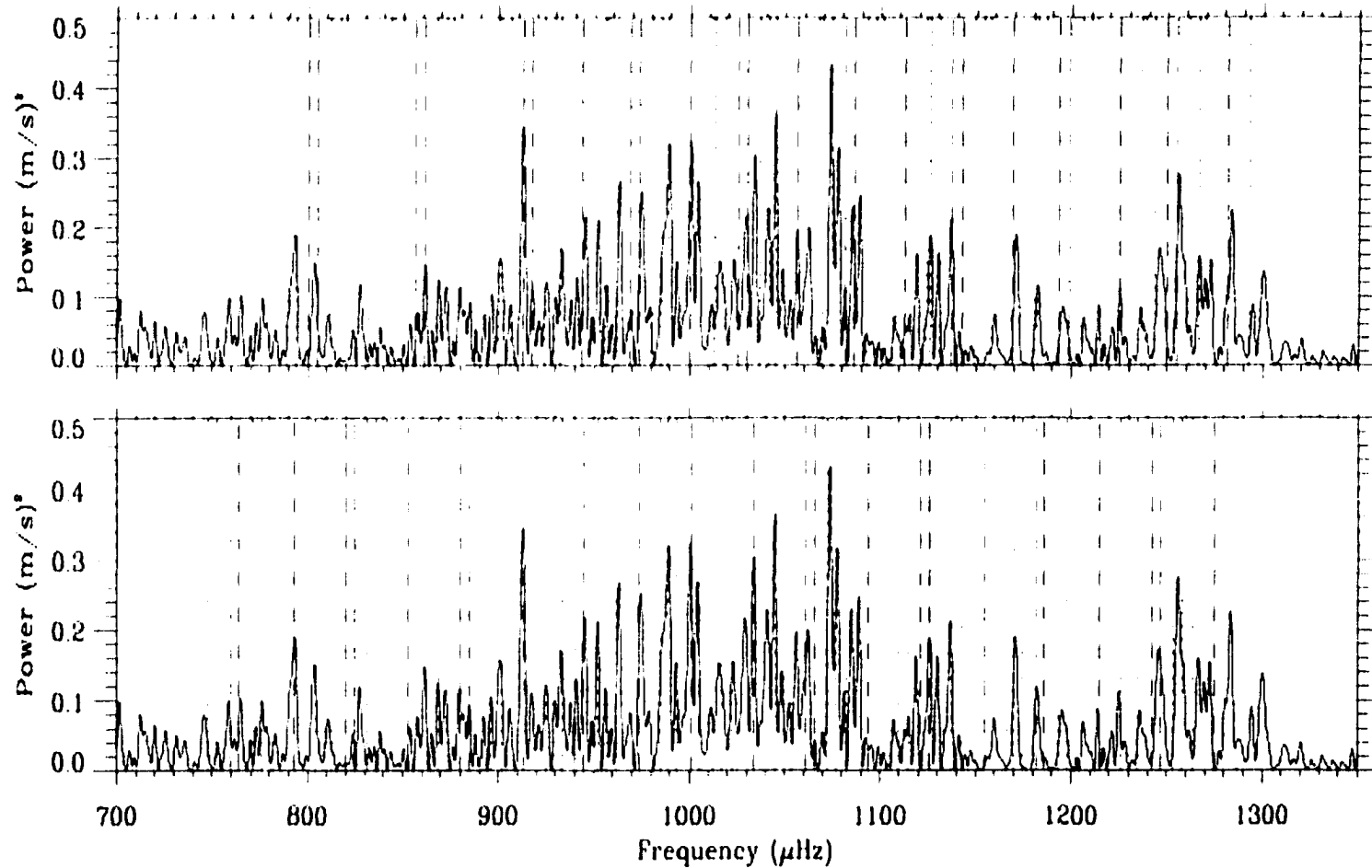


**Figure 4.2.** Power spectrum of oscillations obtained for  $\beta$  Hydri. The dashed lines correspond to the frequencies given by equation 4.01 for the two solutions, A & B (upper and lower panel respectively) determined by Bedding2001. The dotted lines represent the  $\pm 1 \text{ day}^{-1}$  aliases. Refer to text.

frequencies corresponding to those solutions are overlaid on the power spectrum in Figure 4.2.

Bedding2001 note that solution B only represents the low frequencies, while the frequencies for solution A cover the entire range of excess power and are in very good agreement with predictions of  $\Delta\nu = 56.0 \mu\text{Hz}$  (for the latest mass estimate; KB95). They suggest that solution A is the correct one. An interesting feature encountered by Bedding2001 is that the oscillation frequencies in  $\beta$  Hydri have significant departures from the asymptotic relation, and that inhibits the extraction of the correct frequencies from their single-site data.

The analysis done for this work is also encouraging since I obtained large frequency spacing values on the same order as Bedding2001. The results are discussed in more detail in the following sections.

## 4.6 Stellar Evolution Models

The production of stellar models was performed in the same manner as for  $\epsilon$  Eridani. The model parameters are summarized in Table 4.5, and the first 5 models are presented in Figure 4.3. Note how the models are almost parallel for the subgiant star, and the small variation in the end ages.

**Table 4.5.** Stellar evolution parameters for  $\beta$  Hydri.  $T_{\text{eff}}$  is in K.

Parameter	Value
Mass ( $M_{\odot}$ ).....	$1.10 \pm 0.15$
Z.....	$0.011 \pm 0.004$
$\log L/L_{\odot}$ .....	$0.545 \pm 0.015$
$\log T_{\text{eff}}$ .....	$3.763 \pm 0.0075$

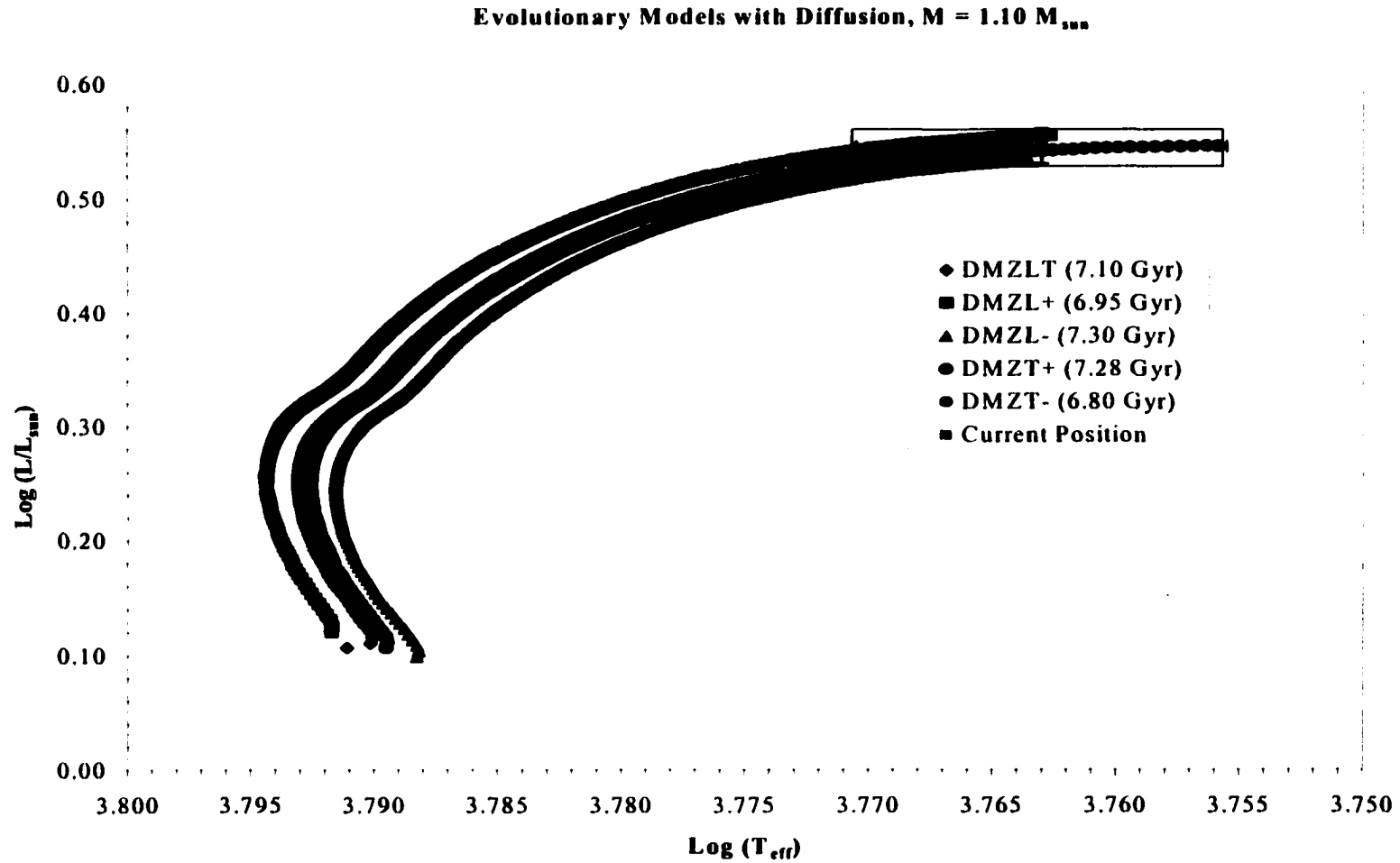


**Figure 4.3.** Stellar evolution diffusion models for  $\beta$  Hydri. Note how the unique position of the star on the subgiant branch limits the range or spread in the parameter space, e.g. the end ages and composition do not vary greatly. Quite unlike the main sequence star  $\epsilon$  Eridani.

The metal abundance,  $Z = 0.011 \pm 0.004$ , was taken from the work of Dravins *et al.* (1998), and the uncertainty was chosen to cover the range of values determined by the above authors. It should be noted that the value is the same as that derived through solving the following equations:

$$\frac{Z_{\star}}{X_{\star}} = (\text{Fe}/\text{H})_{\odot} \times 10^{[\text{Fe}/\text{H}]} \quad (4.02)$$

$$X_{\star} + Y_{\star} + Z_{\star} = 1 \quad (4.03)$$

$$\frac{Y_{\star} - Y_{\text{p}}}{Z_{\star}} = G_{\text{p}} \quad (4.04)$$

where  $G_{\text{p}}$  is the galactic enrichment parameter equal to about 2.50 (Bressan *et al.* 1994), and  $Y_{\text{p}}$  is the primordial abundance of helium taken to be  $0.235 \pm 0.005$  (Olive and Steigman 1995). Solving the above system gives an approximate value for the star's chemical composition. When it is applied to  $\beta$  Hydri, I obtain  $Z = 0.011 \pm 0.004$  (another reason why I chose the uncertainty of  $\pm 0.004$ ). The uncertainties were propagated in the usual way. The galactic enrichment parameter is an observationally determined quantity, and can be found to vary significantly from star to star. However,  $Z$  is not very sensitive to this value so it does not vary greatly with the choice of  $G_{\text{p}}$ .

There were no problems evolving all ninety (90) models, and the data for the fifteen (15) diffusion models covering the mass,  $M = 1.10 M_{\odot}$ , are tabulated in Table 4.6. The information shown is the same as for  $\epsilon$  Eridani, except that  $Y_{\text{c}}$ , the central helium mass fraction, is shown since  $X_{\text{c}}$  is essentially zero. It should be mentioned that models with  $M = 0.95 M_{\odot}$  and  $Z = 0.015$ , converged with a primordial (initial) composition of

**Table 4.6.** Calibrated stellar models with heavy element and helium diffusion data for  $\beta$  Hydri. Note the small amount of scatter in the results for models of equal metal abundance. This is due to the more evolved status of the star.

Diffusion Models, $M=1.10 M_{\odot}$				$\alpha = 1.73141$								
Mo.Ref	$X_r$	$Z_i$	$Z_r$	Age	$\log L/L_{\odot}$	$T_{\text{eff}}$ (K)	$\log g$	$\log P_c$	$\log T_c$	$\log D_c$	$Y_c$	$Z_c$
ZLT	0.7293	0.0110	0.0097	7.1005	0.5445	5801	3.9412	18.6727	7.3334	3.4760	0.9881	0.0119
ZL+	0.7871	0.0110	0.0098	6.9455	0.5544	5790	3.9278	18.7262	7.3386	3.5184	0.9882	0.0118
ZL-	0.7980	0.0110	0.0097	7.3036	0.5332	5802	3.9525	18.6391	7.3003	3.4494	0.9881	0.0119
ZT-	0.7858	0.0110	0.0100	7.2784	0.5452	5700	3.9098	18.8756	7.3596	3.6309	0.9881	0.0119
ZT+	0.7987	0.0110	0.0094	6.7951	0.5428	5891	3.9696	18.4969	7.3220	3.3304	0.9882	0.0118
Z-LT	0.8949	0.0070	0.0061	8.5337	0.5444	5801	3.9412	18.7924	7.3448	3.5701	0.9923	0.0077
Z-L+	0.8433	0.0070	0.0061	8.2389	0.5579	5801	3.9277	18.8301	7.3515	3.5976	0.9924	0.0076
Z-L-	0.8547	0.0070	0.0060	8.7882	0.5445	5801	3.9525	18.7595	7.3413	3.5445	0.9923	0.0077
Z-T-	0.8442	0.0070	0.0063	8.8030	0.5436	5695	3.9099	18.9826	7.3837	3.7048	0.9923	0.0077
Z-T+	0.8561	0.0070	0.0058	8.1491	0.5449	5899	3.9697	18.6059	7.3304	3.4199	0.9924	0.0076
Z+LT	0.7574	0.0150	0.0133	6.3634	0.5442	5800	3.9412	18.6238	7.3286	3.4374	0.9840	0.0160
Z+L+	0.7502	0.0150	0.0134	6.1385	0.5578	5801	3.9277	18.6662	7.3328	3.4713	0.9840	0.0160
Z+L-	0.7611	0.0150	0.1322	6.4540	0.5364	5812	3.9525	18.5752	7.3244	3.3981	0.9839	0.0161
Z+T-	0.7496	0.0150	0.0137	6.5882	0.5429	5692	3.9097	18.8347	7.3544	3.6003	0.9839	0.0161
Z+T+	0.7623	0.0150	0.0128	5.9862	0.5455	5901	3.9696	18.4438	7.3175	3.2869	0.9840	0.0160

**Table 4.6 Continued.** Seismology data. Compare to the data for  $\epsilon$  Eridani in Table 3.7, and to the work of Beddings2001. The large and small frequency spacings are significantly reduced.

Mo.Ref	Big, l=0 $\Delta v$ ( $\mu$ Hz)			Big, l=1 $\Delta v$ ( $\mu$ Hz)			Big, l=2 $\Delta v$ ( $\mu$ Hz)			Small, l=0 $\delta v$ ( $\mu$ Hz)		
	n=1-10	n=10-20	n=20-30	n=1-10	n=10-20	n=20-30	n=1-10	n=10-20	n=20-30	n=1-10	n=10-20	n=20-30
ZLT	59.442	57.015	61.883	43.498	47.376	61.312	37.125	47.188	54.497	0.000	0.000	3.172
ZL+	58.127	55.723	60.423	59.818	47.028	59.260	35.265	46.093	52.989	0.000	0.000	3.486
ZL-	60.606	58.119	62.477	37.150	49.191	62.700	35.107	48.172	55.572	0.000	0.000	4.135
ZT-	56.668	54.057	58.710	61.859	48.825	51.914	33.213	41.674	50.950	0.000	0.000	4.989
ZT+	61.972	59.799	63.974	40.698	53.737	64.239	38.516	49.345	57.331	0.000	4.841	4.846
Z-LT	59.395	57.061	55.194	49.800	46.928	53.076	33.871	46.982	47.764	0.000	0.000	2.993
Z-L+	58.036	55.798	53.752	49.551	47.787	48.161	33.090	42.901	49.899	0.000	0.000	0.000
Z-L-	60.561	58.181	56.451	45.323	47.989	56.320	35.749	52.157	48.910	0.000	0.000	3.604
Z-T-	56.651	54.237	57.960	39.499	48.014	51.401	33.529	45.027	50.848	0.000	0.000	0.000
Z-T+	61.888	59.933	63.628	51.296	52.071	63.655	36.820	48.711	56.403	0.000	0.000	5.204
Z+LT	59.369	56.949	61.211	35.201	48.042	61.343	34.938	47.126	54.447	0.000	0.000	3.702
Z+L+	58.008	55.666	59.728	60.864	46.765	59.641	36.573	46.036	53.099	0.000	0.000	3.849
Z+L-	60.482	58.061	62.343	43.018	50.822	62.551	34.320	49.024	55.406	0.000	0.000	4.581
Z+T-	56.638	53.998	58.056	69.274	47.489	51.975	32.084	40.559	53.330	0.000	0.000	0.000
Z+T+	61.830	59.706	63.973	41.751	53.943	64.259	40.733	49.228	57.333	0.000	4.896	4.970



~60 – 65% hydrogen, and that possibly indicates that the constraining uncertainties are too extreme.

At first glance Table 4.6 seems quite normal, but compare some of the information with Table 3.7, the diffusion models for  $\epsilon$  Eridani. Notice that according to  $\beta$  Hydri's position on the HR-diagram there are only a few evolutionary tracks that can transverse the uncertainty box. The effect, then, is to reduce the spread of ages and the calibrated composition. For example, the ages of models with similar metal abundance do not vary by more than ~0.7 Gyr, and compositions vary by no more than 0.07 in X and Y.

## 4.7 Seismological Results

The seismology of a star on the subgiant branch is quite different from that when the star was on the main sequence. The change in the pulsation spectrum develops as the star evolves. Evolved stars have smaller large frequency spacings mainly because of the larger stellar radius, and the small spacings become almost indistinguishable from the rest of the spectrum since they decrease because of the increasing complexity of the core. The effect of  $g$ -modes (mode bumping/mixing) plays a much larger role since they propagate at a higher frequency and influence higher radial order  $n$   $p$ -modes. Pulsation modes affected by mode bumping are displayed in Figure 4.4 for various models. The graph displays radial order  $p$ -modes ( $n_p$ ) plotted against the radial order of the  $g$ -modes ( $n_g$ ) for the harmonic degree  $l = 1$ . For no mode bumping the  $n_g$  values would be zero, but this figure shows that  $g$ -modes are dominant for low  $n$  and are still present even to high orders of  $n$  (~25).

# Effects of Mode Bumping in $\beta$ Hydri

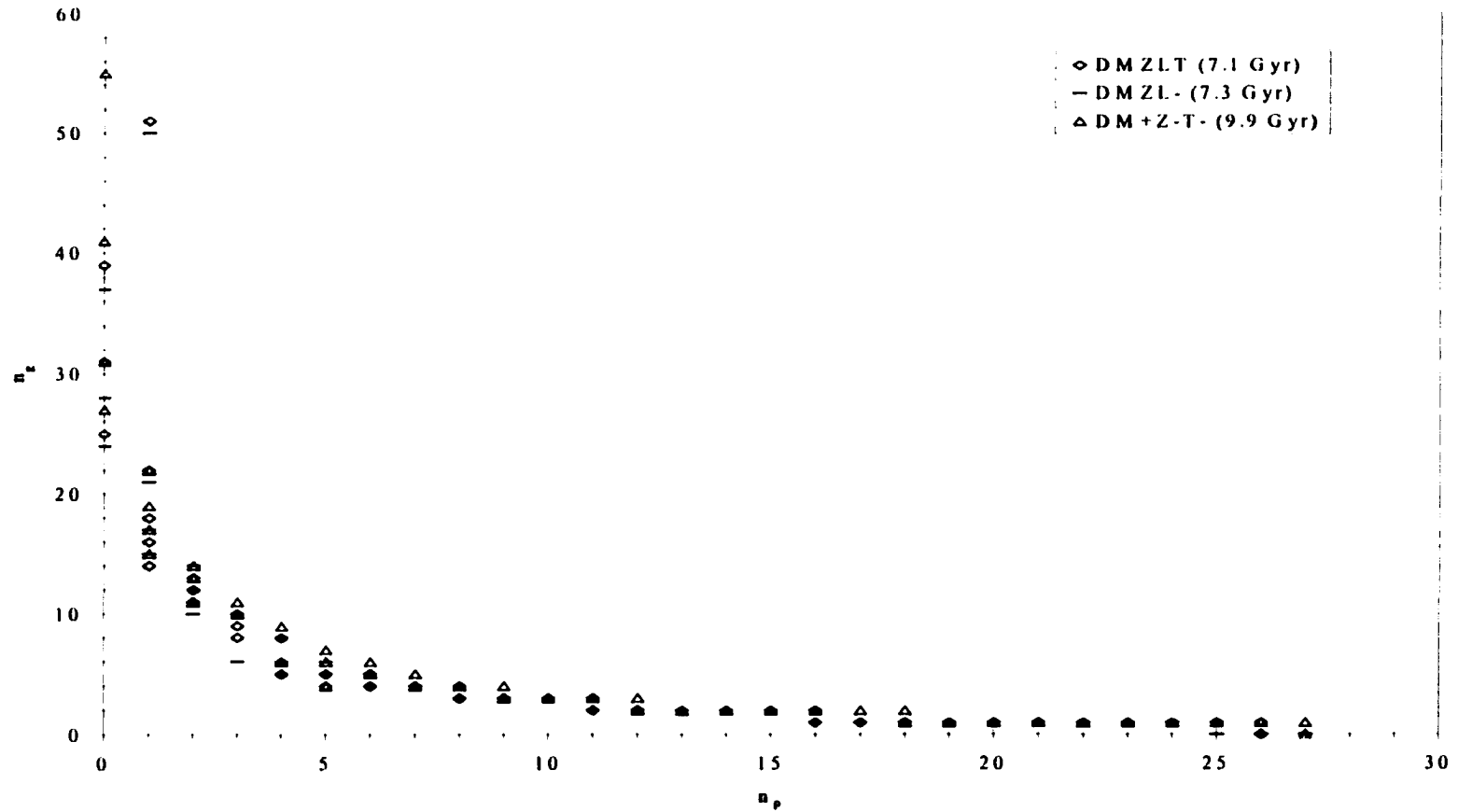


**Figure 4.4.** The effect of mode bumping in three models in the subgiant star  $\beta$  Hydri. It is not until large values of radial order are reached (i.e. far from the stellar core) that  $g$ -modes have a minimal affect. Low oscillation modes are severely contaminated by  $g$ -modes. Note the radial overtone  $n$  is equal to  $n_p - n_g$ .

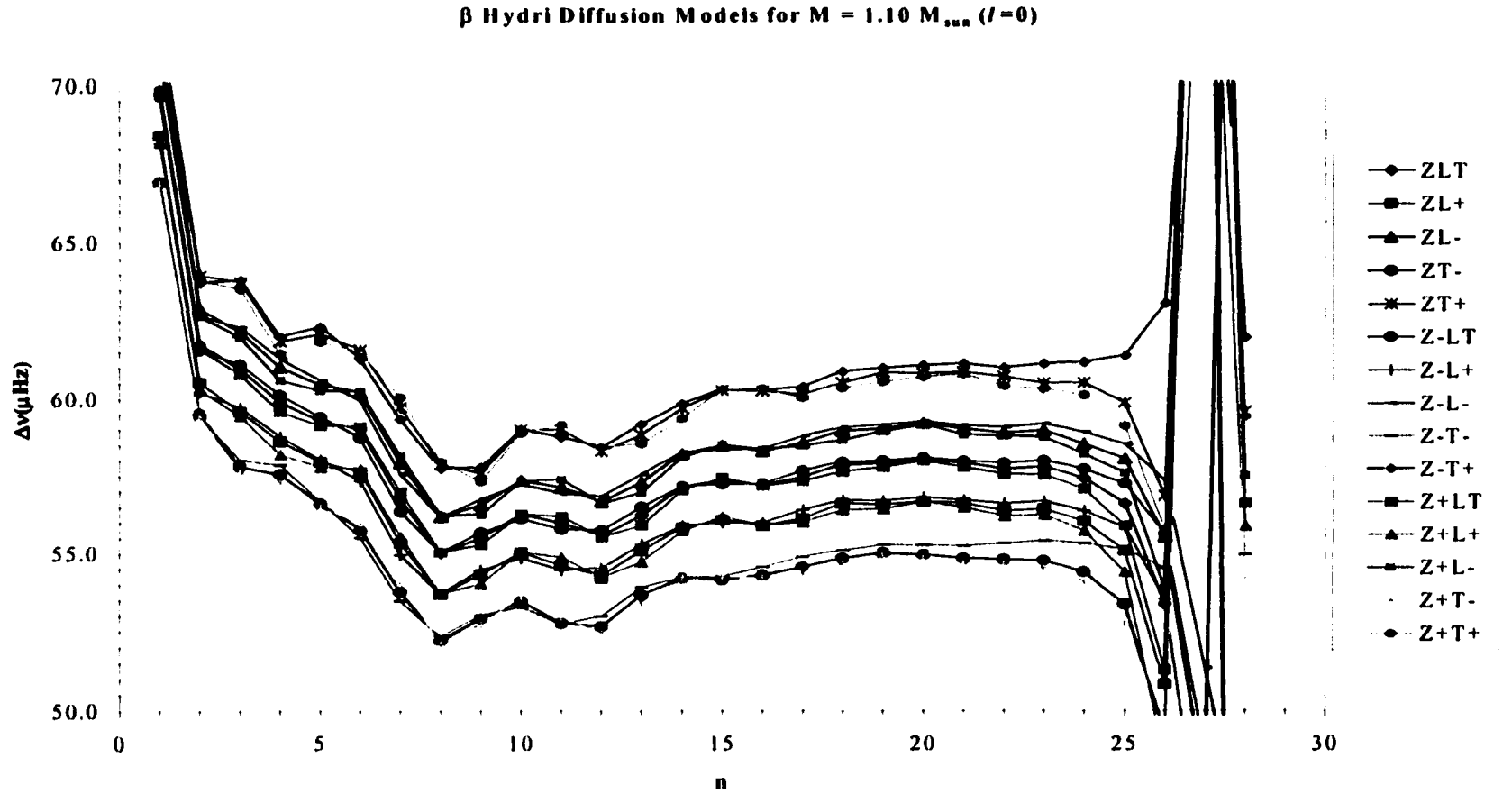


**Figure 4.5.** Large frequency spacing plotted against the radial order  $n$  for the  $l = 0$  harmonic. Note the relation of stellar radius with the large frequency spacing. Each of the five bands represents a model of similar radius. The chaotic behaviour for radial orders with  $n \geq 25$  is because the frequencies are near the acoustic cut-off. The radial harmonic mode is not affected by  $g$ -mode contamination (except at low  $n \leq 5$ ); compare this plot with Figure 4.6, the same models but for the  $l = 1$  mode.

The star is not evolved to limit the harmonic degree to the radial mode ( $l = 0$ ), as for giant stars, so there is good resolution when determining the large frequency spacing  $\Delta\nu$ . Figure 4.5 shows the large spacing as a function of the radial order,  $n$ , for the first fifteen diffusion models. There are three distinct models in each one of the “groupings” displayed here. That is because each group (or band) represents stellar models with a similar radius, i.e. models that converged to the same  $T_{\text{eff}}$ , and luminosity.

There is a frequency maximum for  $p$ -modes in a stellar atmosphere, above which the atmosphere is transparent to the acoustic waves. This is called the *acoustic-cutoff*, where the scale height becomes small in comparison with the wavelength of the oscillations and the  $p$ -modes are not reflected into the stellar interior ( $\omega_a \sim 1414 \mu\text{Hz}$  for  $\beta$  Hydri, Eq. 2.12). Figure 4.5 clearly shows this for  $n \sim 25$  ( $\nu_{n=25} \sim 1400 \mu\text{Hz}$ ), where the large frequency spacing is erratic. In the simulation, if a mode oscillates with a frequency near the acoustic-cutoff, then the adiabatic and non-adiabatic frequencies start to deviate significantly and the imaginary part of the non-adiabatic solution is positive and becomes larger. Because of that the iteration may converge to the incorrect mode and that could explain the discontinuities in Figure 4.5.

The radial harmonic  $l = 0$  is not affected by  $g$ -mode contamination (radial  $g$ -modes are not defined), so the large spacing varies relatively uniformly with radial order. Unfortunately, for harmonic modes of degree  $l > 0$  the  $g$ -modes become a factor. The mode bumping/mixing evidence is displayed in Figure 4.6. This plot is for the same models as in Figure 4.5, but for  $l = 1$   $p$ -modes that travel deep into the stellar interior. There is some linearity per model, but only for large frequency spacings about the range  $14 \leq n \leq 25$ . That plot (excluding the zero and very large values) shows that the majority

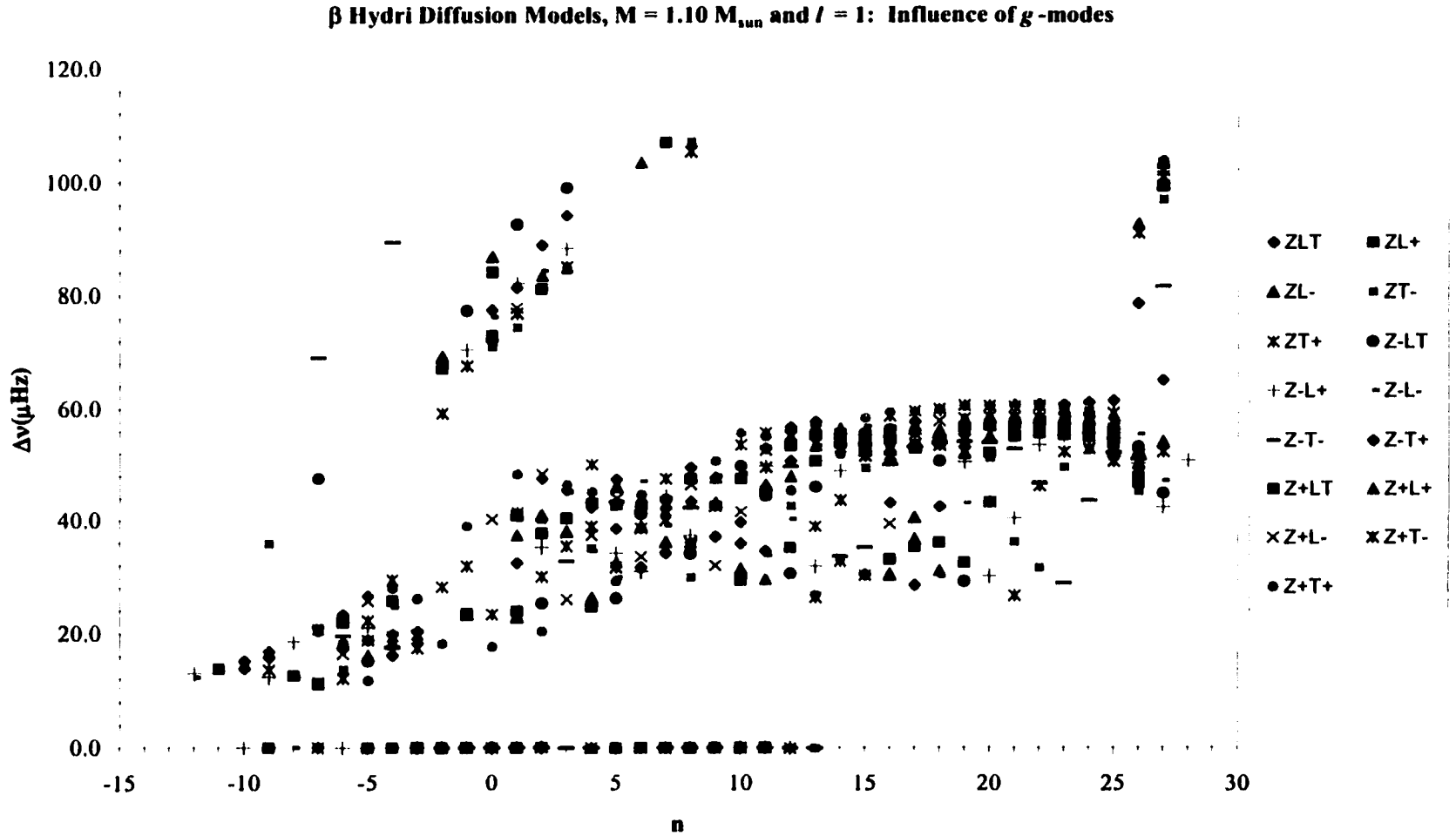


**Figure 4.6.** Similar to Figure 2.6, but for the  $l = 1$  harmonic degree. There is a large contamination by  $g$ -modes for  $n \leq 12$ , but there is some linearity for large frequency spacings in the range  $13 \leq n \leq 25$ . The acoustic-cutoff takes place for  $n \geq 25$ .

of the large spacings lie in a band  $\sim 15 - 20 \mu\text{Hz}$  wide. If observations are successful in determining large frequency spacings for  $l = 1$  &  $2$ , then the information here could possibly be used as a reference for the extent of  $g$ -mode activity in the pulsation spectrum of  $\beta$  Hydri. However, if any  $g$ -mode oscillations are successfully observed it will be a first for asteroseismology and can be used to refine stellar models further because  $g$ -mode frequencies are very sensitive to the stellar parameters.

The high molecular weight  $\mu$  of  $\beta$  Hydri's helium core (surrounded by a hydrogen burning shell) results in a decrease in the sound speed gradient, and consequently a decrease in the small frequency spacing  $\delta\nu$ . Figure 4.7 is a plot of  $\delta\nu$  (averaged over  $20 \leq n \leq 30$ ) vs. age for all the models. Only  $\langle n \rangle_{20-30}$  were used because small spacing values for the other  $n$ -averages were severely hampered by  $g$ -mode mixing and did not produce any results. One thing the figure does show is the sensitivity of  $\delta\nu$  to the parameters used to define the model. The relationship with age is not as distinct as it was for  $\epsilon$  Eridani, but it is there and can possibly be of some use. Most of the small spacing frequencies lie within a band between  $3$  and  $6 \mu\text{Hz}$ . If the data outside of this range are excluded, the results can still be fit with a linear regression line, but will be subject to a very large uncertainty ( $\sim 100\%$ ) in the slope. Even though the models did not produce a linear relation with age, if the small spacing is determined from observations then it can still provide a wealth of information. Because the scatter in Figure 4.7 is so high, an observed small frequency spacing can only be reproduced theoretically if the model parameters are refined.

As for  $\epsilon$  Eridani, the propagation diagram for  $\beta$  Hydri (central model) is shown in Figure 4.8. Immediately it can be seen that there are significant differences in the

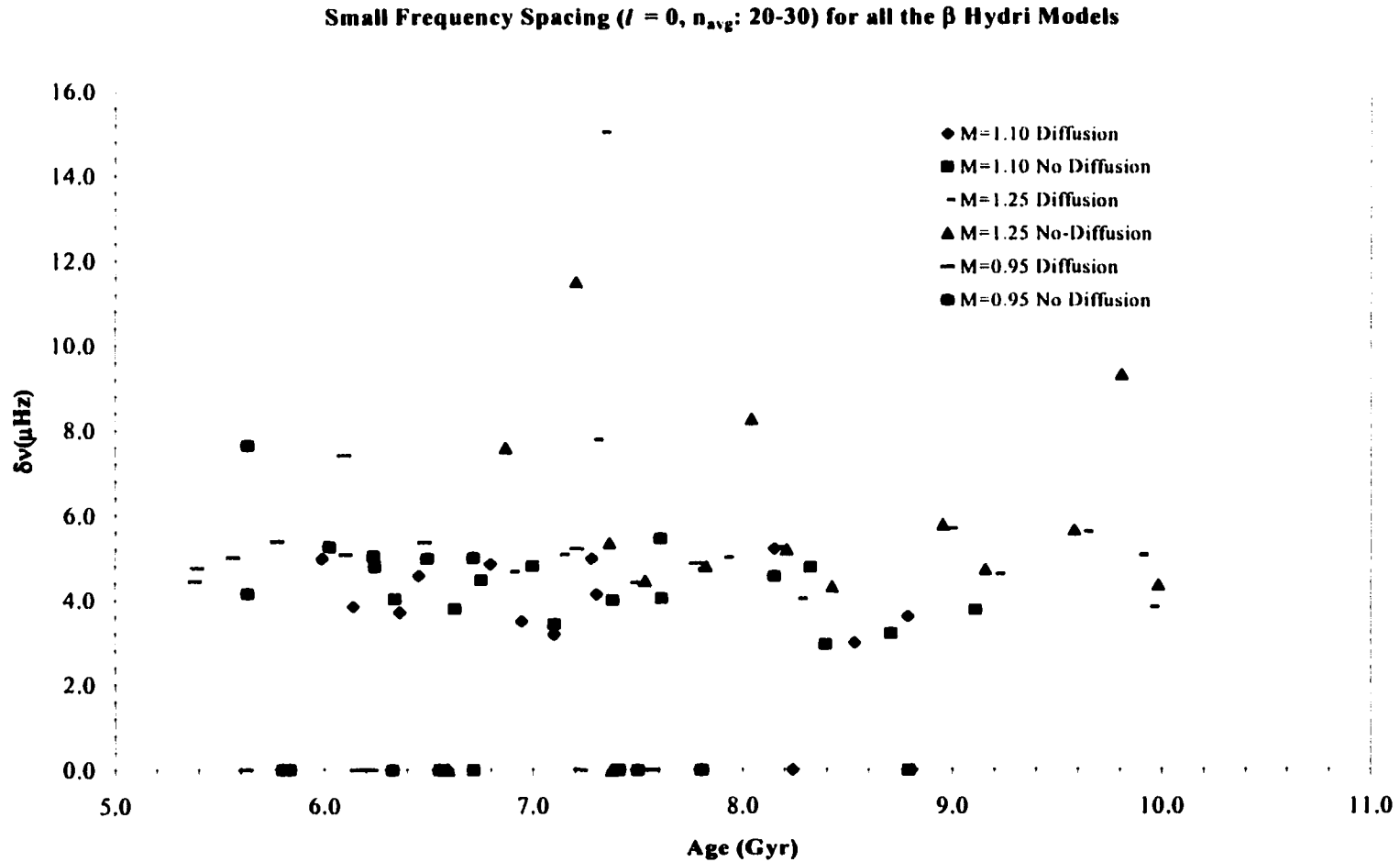


**Figure 4.7.** Small frequency spacing plotted against age for all models for the  $\langle n \rangle_{20-30}$  range. Aside from the erroneous values the majority of the data falls between 3 – 6  $\mu\text{Hz}$ , consistent with the findings of Bedding2001 ( $\delta\nu_0 \sim 5 \mu\text{Hz}$ ). Note that the diffusion models are more erroneous, i.e. very sensitive to the core composition.

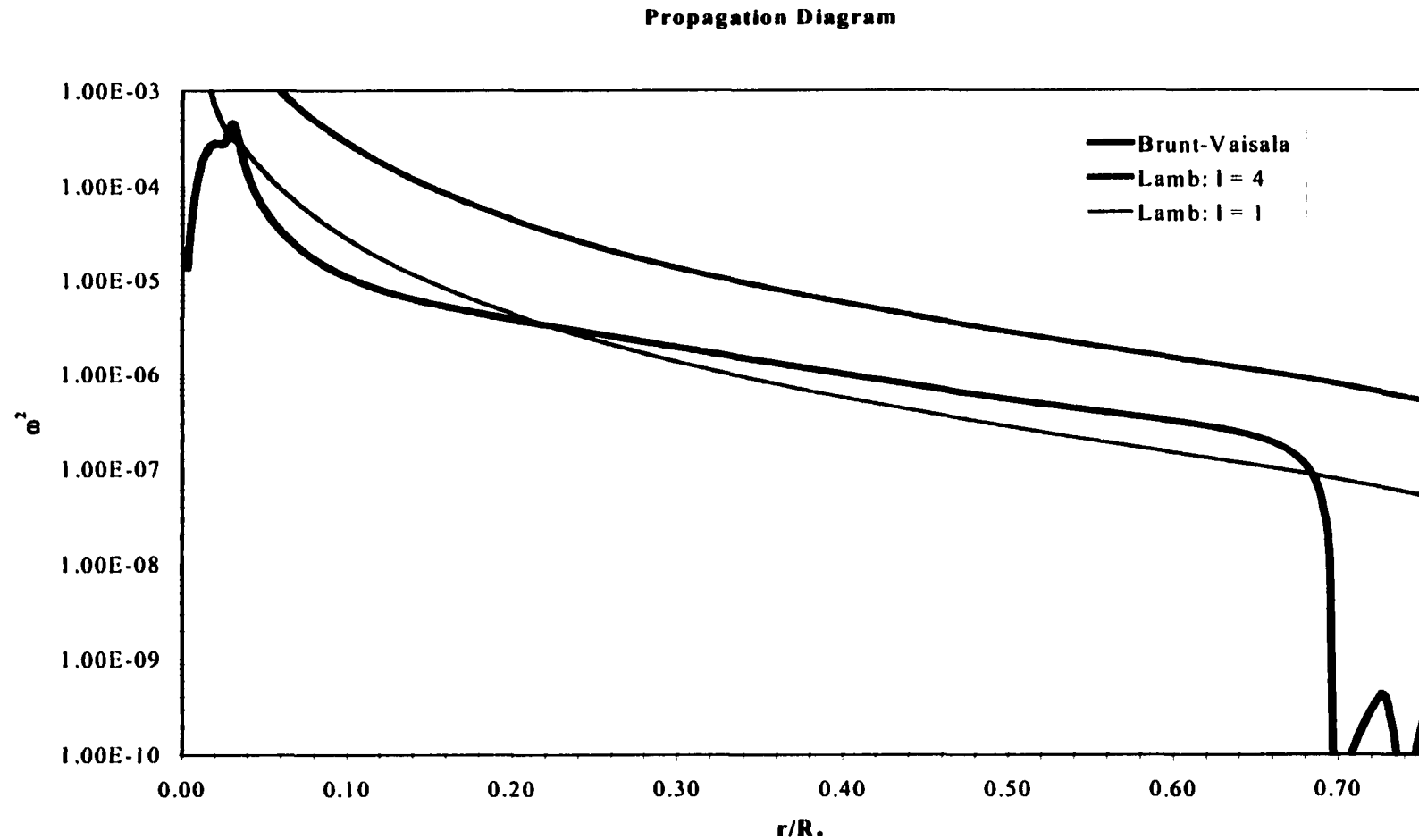


**Figure 4.8** The propagation diagram of a subgiant star is quite different from that of a main-sequence star. The Brunt-Väisälä frequency has a defined peak in the central region, and outside of about  $0.05 r/R$ , it decreases rapidly. The higher frequency peak results in the mixing of more modes; even the  $l = 4$  modes are not safe (see Figure 4.10). This represents the central model.



subgiant structure. Near the centre of the star the dense core allows  $g$ -modes to oscillate at a greater frequency, while the curve has a plateau and behaves very much like a main sequence star (Figure 3.8). Similarly to  $\epsilon$  Eridani and the Sun, Figure 4.8 shows an outer convection zone starting at about  $r = 0.7R_*$ . The higher frequency peak results in the mixing of more modes, see for example Figure 4.9, the eigenfunction (radial displacement) for an  $l = 4$  mode.

For most of the stellar interior this eigenfunction ( $l = 4$ ,  $n = 8$ ,  $\nu = 774.25 \mu\text{Hz}$ ) behaves like a  $p$ -mode, but at about  $0.05R_*$ , where  $N$  peaks, the oscillations take on a  $g$ -mode structure. The Lamb frequency for the same eigenfunction is also plotted in Figure 4.8. Its structure is similar to the  $l = 1$  plot, but has a higher frequency.

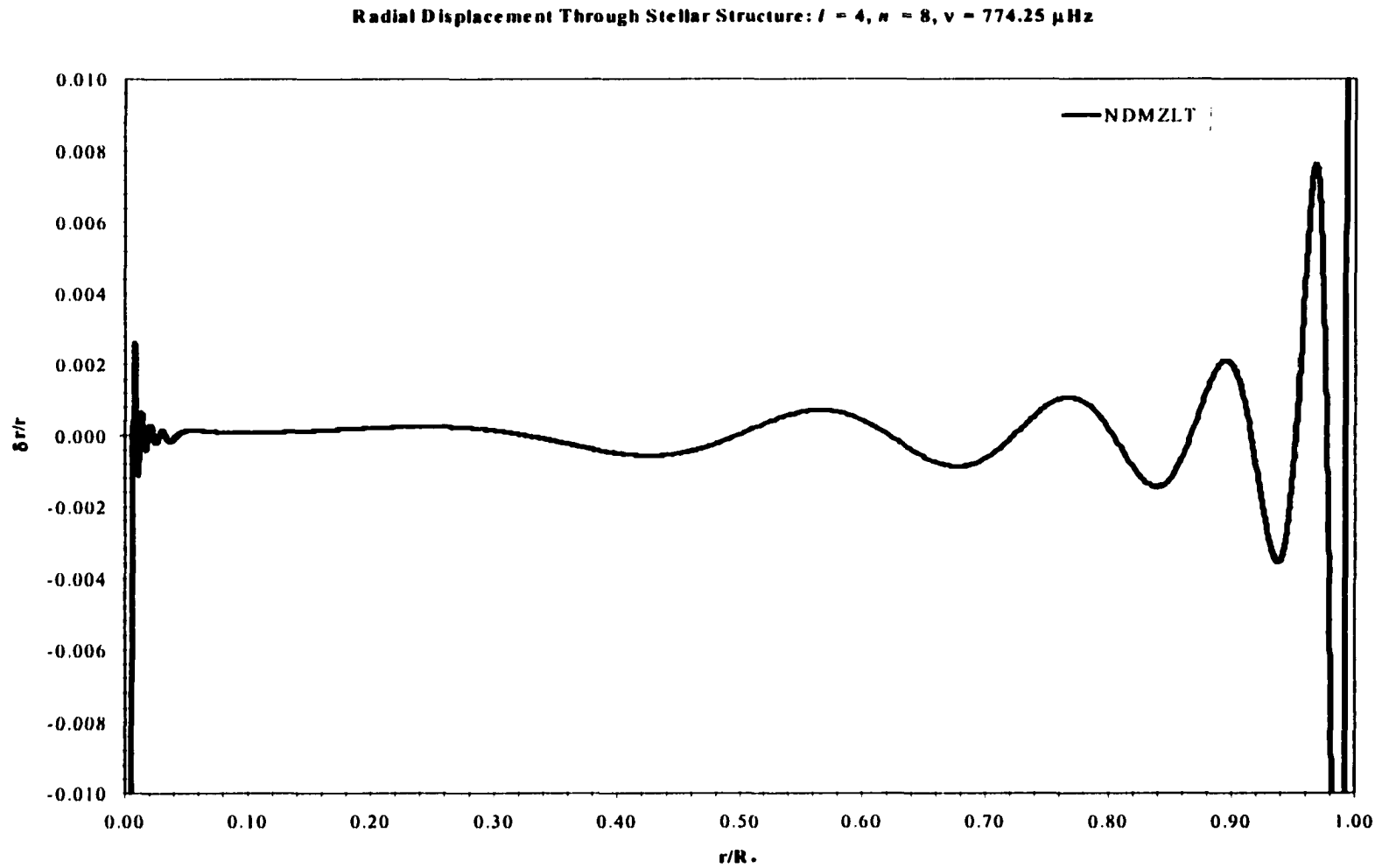


**Figure 4.9** An  $l = 4$  eigenfunction. For almost the entire structure of the star this  $l = 4$  mode behaves like a  $p$ -mode. However, at about  $r = 0.05R_*$ , where the Brunt-Väisälä frequency peaks, the mode oscillates with the properties of a  $g$ -mode.

# Chapter 5

## $\beta$ Geminorum

### 5. Introduction

Pollux,  $\beta$  Gem (K0 III) is one of the nearest giant stars to the Sun. At a distance of about 10 pc, Pollux has been subject to many observations prior to the early 1990s.<sup>1</sup> The majority of the observations were to analyze giant star properties, photometric and chromospheric research, and evolutionary status (Kelch *et al.* 1978; Schmitz and Ulmschneider 1980). To date there have been no seismological observations of Pollux, so the information discussed here is the first for the star. This chapter will review some of the early controversies over Pollux's mass, composition, effective temperature, and position on the HR-diagram. Following this, the results of the stellar models and seismological analysis are presented.

### 5.1 Observational Parameters

The apparent magnitude, colour, and parallax information are taken from the Hipparcos catalogue and are listed in Table 5.1. The values are not very different from what was found in the literature before the Hipparcos mission results ( $\pi = 94 \pm 6$  mas Hoffleit 1982).

---

<sup>1</sup>Pollux was observed recently with the Goddard High Resolution Spectrograph by Ostenetal *et al.* (1998). The information was presented at the AAS proceedings and has not yet been published.

**Table 5.1** Observational parameters taken from the Hipparcos catalogue.

Parameter	Hipparcos Value
$m_v$ .....	$1.16 \pm 0.02$
B–V.....	$0.991 \pm 0.005$
$\pi$ .....	$96.74 \pm 0.87$ (mas)

## 5.2 Photospheric Parameters

The majority of the observations of Pollux have been photometric or spectroscopic and have been used to infer its photospheric properties. The most recent investigation was carried out by Drake and Smith (1991; hereafter DS91). The large range of parameter values determined in previous works summarized in Table 5.2 (DS91), where  $[M/H]$  is the total metals-to-hydrogen ratio relative to the Sun, and  $\xi$  is the micro-turbulence.

What is obvious from the table is the diversity in the values. The effective temperature varies by about 500 K,  $\log g$  estimates range by 0.9 (a factor of 10 in standard units), and the metallicity is slightly better constrained, varying by about 0.3. The large scatter results mainly from the uncertainties involved in the model atmosphere analyses of giant stars. The uncertainties are the result of departures from local thermodynamic equilibrium (LTE). That severely hampers the ability to derive effective temperature and surface gravity using excitation and ionization equilibria, as well as skewing the results of abundance analyses for low surface gravity stars (DS91).

The most detailed analysis (of those listed in Table 5.2) was performed by Ruland *et al.* (1980) since they empirically traced departures from LTE in the excitation and ionization equilibria of iron-peak elements (Ti, Cr, and Fe), which resulted in an abundance significantly below solar. Steenbock (1985) and Holweger (1988) predicted the

**Table 5.2.** Summary of Pollux's photospheric parameters (DS91). The superscripts denote methods applied to derive effective temperatures and surface gravity: (e) derived from excitation equilibria; (g) differential curve of growth method; (i) derived from ionization equilibria; (k) based on the Ca II K line width-luminosity relation of Wilson (1976); (l) "average" of values gleaned from the literature; (m) derived from an estimated mass; (p) based on photometric material.  $\xi$  is the micro-turbulence., [M/H] is the metal-to-hydrogen ratio relative to the Sun.

$T_{\text{eff}}$	$\log g$	[M/H]	$\xi$ (km/s)	Authors
4896 <sup>p</sup>	2.8 <sup>k</sup>	-0.01	---	Bell and Gustafsson (1989)
4800 <sup>p</sup>	2.60 <sup>l</sup>	-0.10	1.5	Tomkin and Lambert (1983)
4950 <sup>e</sup>	2.48 <sup>i</sup>	+0.16	2.0	Gratton <i>et al.</i> (1983)
5060 <sup>e</sup>	3.12 <sup>i</sup>	+0.02	1.5	Lambert and Ries (1981)
4840 <sup>p</sup>	2.24 <sup>i</sup>	-0.10	1.4	Ruland <i>et al.</i> (1980)
4750 <sup>p</sup>	2.3 <sup>i</sup>	---	1.5	Tomkin and Lambert (1979)
4700 <sup>l</sup>	2.7 <sup>l</sup>	+0.00	1.2	Lambert and Ries (1979)
4890 <sup>g</sup>	2.5 <sup>g</sup>	-0.01	---	Griffin (1976)
4680 <sup>p</sup>	2.9 <sup>m</sup>	-0.05	1.8	Gustafsson <i>et al.</i> (1974)
4793 <sup>p</sup>	2.9 <sup>m</sup>	-0.17	---	Williams (1971)
4750 <sup>p</sup>	2.8 <sup>m</sup>	0.00	---	Conti <i>et al.</i> (1967)

same non-LTE affects as those observed by Ruland *et al.* using detailed radiative and statistical equilibrium calculations for a model iron atom.

The effective temperature, surface gravity, and metallicity chosen for this work's stellar modeling came directly from DS91. They used an analogous method to derive the parameters for  $\epsilon$  Eridani (DS93), which is based on the Smith and Drake (1987) analysis of calcium and iron lines. The major difference for Pollux is the treatment of non-LTE effects on the model. A non-LTE study of neutral calcium using simultaneous radiative transfer – statistical equilibrium calculations and model stellar atmospheres was performed by Drake (1991). Drake (1991) shows that individual multiplets of Ca I occur, indicating widely different surface abundances of Ca among giant stars.

Using the groundwork of Drake (1991), DS91 obtain an effective temperature,  $T_{\text{eff}} = 4865 \pm 50$  K, metallicity  $[\text{Fe}/\text{H}] = -0.04 \pm 0.05$ , and a logarithmic surface gravity  $\log g = 2.75 \pm 0.15$ .

### 5.3 Mass and Evolutionary Status

In one of the first detailed analyses, Ruland *et al.* (1980) calculate a mass for Pollux of  $M = 0.53^{+0.67}_{-0.33} M_{\odot}$ . They used their derived surface gravity,  $\log g = 2.24 \pm 0.35$  and radius  $R = 9.1 \pm 0.6 R_{\odot}$ . The radius was calculated using an angular diameter of  $\phi = 8.0 \pm 0.29$  mas (Blackwell and Shallis 1977) and parallax  $\pi = 95 \pm 6$  mas (Woolley *et al.* 1970). In the same manner, DS91 calculate a mass of  $M = 1.7^{+0.7}_{-0.5} M_{\odot}$  from their surface gravity, stellar angular diameter  $\phi = 7.4 \pm 0.15$  mas (Blackwell *et al.* 1990), and parallax  $\pi = 94 \pm 6$  mas (Hoffleit 1982). That leads to the question of the evolutionary status of

Pollux. Pollux's position on the HR-diagram was found to be the same by both Ruland *et al.* and DS91, but the ambiguity is whether Pollux is ascending the giant branch for the first time or at a stage after the helium flash.

Prior to any discussion of the evolutionary status of Pollux, the possibility that it is a low-mass star can be ruled out instantly. Pollux is unarguably a star that has evolved off the main-sequence, but a  $0.53 M_{\odot}$  star will burn hydrogen in the core for a time longer than the current age of the universe (unless Pollux has suffered major mass loss). The efforts by Ruland *et al.* to determine an evolutionary state are not invalid since they infer Pollux's structure by other means.

Ruland *et al.* analyzed the surface chemical abundance of carbon and nitrogen and suggested that Pollux is most likely ascending the giant branch for the first time. They suggest that the Li and Be surface abundance may provide much needed evidence of Pollux's evolutionary state.

The regions of the HR-diagram for spectral type K0 contain many over-lapping evolutionary tracks, making an accurate evolutionary track determination difficult. A follow-up analysis by DS91 draws the same conclusion as Ruland *et al.*, that an exact determination of Pollux's evolutionary stage cannot be determined without accurate stellar models. What is known for certain is that Pollux is a star with a mass of about 1.7 solar masses. The evolutionary status of the YREC models used in this work are discussed in § 5.4.

The inferred mass is also supported by the recent theoretical work of Allende Prieto and Lambert (1999). They use an interpolation of theoretical isochrones (models of Bertelli *et al.* 1994) in conjunction with the Hipparcos data to obtain a mass of  $M = 1.7$

$\pm 0.4 M_{\odot}$  ( $\log g = 2.77 \pm 0.24$ ). This is in very good agreement with DS91, and supports the calcium line width method for determining stellar parameters. It is the mass range centred on the mass from Allende Prieto and Lambert (1999) that I adopted for the stellar models. The complete set of model parameters is given in Table 5.3.

**Table 5.3** Stellar Evolution Parameters.

M.....	$1.7 \pm 0.4 M_{\odot}$
Z.....	$0.016 \pm 0.006$
$\log L/L_{\odot}$ .....	$1.631 \pm 0.014$
$\log T_{\text{eff}}$ .....	$3.687 \pm 0.0045$

## 5.4 Stellar Evolution Models

With the parameters in Table 5.3 and YREC, I produced 27 evolutionary models for Pollux. Figure 5.1 displays nine of the models that cover all the variations of mass and composition for the adopted central luminosity. Pollux had to be modeled differently from other stars in that all the models were evolved without diffusion, and YREC did not automatically calibrate the composition to evolve to a desired luminosity and effective temperature. The reason for that is  $\beta$  Gem's position on the HR-diagram, the giant branch, where the tracks are nearly vertical and may overlap. The uncertainty in effective temperature is small, which limits the number of tracks (which are very sensitive to the initial composition) passing through the star's uncertainty range.

The evolution models that were forced to evolve to the star's position on the HR-diagram only converged on the HR-diagram position if the initial (primordial) composition was on the order of 50 – 60 % helium, a very improbable system. Because of that the models were evolved to the giant branch at the star's luminosity, and no specific attempt was made to adjust the composition so that the star's  $T_{\text{eff}}$  lay within the



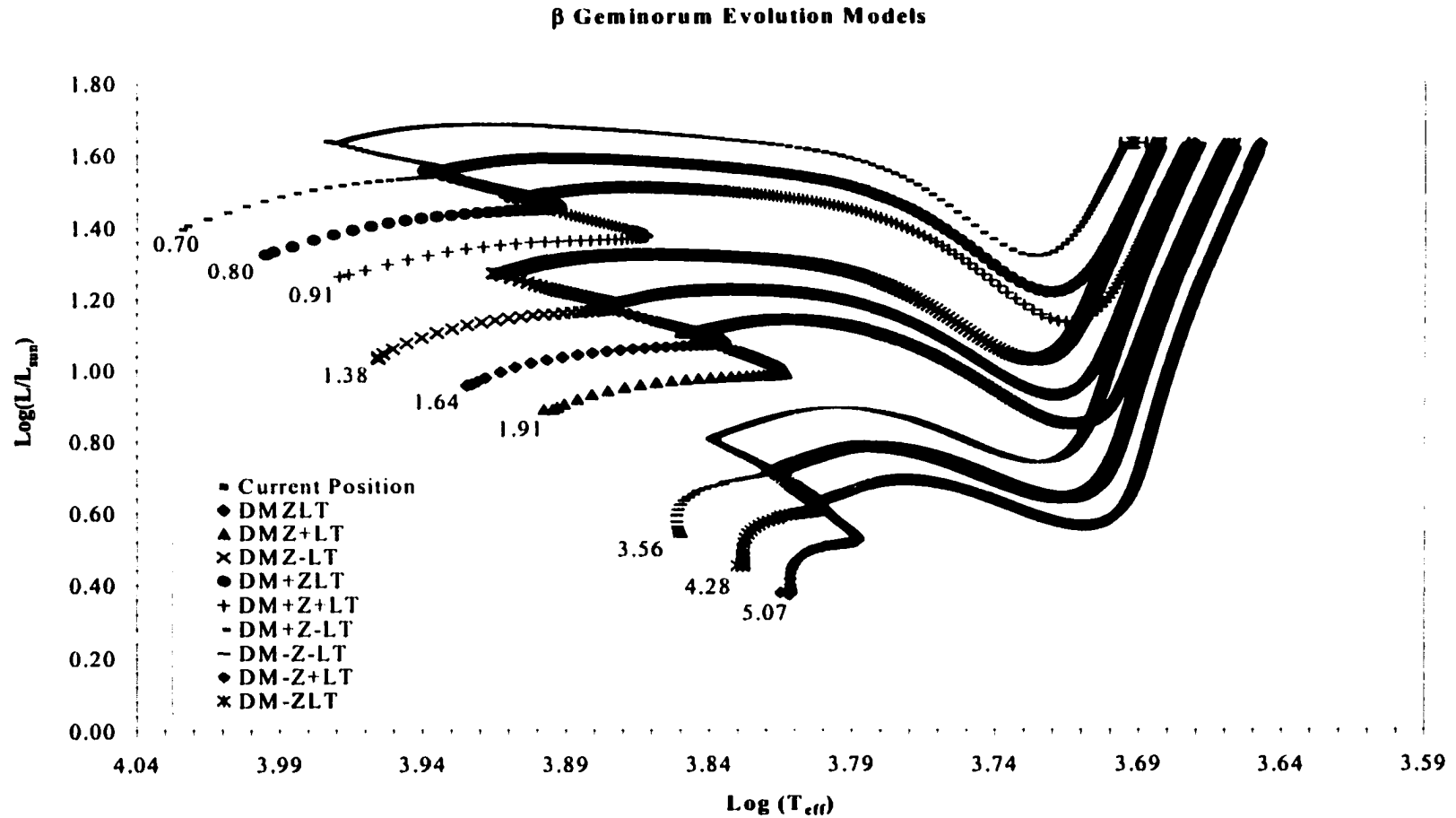


**Figure 5.1** Nine of 27 evolution models for  $\beta$  Gem. The models are not calibrated, but rather stopped at the desired luminosity (see text). Models shown here are evolved to the central luminosity. The above results show a discrepancy in the effective temperature or the physics of the models. Note also the overlapping tracks. The numbers at the base of each model is the age of the model.

uncertainties. All the models have  $Y = 0.270$ . As Figure 5.1 shows, the uncertainty in the stellar parameters allows models to pass through the observational error box, but only near the uncertainty extremes. The fact that only a few models actually pass through the determined HR-diagram position is not of great significance. The spread of the models resulting from the uncertainty in mass is the important feature of Figure 5.1.

This is an example of the potential of constraining stellar parameters with stellar model physics and asteroseismology. Since the models were not calibrated to  $T_{\text{eff}}$ , the resulting spread of models vary in effective temperature by about 525 K, ten times as much as the observational uncertainty. Seismological observations of  $\beta$  Gem can help improve our poorly determined physical parameters of the star.

A summary of the  $1.70 M_{\odot}$  model characteristics is given in Table 5.4. All the evolutionary models produced by YREC for Pollux have it ascending the red giant branch. It has not commenced core helium burning. Seismological observations will be able to test if Pollux is indeed ascending the giant branch for the first time. I have not calculated asymptotic giant branch models for Pollux owing to time constraints.

## 5.5 Seismology Results

The seismological analysis of giant stars is limited to the radial  $l = 0$  mode. Modes of higher harmonic degree are severely mixed with high radial order  $g$ -modes, which behave like  $p$ -modes in the sparse convective envelope of the giant star. The pulsation results for all 27 models are given in Table 5.5. The large frequency spacing (averages) varies from about  $3.76 - 7.77 \mu\text{Hz}$ , and is in good agreement with predictions based on simple radius scaling arguments,  $\Delta\nu_0 \approx 6.4 \mu\text{Hz}$ .

**Table 5.4** Properties for all the  $1.70 M_{\odot}$  models. There was no heavy element or helium diffusion and the models were not calibrated in composition. Each evolution started with a helium abundance of  $Y = 0.270$ . All models are evolved independent of temperature so “T” is not written.

<b>Non-Diffusion Models, <math>M = 1.70 M_{\text{sun}}</math></b>				<b><math>\alpha = 1.60471</math></b>							
<b>Mo.Ref</b>	<b>X<sub>r</sub></b>	<b>Z<sub>i</sub></b>	<b>Age</b>	<b>log L/L<sub>sun</sub></b>	<b>T<sub>eff</sub> (K)</b>	<b>log g</b>	<b>log P<sub>c</sub></b>	<b>log T<sub>c</sub></b>	<b>log D<sub>c</sub></b>	<b>Y<sub>c</sub></b>	<b>Z<sub>c</sub></b>
MZL	0.7042	0.0160	1.6396	1.6309	4628	2.6512	21.2281	7.5956	5.2271	0.8040	0.0160
MZL+	0.7042	0.0160	1.6411	1.6443	4619	2.6345	21.2364	7.5967	5.2324	0.8040	0.0160
MZL-	0.7042	0.0160	1.6380	1.6159	4638	2.6698	21.2185	7.5943	5.2210	0.8040	0.0160
MZ+L	0.6982	0.0220	1.9059	1.6307	4522	2.6110	21.2427	7.5787	5.2378	0.7080	0.0220
MZ+L+	0.6982	0.0220	1.9074	1.6443	4513	2.5942	21.2509	7.5804	5.2430	0.7080	0.0220
MZ+L-	0.6982	0.0220	1.9045	1.6170	4530	2.6281	21.2343	7.5771	5.2326	0.7080	0.0220
MZ-L	0.7096	0.0100	1.3847	1.6310	4763	2.7010	21.2067	7.6214	5.2112	0.9900	0.0100
MZ-L+	0.7096	0.0100	1.3861	1.6444	4754	2.6844	21.2161	7.6220	5.2172	0.9900	0.0100
MZ-L-	0.7096	0.0100	1.3830	1.6162	4773	2.7194	21.1963	7.6208	5.2045	0.9900	0.0100

**Table 5.5** Large frequency spacing for all stellar evolution models. Note that the calculations were for the  $l = 0$  (radial mode) only because all higher degree modes are very closely spaced in the sparse atmosphere and are mixed modes. Compare these values with those of Table 3.7 ( $\epsilon$  Eridani), the much larger large frequency spacing values of a main-sequence star.

Large, $l = 0$			$\Delta\nu$ ( $\mu\text{Hz}$ ) Non-Diffusion Models								
Mo.Ref	n=1-10	n=10-20	n=20-30	Mo.Ref	n=1-10	n=10-20	n=20-30	Mo.Ref	n=1-10	n=10-20	n=20-30
MZL	5.548	5.622	5.255	M+ZL	6.864	6.868	6.423	M-ZL	4.340	4.428	4.137
MZL+	5.384	5.46	5.105	M+ZL+	6.607	6.619	6.180	M-ZL+	4.204	4.284	4.008
MZL-	5.735	5.808	5.428	M+ZL-	7.079	7.079	6.640	M-ZL-	4.473	4.562	4.260
MZ+L	5.16	5.229	4.901	M+Z+L	6.343	6.351	5.953	M-Z+L	4.058	4.143	3.877
MZ+L+	5.007	5.077	4.758	M+Z+L+	6.154	6.166	5.787	M-Z+L+	3.936	4.013	3.762
MZ+L-	5.318	5.387	5.048	M+Z+L-	6.543	6.545	6.153	M-Z+L-	4.190	4.274	3.997
MZ-L	6.072	6.151	5.728	M+Z-L	7.560	7.564	7.032	M-Z-L	4.738	4.834	4.507
MZ-L+	5.895	5.977	5.566	M+Z-L+	7.282	7.291	6.791	M-Z-L+	4.590	4.677	4.365
MZ-L-	6.275	6.355	5.912	M+Z-L-	7.772	7.769	7.234	M-Z-L-	4.889	4.987	4.650

Like stars themselves, the pulsation spectrum evolves over time and changes with stellar structure. As mentioned in § 2.2.1, the regions of  $p$ - and  $g$ -mode propagation are defined by the Brunt-Väisälä,  $N$ , and Lamb,  $L_l$ , frequencies, and are shown here for Pollux in Figure 5.2. A comparison of this figure to the propagation diagrams of  $\epsilon$  Eridani (Figure 3.8) and  $\beta$  Hydri (Figure 4.9) reveals a peak frequency orders of magnitude larger than those of the other stars. The  $g$ -modes are effectively trapped by the gradient in the mean molecular weight  $\mu$ , and sharp changes in  $\mu$  enhance the buoyancy-restoring force to create the central peak in Figure 5.2. Even though the peak is confined to the central (core) region of the giant star, the  $g$ -modes propagate with such a high frequency that they overlap the  $p$ -mode spectrum (Guenther *et al.* 2000). Any observed frequencies with a harmonic degree greater than zero will then be a mixture of very closely spaced  $g$  and  $p$ -modes (the nomenclature from Scuflaire 1974 is to use negative and positive  $n$ -values to denote  $g$ -modes and  $p$ -modes, respectively).

Figure 5.2 also displays the Lamb frequencies for the  $l = 1$  and  $l = 3$  modes, and note that the  $l = 3$  frequencies have the  $l = 1$  structure. Recall that  $p$ -modes propagate with frequencies higher than both the  $L_l$  and  $N$  frequencies, and  $g$ -modes must have lower frequencies. The Brunt-Väisälä frequency very quickly goes to zero in the large convective envelope of the giant star (Figure 5.2 only displays the inner 10% of the star's structure).

Another difference between giants and less evolved stars is the location of the inner turning point for an mode. The relatively rarified envelope of the giant star allows modes of high degree to propagate to greater depths before the horizontal wave velocity equals that of the local sound speed. Examples of two selected eigenfunctions for the central

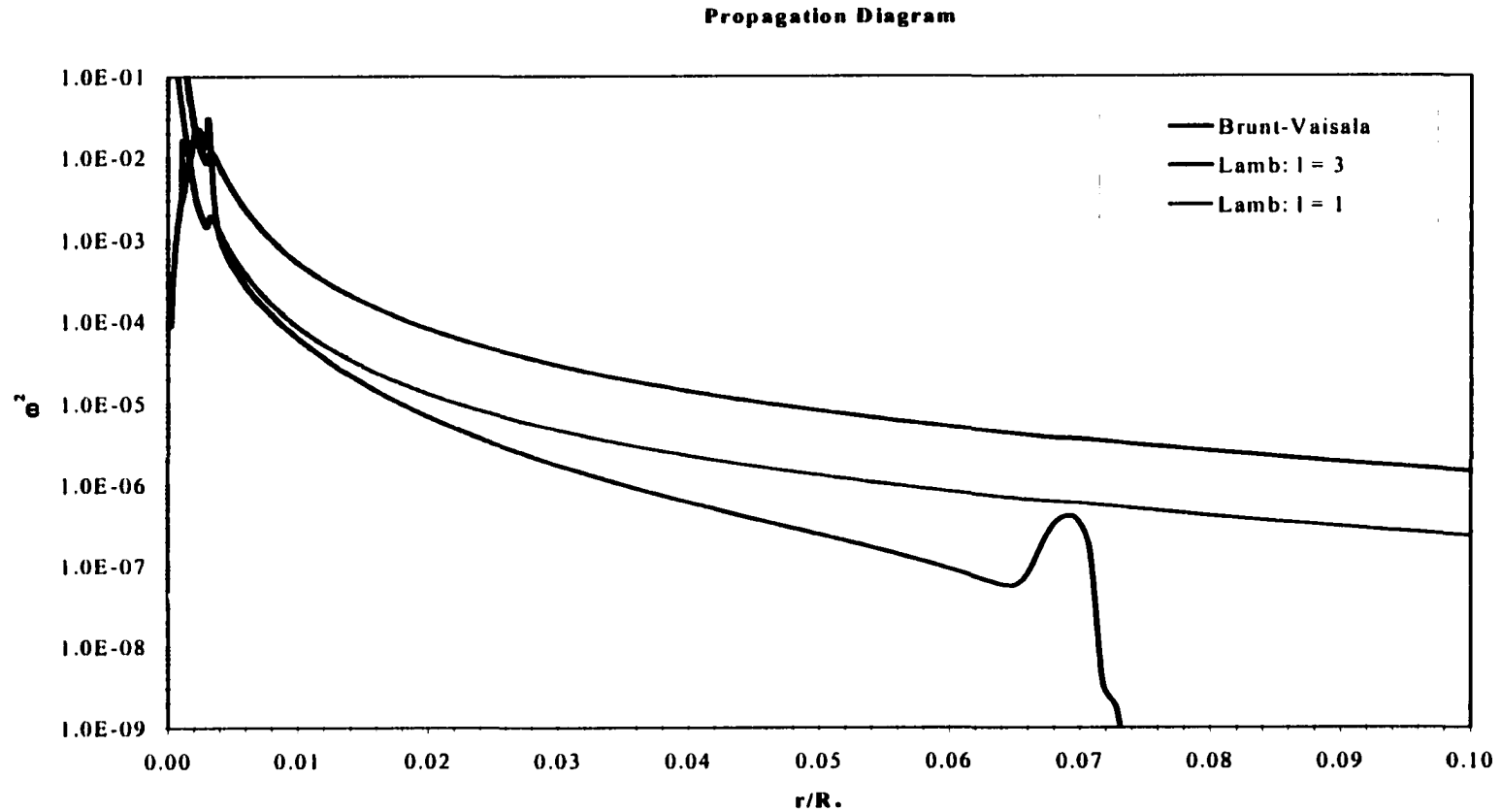


**Figure 5.2** Propagation diagram for Pollux which defines the region of wave oscillation. The Brunt-Väisälä frequency is independent of harmonic degree, but the Lamb frequency is sensitive to this value. Compare this figure with the propagation diagram of  $\epsilon$  Eridani and  $\beta$  Hydri (Figures 3.8, and 4.9, respectively). Here the Brunt-Väisälä frequency may only be significant very near the core but its high, sharp peak influences the entire star. The Brunt-Väisälä frequency is damped and is erratic in the large convective envelope of the giant star.

$\beta$  Gem,  $l = 3$ ,  $n = -55$ ,  $\nu = 300.80$  mHz

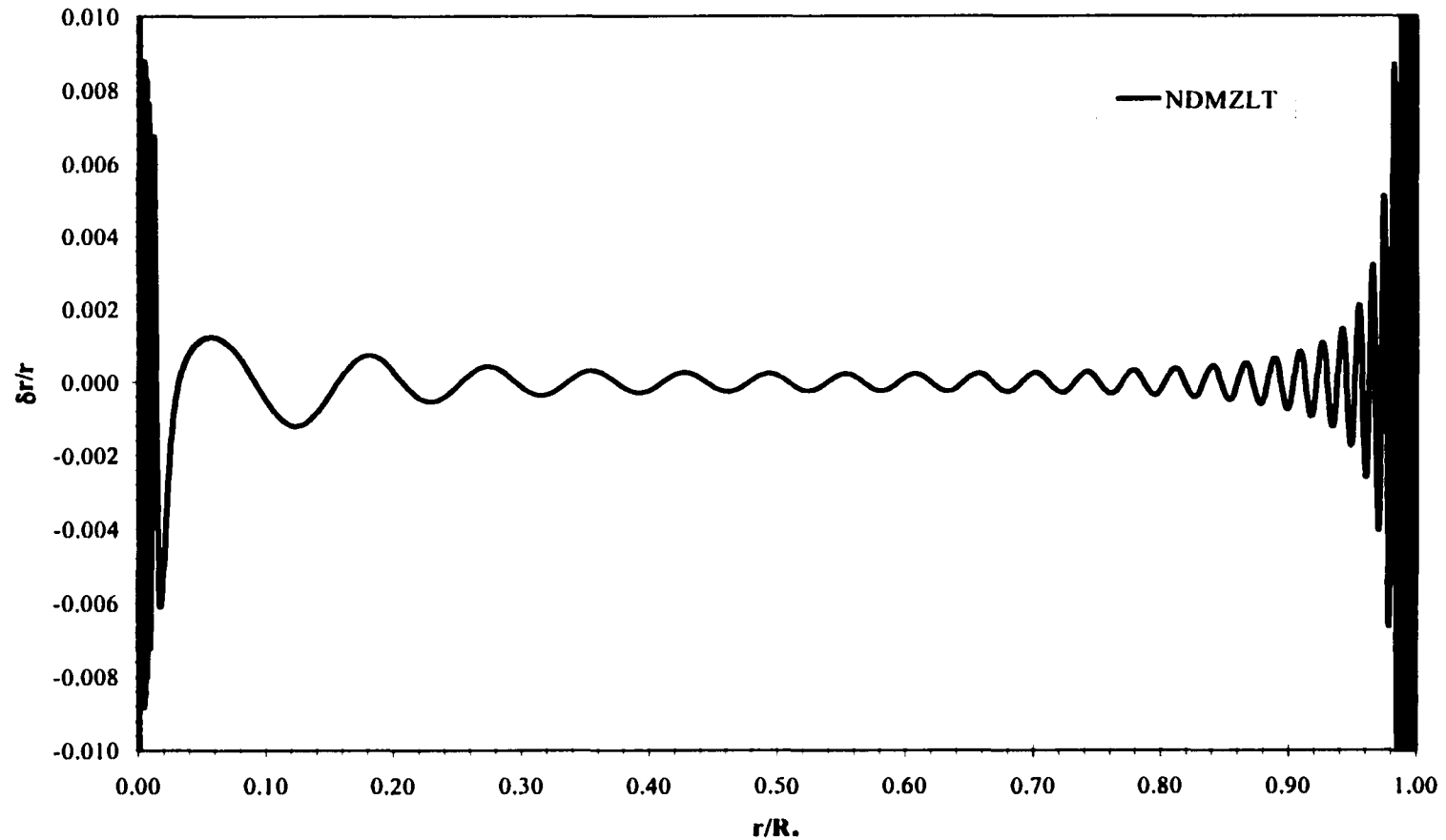


**Figure 5.3** Frequencies for an  $l = 3$   $p$  ( $g$ ) -mode. This is an excellent example of the effects of mode mixing. In the outer layers of the star the oscillation behaves like a  $p$ -mode, and at about  $0.55R_*$  the mode has  $g$ -mode properties throughout the stellar interior.

(NDMZL) model are shown in Figures 5.3 and 5.4. Figure 5.3 is for an  $l = 3$ ,  $n = -55$ ,  $\nu = 300.80 \mu\text{Hz}$  eigenfunction, and is an excellent example of the effects of mode mixing. For the outer 45% of the star the mode has  $p$ -mode-like oscillatory behavior and the amplitude decreases moving toward the centre. However, the radial displacement begins to increase in amplitude at about  $0.55R_*$  since the oscillation now has the characteristics of a  $g$ -mode. The different characteristics of a mixed mode are a result of the different phases of the radial and horizontal components of the oscillation for  $p$ -modes and  $g$ -modes (see Unno *et al.* 1989, p. 139-149).

Similarly, Figure 5.4 is the eigenfunction  $l = 40$ ,  $n = 43$ , and  $\nu = 300.52$ . Here the turning point is clearly resolved and located around  $0.5R_*$ . The result is quite different from its main-sequence counterpart where it is reflected at a smaller radius fraction and has larger amplitudes.

The large spacing is plotted for all the models (evolved to the central luminosity) in Figure 5.5,  $\Delta\nu_0$  vs.  $n$ , radial order for the  $l = 0$  mode. Except for a discrete number of the radial order values, the large spacing behaves as expected. The deviations are the result of misidentified modes in the pulsation code. Aside from the few variant modes, the results here are in good agreement with predictions of  $\Delta\nu \sim 6.4 - 6.9 \mu\text{Hz}$ .

The small frequency spacing will likely not be observed since it requires the presence of the  $l = 2$  frequencies (Refer to Equation 2.19, an  $l + 2$  harmonic degree mode is required). That means an age determination will have to be made in conjunction with stellar models. If the models in Figure 5.1 are constrained in temperature, then the age of  $\beta$  Gem is could possibly be around  $0.50 - 0.90$  Gyr (the 2.10 solar mass models). The variation of age with the large frequency spacing is shown in Figure 5.6, and the linearity



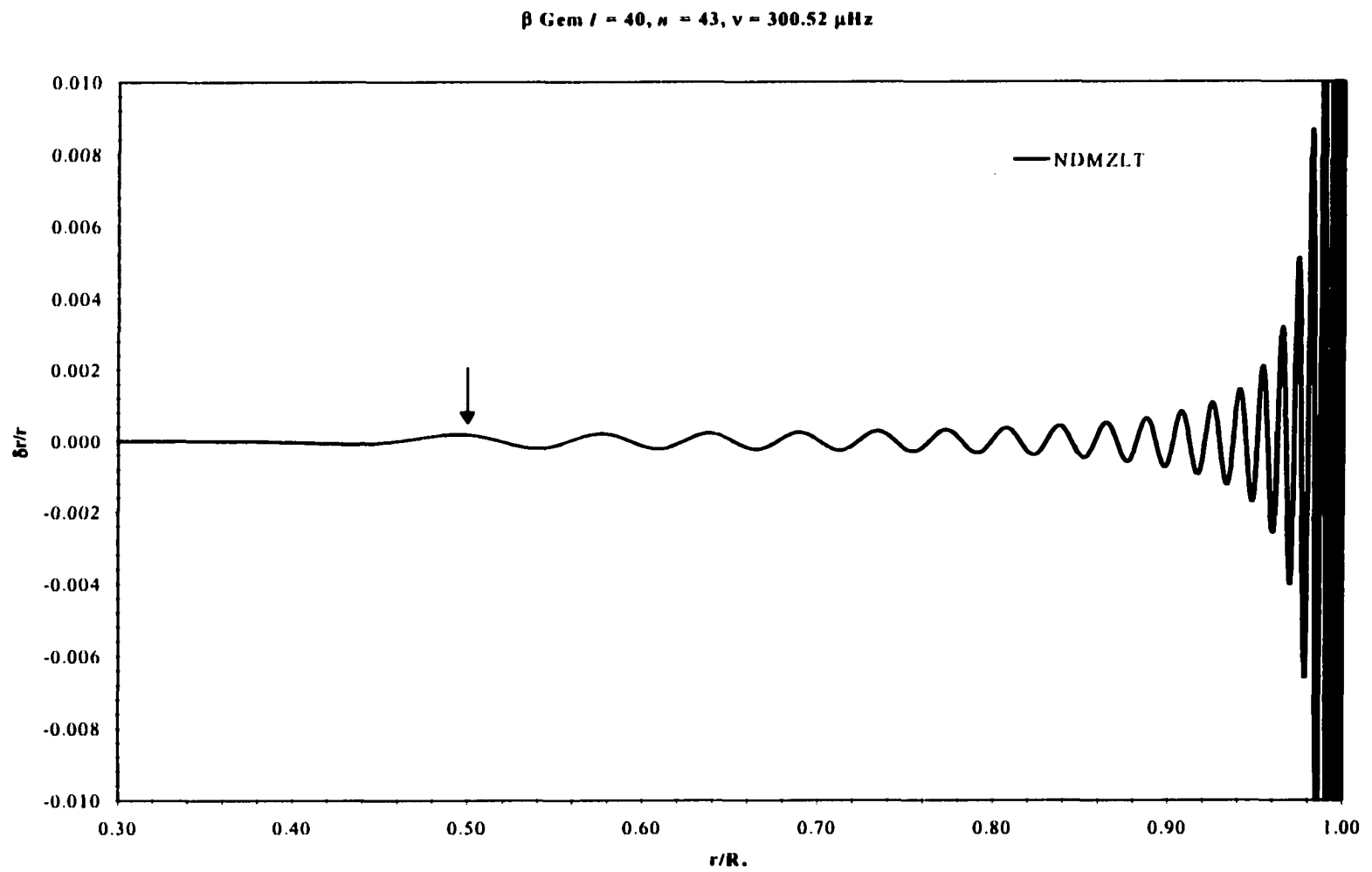


**Figure 5.4** Eigenfunctions for an  $l = 40$   $p$ -mode. Here the turning point appears to be around halfway to the centre of the star.

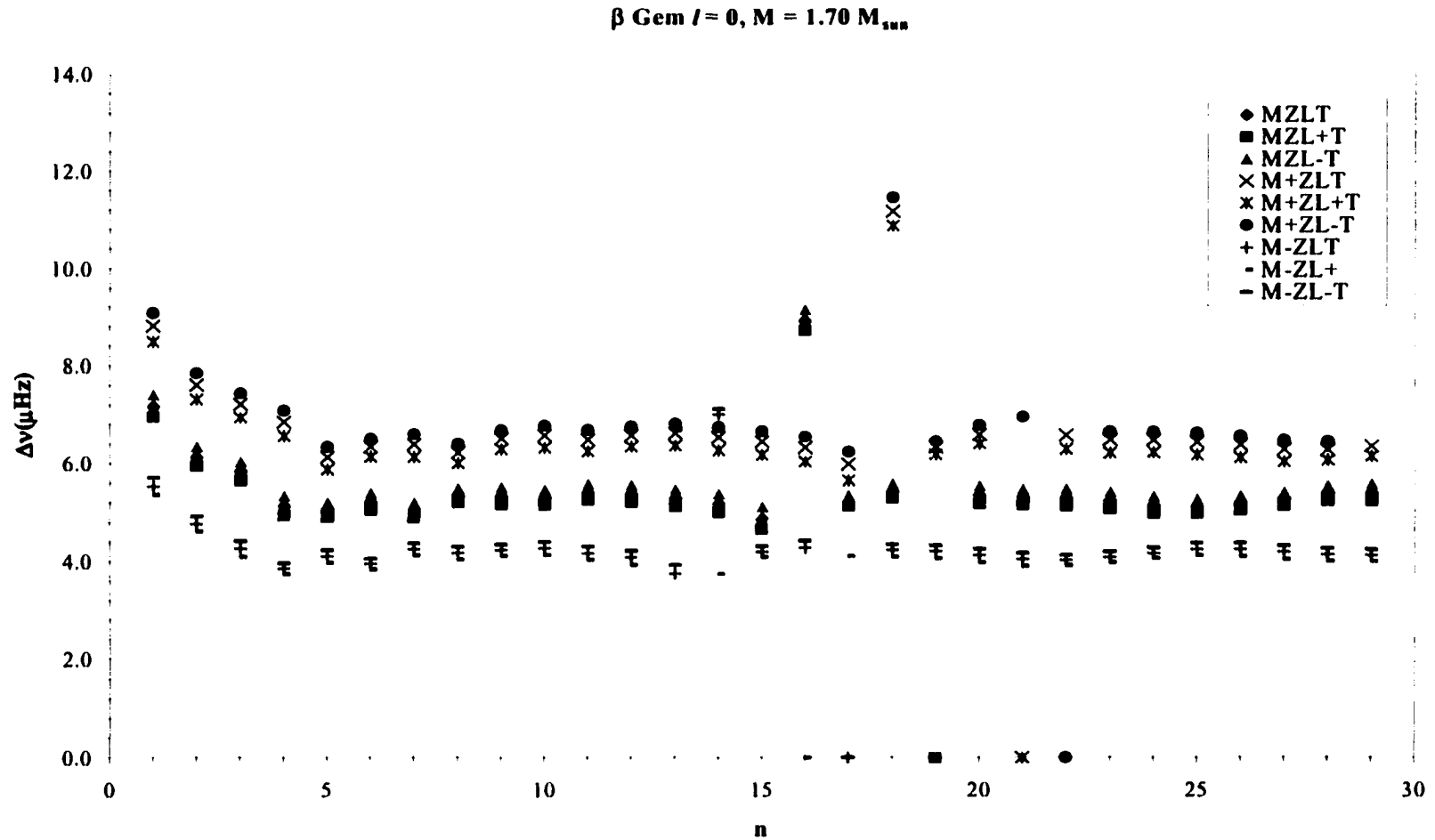


**Figure 5.5** Large frequency spacing for nine selected models. Each group of three models is for different masses. Higher mass models have the highest values, and lower mass the lowest. There are ambiguities for certain radial order frequencies, an indication of the sensitivity to the stellar structure.

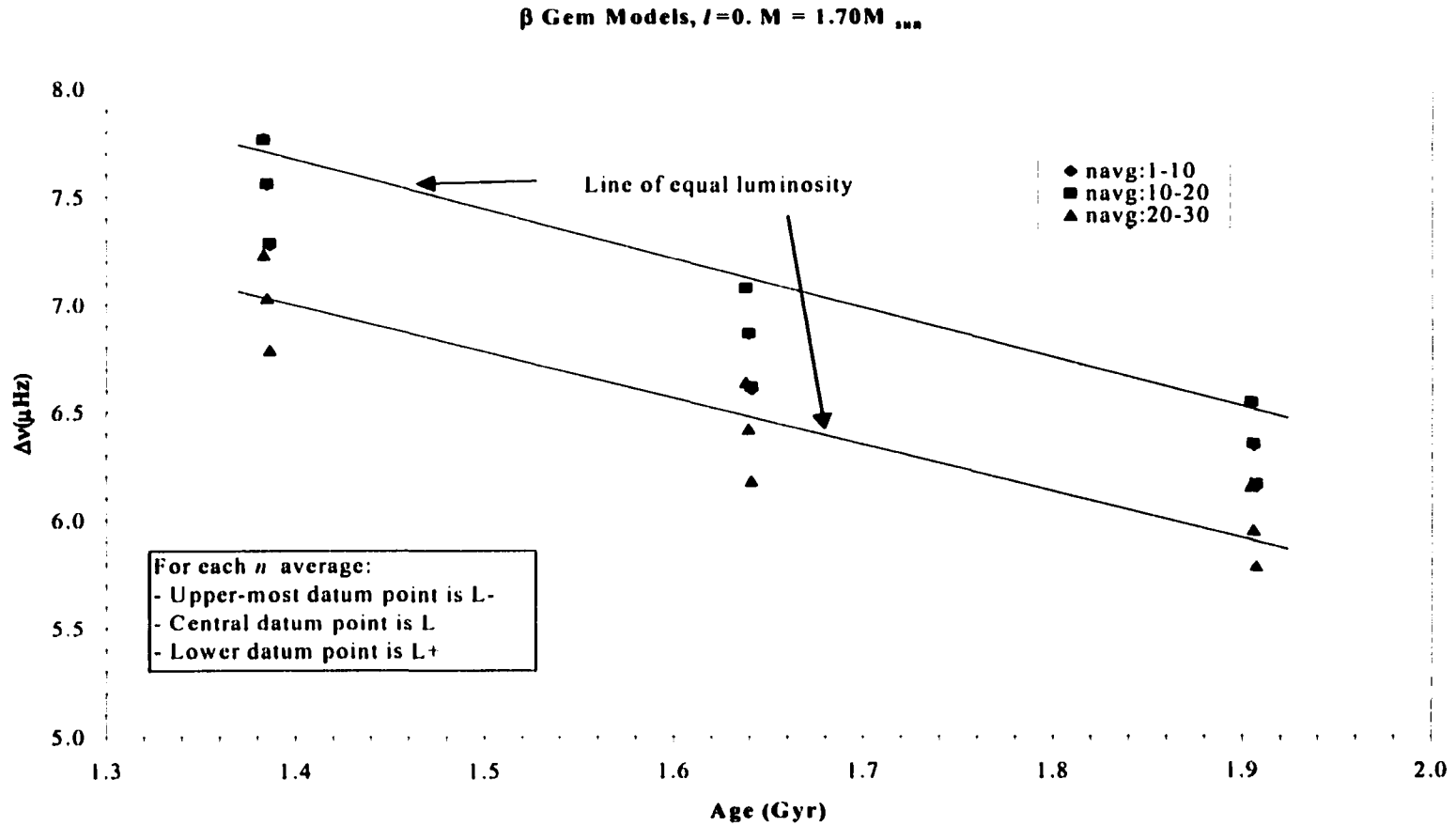


**Figure 5.6** Large frequency spacing plotted against age (Gyr). The linearity arises from the relationship between the large frequency spacing and radius. The models are collimated by models of equal metallicity and are linear in luminosity. The displacement of the  $n = 20 - 30$  averages is about  $-0.3 \mu\text{Hz}$  for each luminosity case.

is because of the relationship between the large spacing and radius. A relationship between the large frequency spacing and age cannot be made purely from the data, but the figure does show the differences that arise from the variation of the radial order value (only the  $1.70 M_{\odot}$  models are shown). The plot is collimated from the small variation in age for a model of a particular composition and note the displacement of the  $n = 20 - 30$  averages. This displacement is seen for all masses and separation increases with increasing mass:  $-0.2 \mu\text{Hz}$  for  $1.3 M_{\odot}$ ;  $-0.3$  for  $1.7 M_{\odot}$ ; and  $-0.50$  for the  $2.10 M_{\odot}$  models. This is an indication of the sensitivity of the higher radial order frequencies to the interior structure.

# Chapter 6

## Summary and Discussion

This thesis is an uncertainty analysis of the evolutionary state and non-radial pulsation spectrum of three stars in various stages of evolution:  $\epsilon$  Eridani is a main-sequence star,  $\beta$  Hydri is a subgiant, and  $\beta$  Geminorum is a red giant. The production of a theoretical pulsation spectrum results from the use of current knowledge about the physical nature of the stars. It should be made clear that the pulsation information produced by the models is not necessarily what will be observed, but can be used in conjunction with observations to obtain information on the stellar structure of the above stars.

### 6.1 $\epsilon$ Eridani

The main-sequence star  $\epsilon$  Eridani is shrouded in uncertainty. It is not a massive star so it has a long lifetime on the main-sequence. That means the uncertainty in  $\epsilon$  Eridani's age is large because of the sensitivity of the model to the stellar parameters used. That is probably  $\epsilon$  Eridani's most uncertain feature. Depending on the model parameters used, the age of the star ranges from less than one Gyr to about ten Gyr. That relation is shown for the models in Figures 3.6 (diffusion) and 3.7 (non-diffusion), the variation of age with the small frequency spacing. It is possible that that information can be used with successful observations by MOST and/or MONS to refine  $\epsilon$  Eridani's age, and constrain its stellar parameters even if observations differ significantly.

Figures 3.8 and 3.9 show that mode mixing is not as important in main-sequence stars, and depict the behavior of the Lamb and Brunt-Väisälä frequencies with the stellar structure. The peak of the Brunt-Väisälä frequency, hence  $g$ -modes, found at even lower frequencies, only influence the lowest frequency  $p$ -modes. It also shows the base of  $\epsilon$  Eridani's (simulated) convection zone to be around  $r = 0.7 R_*$ . The radial displacement (eigenfunction) in Figure 3.9 is shown as an example of how the amplitude of the oscillation changes as it propagates to greater depths.

## 6.2 $\beta$ Hydri

As for  $\epsilon$  Eridani, stellar evolution and seismological models were produced for the subgiant star  $\beta$  Hydri. There were some evolution models which could only converge to the correct  $T_{\text{eff}}$  and luminosity if their helium mass fraction was significantly increased. That is quite improbable for a star forming in the Milky Way, so the physics of stellar evolution dictate that  $M = 0.95 M_{\odot}$  is too low and  $\beta$  Hydri's mass is probably close to  $1.10 M_{\odot}$ .

The evolved state of the star means that the seismological analysis was affected by mode bumping because  $g$ -modes can propagate with higher frequencies and influence a greater range of the different  $p$ -modes. The pulsation analysis (Figure 4.5) produced large frequency spacings of the same order of magnitude as that observed by Bedding2001 ( $\Delta\nu = 56.2 \mu\text{Hz}$ ), and predicted by extrapolating from the Sun ( $\Delta\nu = 56.0 \mu\text{Hz}$ , KB95). The small frequency spacing was shown to be very sensitive to the stellar parameters and in the simulation it was resolved mostly for high values of the radial order

*n*. That is displayed in Figure 4.7, which shows a high amount of scatter for the small frequency spacing.

The models of  $\beta$  Hydri reveal, via a propagation diagram (Figure 4.8), a dense hydrogen exhausted core, surrounded by a hydrogen shell structure, and an outer convection zone starting at  $r \sim 0.7 R_*$ . The sharp peak in the Brunt-Väisälä frequency implies the mixing of low frequency *p*-modes, which is shown in the eigenfunction of an  $l = 4$  mode (Figure 4.10). It is likely that future seismological observations will display many of the mode mixing features discussed here.

### 6.3 $\beta$ Geminorum

Interestingly, the small uncertainty in Pollux's effective temperature may be used as a tight constraint on the star's evolutionary status with the aid of stellar models. Although it was not the purpose of our investigation, the models suggest that Pollux probably has a higher mass than first thought ( $1.70 - 2.10 M_{\odot}$ ), assuming a solar composition and mixing length parameter. The size of the uncertainty box in the HR-diagram for the star is small in comparison with the spread of its evolutionary tracks, and that limits the number of evolutionary models that can pass through  $\beta$  Gem's position on the HR-diagram.

A detailed seismological analysis was only calculated for the  $l = 0$  mode because higher degree oscillations will probably not be observed with any certainty. The calculations suggest that the large frequency spacing increases with mass and ranges from about 4.0 to 7.5  $\mu\text{Hz}$ . There are some discrepancies in the variation of the large spacing with radial order that arise from the misidentification of various modes. The small

frequency spacings could not be calculated. The variation of age with the large frequency spacing is shown in Figure 5.6, and the linearity is because of the relationship between the large spacing and radius. Although a definite relationship between the large frequency spacing and age cannot be made, the figure shows the differences that arise from the variation of the radial order value.

The mode mixing phenomenon was explored for the central model and found to be caused by the high frequency of the interior  $g$ -modes (Figure 5.2). Eigenfunctions of low degree modes are severely mixed, having  $p$ -mode structure in the outer envelope only and  $g$ -mode properties throughout the rest of the star (Figure 5.3). Higher degree eigenfunctions (not observable) are less affected by  $g$ -modes and have deeper turning points than stars in an earlier state of evolution (Figure 5.4).

Although no seismological observations of Pollux have been made (it is a MOST target star), the results here are in general agreement with what is expected from giant stars. Similar to Arcturus (§ 1.6.1) and  $\alpha$  UMa (§ 1.6.5), Pollux pulsates only in the radial mode ( $l = 0$ ), and higher degree modes are severely mixed with  $g$ -modes. Observationally, the frequencies of  $p$ -modes are very closely spaced for a given harmonic degree  $l$ , and that will make their identification from observations difficult.

## 6.4 General Conclusions and Summary

The oscillation spectrum of each star generally behaved as predicted; the frequency of the  $p$ -mode oscillations decreases in an evolving star, and the  $g$ -mode frequencies increase. That is shown in Figures 6.1 and 6.2. Figure 6.1 is the variation of the Lamb frequency (for  $l = 1$ ) with stellar radius fraction for the central model of each



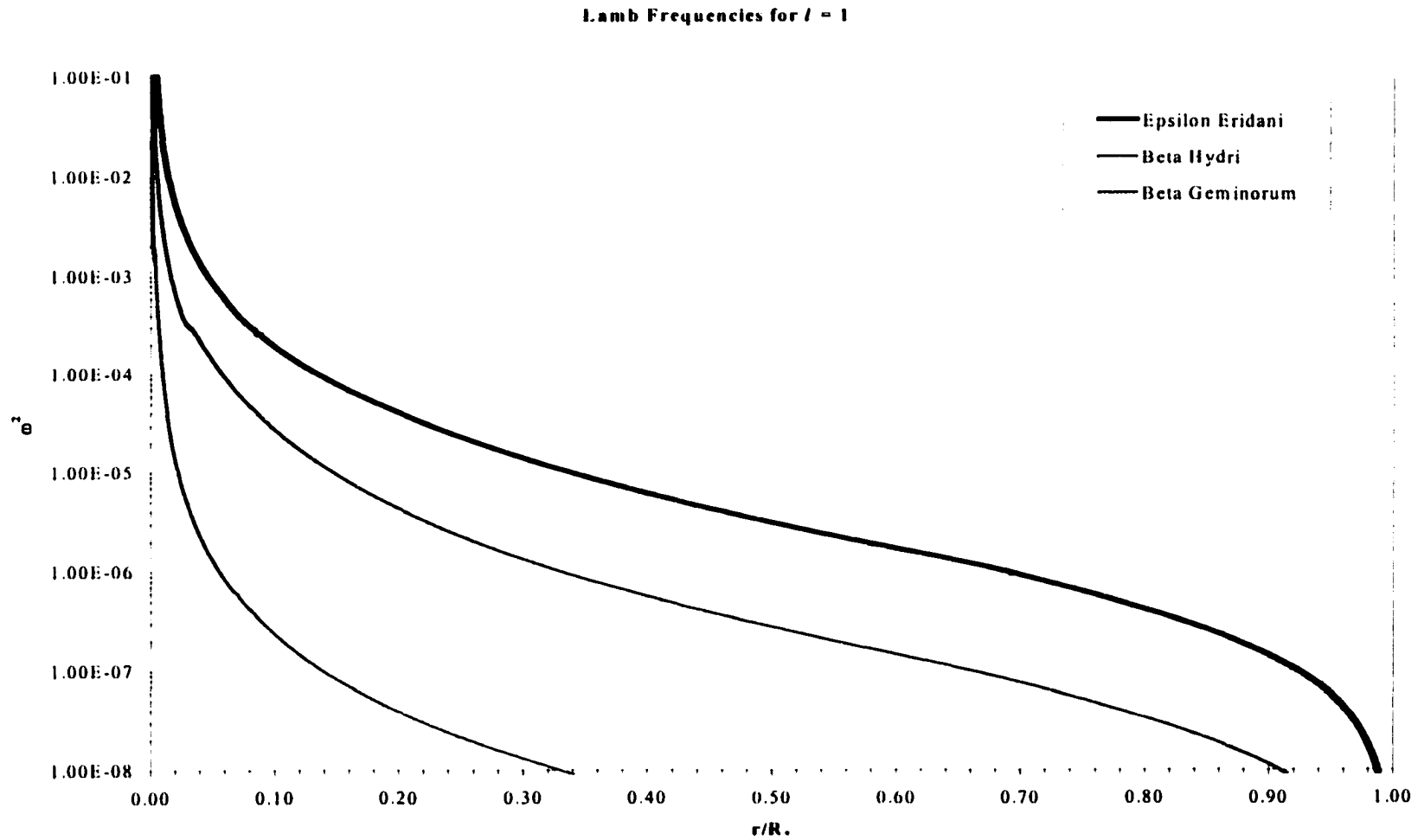


**Figure 6.1** The general variation of Lamb frequencies ( $l = 1$ ) with stellar evolution. The more evolved the star, the lower the  $p$ -mode spectrum. The above are the central modes for the three stars.

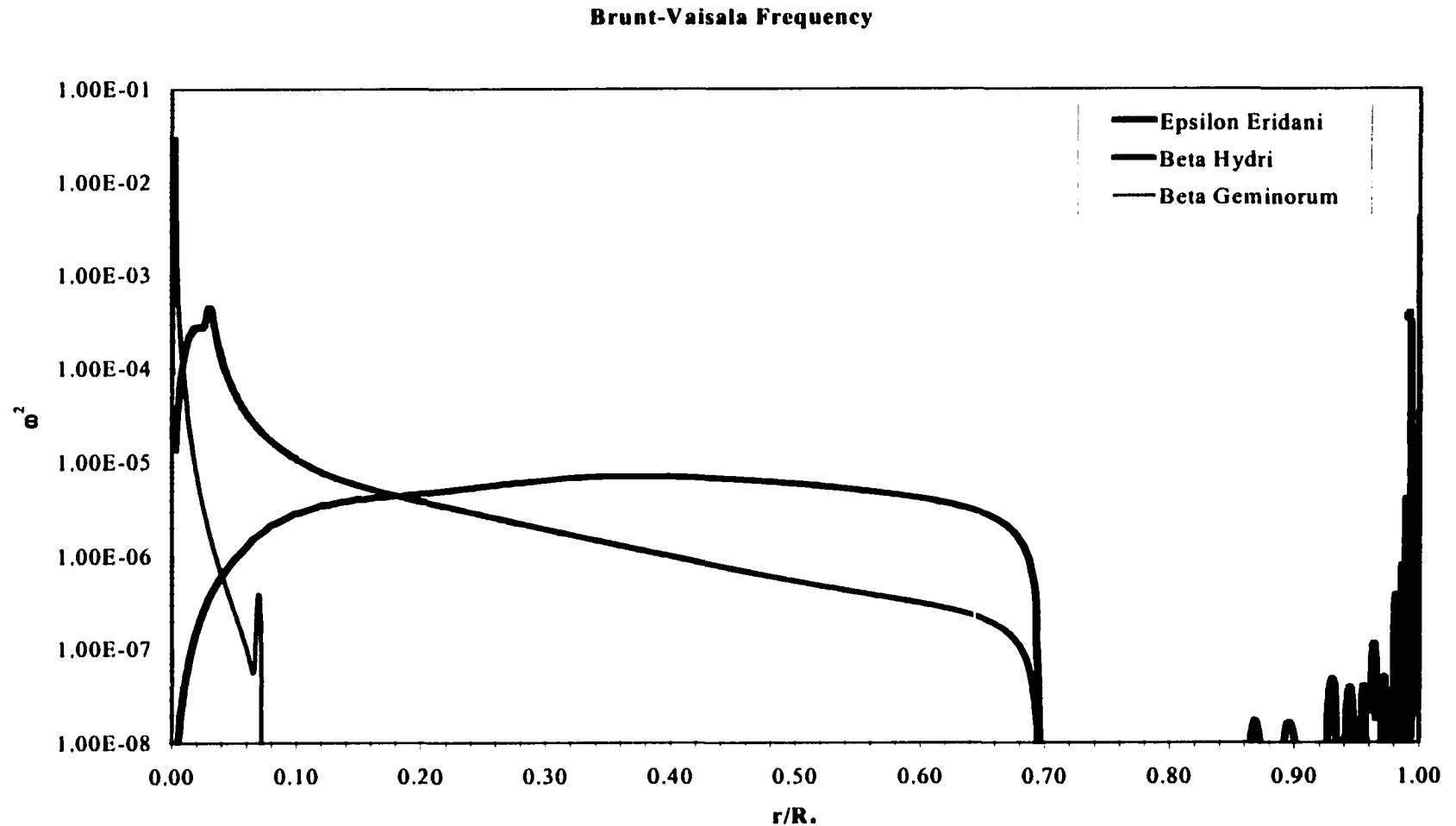


**Figure 6.2** The general variation of Brunt-Väisälä frequency with stellar evolution. The central models for the three stars is shown. Prominent features are the discontinuities at the base of the convection zones and the strength of  $N$  in the dense stellar cores.

star. The more evolved the star, the lower the oscillation frequencies. That arises from the relation of the frequencies with radius (mean density).

Similarly, Figure 6.2 shows that the variation of the Brunt-Väisälä frequency is very sensitive to stellar structure, so the variation of  $N$  with evolutionary state depends on what section of the stellar interior one is concerned with. The most apparent features in Figure 6.2 are the discontinuity at the base of the convection zones and the increase of frequency in the cores. It is these high frequencies that are responsible for the mode mixing observed in the results.

Observations of non-radial oscillations are only going to be sensitive to low degree modes, so the large and small frequency spacings determined for the stars will be very important. The small spacing is resolved for all the models of  $\epsilon$  Eridani and for the  $\beta$  Hydri models with a high radial order, but the small spacing is not resolved for the  $\beta$  Gem models. The large frequency spacing is easily obtained for all stars. The large spacing is displayed for all central models in Figure 6.3. The figure clearly shows the decrease of large spacing with evolution. The decrease arises from the dependence on the stellar radius.

The forthcoming non-radial oscillation observations by MOST and MONS will use the results presented here in one of two ways. If the observations identify frequencies (e.g. large and small frequency spacings) within the range of values calculated in this work, then we will be able to produce models to fine-tune the stellar parameters. The opposite case, where observations find very different frequency results, is more interesting and challenging because then we have to figure out what is the source of the discrepancies.

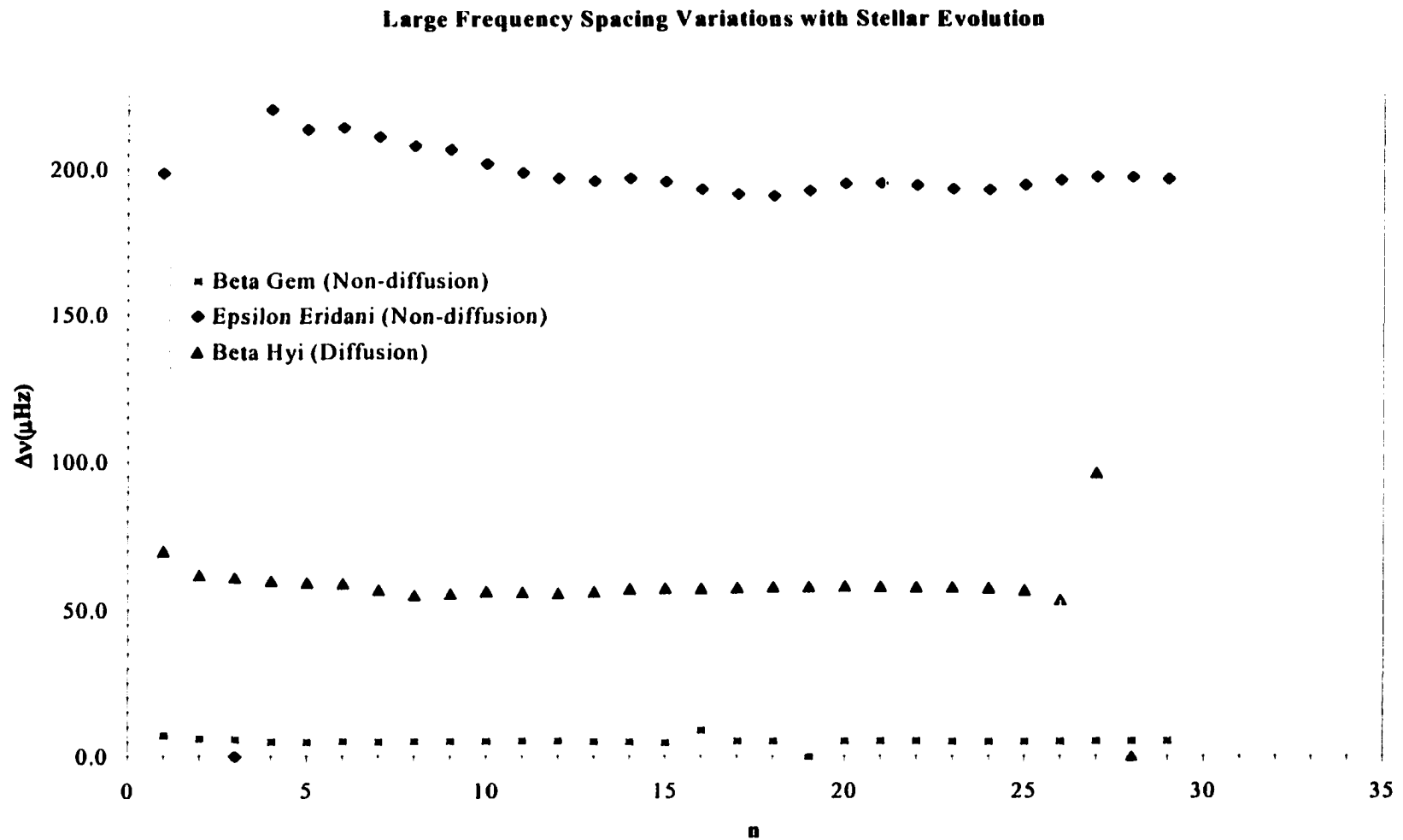


**Figure 6.3** The large average ( $20 \leq n \leq 30$ ) frequency spacing between the modes. The central models are displayed. This shows the decrease in  $\Delta\nu$  with evolution arising primarily from the increase in radius throughout stellar evolution.

# References

- Alexander, D.R., & Ferguson, J.W. 1994, ApJ, **437**, 879.
- Allende Prieto, C. & Lambert, D.L. 1994, A&A, **352**, 555.
- Andersen, B.N. 1984, Proc. 25<sup>th</sup> Liège Int. Astron. Coll., eds. Noels and Gabriel, p.220.
- Antia, H.M., & Basu, S. 1994, ApJ, **426**, 801.
- Antia, H.M., Chitre, S.M., & Gough, D.O. 1988, In: *Advances in Helio – and Asteroseismology*, IAU Symp. No. 123, ed. J. Christensen-Dalsgaard and S. Frandsen (D. Reidel Publ. Co., Dordrecht), p.371.
- Bahcall, J.N., & Pinsonneault, M.H. 1992, Rev. Mod. Phys. **64**, 85.
- Bahcall, J.N., Pinsonneault, M.H., Basu, S., & Christensen-Dalsgaard, J. 1997, Phys. Rev. Lett., **78**, 171-175.
- Baglin, A. *et al.* 1998, In: Deubner, F.L., Christensen-Dalsgaard, J., Kurtz, D.W. (eds.) Proc. IAU Symp. 185, *New Eyes to see Inside the Sun and Stars*, 301, Dordrecht: Kluwer, see also <http://www.astrsp-mrs.fr/www/COROT.html>
- Barban, C., Michel, E., Martić, M., Schmitt, J., Lebrun, J.C., Baglin, A., Bertaux, J.L. 1994, A&A, **350**, 617.
- Basu, S. 1997, MNRAS, **288**, 572.
- Basu, S. & Antia, H.M. 1988, In: *The Structure and Dynamics of the Interior of the Sun and Sun-like Stars*, eds. Korzennik, S.G., and Wilson, A. (ESA, Noordwijk, The Netherlands), p.711-715.
- Basu, S., & Antia, H.M. 1995, MNRAS, **276**, 1402.
- Bedding, T.R., Butler, P., Kjeldsen, H., *et al.* 2001, ApJ, *Letters*, **549**, L105
- Bedding, T.R., Kjeldsen, H., Christensen-Dalsgaard, J. 1998, CSSS, **10**, 741. ASP Conf. Ser. 154. The Tenth Cambridge Workshop on *Cool Stars, Stellar Systems, and the Sun*, ed. Donahue, R.A., & Bookbinder, J.A., p.741.
- Bell, R.A., & Gustafsson, B. 1989, MNRAS, **236**, 653.
- Belmonte, J.A., Jones, A.R., Pallé, P.L., & Roca Cortés, T. 1990, ApJ, **358**, 595.

- Bertelli, G., Bressan, A., Chiosi, C., Fagotto, F., Nasi, E. 1994, *A&AS*, **106**, 275.
- Blackwell, D.E., & Shallos, M.J. 1997, *MNRAS*, **180**, 177.
- Böhm – Vitnese, E. 1958, *Zs. Ap.*, **46**, 108.
- Bouchy, F., Carrier, F. 2001, astro-ph/0107099, accepted by *A&A*.
- Brown, T.M. 1990. *High Precision Doppler Measurements via Echelle Spectroscopy*.  
In: *CCDs in Astronomy*, ed. G.H. Jacoby, ASP Conf. Ser. **8**: 335. San Francisco:  
Astron. Soc. Pac.
- Brown, T.M., & Gilliland, R.L. 1990, *ApJ*, **350**, 893.
- Brown, T.M., & Gilliland, R.L. 1994, *ARA&A*, **32**, 37-82.
- Brown, T.M., Gilliland, R.L., Noyes, R.W., Ramsey, L.W., 1991, *ApJ*, **368**, 599.
- Brown, T.M., Kennelly, E.J., Korzennik, S.G., Nisenson, P., & Noyes, R.W. 1997, *ApJ*, **475**, 322.
- Bressan, A., Chiosi, C., & Fagotto, F. 1994, *ApJS*, **94**, 63.
- Buzasi, D., Catanzarite, J., Laher, R., Conrow, T., Shupe, D., Gautier III, T.N., Kreidl, T.,  
& Everett, D. 2000, *ApJ, Letters*, **532**, L133.
- Chaboyer, B., Demarque, P., Guenther, D.B., & Pinsonneault, M.H. 1995, *ApJ*, **446**, 435.
- Chen, K.R., Chou, C.-Y., & TON Team, 1996, *ApJ*, **485**, 985.
- Christensen-Dalsgaard, J. 1987, *Méthodes Mathématiques pour L'Astrophysique*, p.479-524, eds. Auvergne, M., & Baglin, A., (Société Française des Spécialiste d'Astronomie, Paris).
- Christensen-Dalsgaard, J. 1998, *Lecture Notes on Stellar Oscillations*, Fourth Edition.
- Christensen-Dalsgaard, J., Bedding, T.R., Kjeldsen, H. 1995, *ApJ, Letters*, **443**, L29.
- Christensen-Dalsgaard, J., Dilke, F.W.W., & Gough, D.O. 1974, *MNRAS*, **169**, 429.
- Christensen-Dalsgaard, J. & Frandsen, S. 1983, *Sol. Phys.*, **82**, 469.
- Christensen-Dalsgaard, J., & Frandsen, S., eds. 1988. *Advances in Helio – and Asteroseismology*, IAU Symp No. 123. Dordrecht: Reide.

- Christensen-Dalsgaard, J., Gough, D.O., & Libbrecht, K.G. 1989, *ApJ, Letters*, **341**, L103.
- Christensen-Dalsgaard, J., Gough, D.O., & Thompson, M.J. 1991, *ApJ*, **378**, 413.
- Clayton, D.D. 1968, *Principles of Stellar Evolution and Nucleosynthesis*, McGraw – Hill, Inc.
- Conti, P.S., Greenstein, J.L., Spinrad, H., & Wallerstein, G. 1967, *ApJ*, **148**, 105.
- Cox, A.N., Christie, S.M., Frandsen, S., Kumar, P. 1991, In: *Solar Interior and Atmosphere*, ed. A.N. Cox, W.C. Livingston, M.S. Matthews, p.618. Tucson: University Ariz. Press.
- Cox, J.P. 1968, *Principles of Stellar Structure*, Vol. 1: Physical Principles, Vol. 2: *Applications to Stars*, New York, Gordon & Breech.
- Cox, J.P. 1976, *ARA&A*, **14**, 247.
- Cox, J.P. 1980, *The Theory of Stellar Pulsation*, New Jersey, Princeton University Press.
- Däppen, W., & Gough, D.O. 1986, In: NATO ASI Ser. C 169, *Seismology of the Sun and the Distant Stars*, ed. D.O. Gough (Dordrecht: Reidel), p.275.
- Demarque, P., & Guenther, D.B. 1999, *Proc. Natl. Acad. Sci. USA*, Vol. **96**, p.5356-5359, May 1999.
- Demarque, P. Guenther, D.B., van Altena, W.F. 1986, *ApJ*, **300**, 773.
- Deubner, F.L. 1975, *A&A*, **44**, 371.
- Deubner, F., & Gough, D. 1984, *ARA&A*, **22**, 593.
- Drake, J.J. 1991, *MNRAS*, **251**, 369.
- Drake, J.J., and Smith, G. 1991, *MNRAS*, **250**, 89.
- Drake, J.J., & Smith, G. 1993, *ApJ*, **412**, 797.
- Dravins, D. Linde, P., Ayres, T.R., Linsky, J.L, Monsignori-Fossi, B., Simon, T., & Wallinder, F. 1993c, *ApJ*, **403**, 412.
- Dravins, D., Linde, P., Fredga, K., & Gahm, G.F. 1993b, *ApJ*, **403**, 396.
- Dravins, D., Lindegren, L., Nordlund, Å, & VandenBerg, D.A. 1993a, *ApJ*, **403**, 385.

- Dravins, D., Lindegren, L., & VandenBerg, D.A. 1998, *A&A*, **330**, 1077.
- Duvall, T.L., Jr., Harvey, J.W., Libbrecht, K.G., Popp, B.D., & Pomerantz, M.A. 1988, *ApJ*, **324**, 1158.
- Dziembowski, W., 1982, *AcA*, **32**, 147.
- Eddington, A.S. 1926, *The Internal Constitution of the Stars*, Cambridge University Press, Cambridge.
- Edmonds, P.D. 1993, Ph.D. Thesis, University of Sydney.
- Edmonds, P.D., & Cram, L.E. 1995, *MNRAS*, **276**, 1295.
- Edmonds, P.D., Cram, L.E., Demarque, P., Guenther, D.B., & Pinsonneault, M. 1992, *ApJ*, **394**, 313.
- Edvardsson, B., Anderson, J., Gustafsson, B., Lambert, D.L., Nissen, P.E., & Tamkin, J. 1993, *A&A*, **275**, 101.
- Frandsen, S. 1987, *A&A*, **181**, 289.
- Foster, G. 1996, *AJ*, **111**, 541.
- Gehren, T. 1981, *A&A*, **100**, 97.
- Gilliland, R.L., Brown, T.M., Kjeldsen, H., *et al.* 1993, *AJ*, **106**, 2441.
- Girard, T.M., Wu, H., Lee, J.T., Dyson, S.E., van Altena, W.F., Horch, E.P., Gilliland, R.L., *et al.* 2000, *ApJ*, **119**, 2428.
- Girard, T.M., Wu, H., Lee, J.T., Dyson, S.E. 1996, *BAAS*, **28**, 919.
- Goldreich, P., & Keeley, D.A. 1977, *ApJ*, **211**, 934.
- Goldreich, P., & Kumar, P. 1988, *ApJ*, **326**, 462.
- Goldreich, P., & Kumar, P. 1990, *ApJ*, **363**, 694.
- Gough, D.O. 1986. *Seismology of the Sun and the Distant Stars*, p.125-140, ed. Gough, D.O., Reidel, Dordrecht.
- Gough, D., & Toomre, J. 1991, *ARA&A*, **29**, 627.
- Gratton, L., & Gaudenzi, S., Rassi, C., & Gratton, R.G. 1981, *MNRAS*, **201**, 807.



- Gratton, R.G., & Ortolani, S. 1986, *A&A*, **169**, 201.
- Grec, G., Fossat, E., Pomerantz, M.A. 1983, *Sol. Phys.*, **82**, 55.
- Green, E.M., Demarque, P., & King, C.R. 1987, *The Revised Yale Isochrones and Luminosity Functions* (New Haven: Yale Observatory Press).
- Grevesse, N., Noels, A., & Sauval, A.J. 1996, in ASP Conf. Ser. 99, *Cosmic Abundances*, ed. S.S. Holt, & G. Sonneborn (San Francisco: ASP), 117.
- Griffin, R. 1976, *MNRAS*, **175**, 255.
- Guenther, D.B. 1987, *ApJ*, **312**, 211.
- Guenther, D.B., 1994, *ApJ*, **422**, 400.
- Guenther, D.B., & Demarque, P. 1986, *ApJ*, **301**, 207.
- Guenther, D.B., & Demarque, P. 1993, *ApJ*, **405**, 298.
- Guenther, D.B., & Demarque, P. 1996, *ApJ*, **456**, 798.
- Guenther, D.B., & Demarque, P. 1997, *ApJ*, **484**, 937,
- Guenther, D.B., & Demarque, P. 2000, *ApJ*, **531**, 503.
- Guenther, D.B., Demarque, P., Pinsonneault, M.H., & Kim, Y.-C. 1992b, *ApJ*, **392**, 328.
- Guenther, D.B., Demarque, P., Buzasi, J., Catanzarite, R., Laher, R., Conrow, T., & Kreidl, T. 2000, *ApJ, Letters*, **530**, L45.
- Guenther, D.B., Demarque, P., Kim, Y.-C., & Pinsonneault, M.H. 1992a, *ApJ*, **387**, 372.
- Guenther, D.B., & Kim, Y.-C., Demarque, P. 1996, *ApJ*, **463**, 382.
- Guenther, D.B., Krauss, L.M., & Demarque, P. 1998, *ApJ*, **498**, 871.
- Gustafsson, B., Kjaergaard, P., & Andersen, S. 1974, *A&A*, **34**, 99.
- Hallam, K.L., & Wolff, C.L. 1981, *ApJ, Letters*, **248**, L73.
- Hansen, C.J., & Kawaler, S.D. 1994, *Stellar Interior: Physical Principles, Structure and Evolution*, Springer-Verlag, New York, Inc.
- Harrington, R.S., *et al.* 1993, *AJ*, **105**, 1571.

- Harvey, J.W. 1988, *IAUS*, **123**, 497.
- Harvey, J. October 1995, *Physics Today*, p.32-38.
- Hayes, D.S. 1978, in IAU Symposium 80, *The HR Diagram*, ed. A.G.D. Philip and D.S. Hayes (Dordrecht: Reidel), p. 65.
- Hearnshaw, J.B. 1972, *Mmem. RAS*, **77**, 55.
- Hearnshaw, J.B. 1974, *A&A*, **4**, 11.
- Heasley, J.A., Janes, K., LaBonte, B., Guenther, D.B., Mickey, D., Demarque, P. 1996, *PASP*, **108**, 385.
- Hipparcos: European Space Agency (ESA). 1997, *The Hipparcos and Tycho Catalogues* (SP-1200; Noordwijk: ESA)
- Hoffleit, D. 1982. *The Bright Star Catalogue*, Yale University Observatory Press, Yale.
- Holweber, H. 1988. In: *The Impact of Very High S/N Spectroscopy on Stellar Physics*, IAU Symp. No. 132, p.411 eds. Cayrel de Strobel, G. & Spite, M., Kluwer, Dordrecht.
- Irwin, A.W., Fletcher, J.M., Yang, S.L.S., Walker, G.A.H., & Goodenough, G. 1992, *PASP*, **104**, 4891.
- Isaak, G.R., McLeod, C.P., Pallé, P.L., van der Raay, H.B., & Roca Cortés, T. 1989, *A&A*, **208**, 297.
- Jenkins, L.F. 1952, *General Catalogue of Trigonometric Stellar Parallaxes*, Yale Univ. Observatory Press.
- Jiménez, A., Álvarez, M., Andersen, N.B., *et al.* 1990, *Sol. Phys.*, **126**, 1.
- Johnson, H.L. 1966, *ARA&A*, **4**, 193.
- Kelch, W.L., Linsky, J.L., Basri, G.S., Chiu, H., Chang, S., Maran, S.P., & Furenlid, I. 1978, *ApJ*, **220**, 962.
- Kippenhahn, R., & Baker, N. 1965, *ApJ*, **142**, 868.
- Kjeldsen, H., & Bedding, T.R., Viskum, M., & Frandsen, S. 1995 (KBVF), *AJ*, **109**, 1313.
- Kjeldsen, H., & Bedding, T.R. 1995 (KB95), *A&A*, **293**, 87.

- Kjeldsen, H., & Bedding, T.R. 2000, *Current Status of Asteroseismology*, astro-ph/ No. 0011354, v1, 19 Nov. 2000.
- Kjeldsen, H., Bedding, T.R., Christensen-Dalsgaard, J. 2000, In: : Szabados, L., Kurtz, D. (eds.) IAU Colloquium 176: *The Impact of Large-Scale Surveys on Pulsating Star Research*, Vol. 203, 73, ASP Conf. Ser., see also <http://astro.ifa.au.dk/MONS>
- Kjeldsen, H., Bedding, T.R., Frandsen, S., & Dall, T.H. 1999, MNRAS, **303**, 579.
- Krishna Swamy, K.S. 1966, ApJ, **145**, 174.
- Kumar, P., Franklin, J., & Goldreich, P. 1988, ApJ, **328**, 879.
- Kumar, P., & Lu, E. 1991, ApJ, *Letter*, **375**, L35.
- Kurucz, R.L. 1979, ApJS, **40**, 1.
- Lambert, D.L., & Reis, L.M. 1977, ApJ, **217**, 508.
- Lambert, D.L., & Reis, L.M. 1981, ApJ, **248**, 228.
- Leibacher, J.W., Stein, R.F. 1971, ApJ, *Letters*, **7**, L191.
- Leighton, R.B., Noyes, R.W., Simon, G.W. 1962, ApJ, **135**, 475.
- Libbrecht, L.G., & Woodward, M.F. 1991, Sci, **253**, 152.
- Martić, M., Schmitt, J., Lebrun, J.-C., Barban, C. *et al.* 1999, A&A, **351**, 993.
- Matthews, J.M., Kuschnig, R., Walker, G.A.H., *et al.* 2000, In: Szabados, L., Kurtz, D. (eds.) IAU Colloquium 176: *The Impact of Large-Scale Surveys on Pulsating Star Research*, Vol. 203, 74, ASP Conf. Ser., see also <http://www.astro.ubc.ca/MOST>
- Michaud, G. 1970, ApJ, **160**, 641.
- Michaud, G. 1986, ApJ, **302**, 650.
- Middlekoop, F., Vaughan, A.H., and Preston, G.W. 1981, A&A, **96**, 401.
- Nigam, R., & Kosovichev, A.G. 1999, ApJ, *Letters*, **514**, L53.
- Nordlund, A.A., & Stein, R.F., 1996, In: Proceedings of the 32<sup>nd</sup> Liège Colloquium, eds. Noels, A., Fraipont-Caro, D., Gabriel, M., Grevesse, N., & Demarque, P. (Univ. Liège, Belgium), p.75-93.

- Noyes, R.W., Baliunas, S.L., Belserene, E., Duncan, D.K., Hornes, J., & Wildrow, L. 1984, *ApJ, Letters*, **285**, L23.
- Oinas, V. 1974a, *ApJS*, **27**, 391.
- Oinas, V. 1974b, *ApJS*, **27**, 405.
- Olive, K.A., & Steigman, G. 1995, *ApJS*, **97**, 49.
- Peri, Michal Leah, 1995, Ph.D. Thesis, California Institute of Technology.
- Pinsonneault, M.H. 1988, Ph.D. Thesis, Yale University.
- Pottasch, E.M., Butcher, H.R., van Hoesel, F.H.J. 1992, *A&A*, **264**, 138.
- Prather, M. 1976, Ph.D. Thesis, Yale University.
- Proust, D., & Foy, R. 1988, *Ap&SS*, **145**, 61.
- Queloz, D., Mayor, M., Weber, L., *et al.* 2000, *A&A*, **354**, 99.
- Rebolo, R., Crivellari, L., Castelli, F., Foing, B., Beckman, J.E. 1986, *A&A*, **166**, 195.
- Régulo, C., Jiménez, A., Pallé, P.L., Pérez Hernández, F., & Roca Cortés, T. 1994, *ApJ*, **434**, 384.
- Richard, O., Dziembowski, W.A., Sienkiewicz, R., and Goode, P.R. 1998, *A&A*, **338**, 756.
- Roberts, D.H., Lehár, J., & Dreher, J.W. 1987, *AJ*, **93**, 968.
- Rodgers, A.W., & Bell, R.A. 1963, *Observatory*, **83**, 79.
- Rogers, F.J., & Iglesias, C.A. 1992, *ApJS*, **79**, 507.
- Rogers, F.J., Swenson, F.J., Iglesias, C.A. 1996, *ApJ*, **456**, 902.
- Ruland, F., Holweger, H., Griffin, R., & Biehl, D. 1980, *A&A*, **92**, 70.
- Saio, H., & Cox, J.P. 1980, *ApJ*, **236**, 549.
- Samadi, R. 2000, Ph.D. Thesis, Université Paris.
- Samadi, R., & Goupil, M.-J. 2001, *A&A*, **370**, 136.
- Samadi, R., Goupil, M.-J., Lebreton, Y. 2001, *A&A*, **370**, 147.

- Schmitz, F., & Ulmscheider, P. 1980, A&A, **84**, 191.
- Schou, J., & Buzasi, D.L. 2000, AAS, **197**, 4604S
- Schwarzschild, M. 1958, *Structure and Evolution of the Stars*, Princeton University Press.
- Scuflaire, R. 1974, A&A, **36**, 107.
- Shibahashi, H., Osaki, Y., Unno, W. 1975, Pull. Aston. Soc Japan, **27**, 401.
- Shkolnik, E. 2000, M.Sc. Thesis, University of British Columbia.
- Smith, G., & Drake, J.J. 1987, A&A, **181**, 103.
- Soderblom, D.R. 1986, A&A, **158**, 273.
- Soderblom, D.R., & Däppen, W. 1989, ApJ, **342**, 945.
- Söderhjelm, S. 1999, A&A, **341**, 121.
- Spiegel, E.A., Zahn, J.-P. 1992, A&A, **265**, 106.
- Steenbock, W. 1985. In: *Cool Stars with Excesses of Heavy Elements*, p.231, eds. Jaschek, M. & Keenan, P.C., Reidel, Dordrecht.
- Steenbock, W., & Holweger, H. 1981, A&A, **99**, 192.
- Strand, K.Aa. 1951, ApJ, **113**, 1.
- Tassoul, M. 1980, ApJS, **43**, 469.
- Tomkin, J., & Lambert, D.L. 1979, ApJ, **227**, 209.
- Tomkin, J., & Lambert, D.L. 1983, ApJ, **273**, 722.
- Tomkin, J., Lambert, D.L., & Balchandran, S. 1985, ApJ, **290**, 289.
- Toomre, A. 1970, IAUS, **38**, 334.
- Toutain, T., Fröhlich, C. 1992, A&A, **257**, 287.
- Ulrich, R.K. 1970, ApJ, **162**, 993.
- Ulrich, R.K. 1986, ApJ, *Letters*, **306**, L37.

- Ulrich, R.K. 1988, Proc. IAU Symposium No. 123, *Advances in Helio – and Asteroseismology*, p.299-302, eds. Chrsitensen-Dalsgaard, J., and Frandsen, S., Reidel, Dordrecht.
- Unno, W., Osaki, Y., Ando, H., Saio, H., Shibahashi, H. 1989, *Nonradial Oscillations of Stars: Second Edition*, University of Tokyo Press.
- van Altena, W.F., Lee, J.T., Hoffleit, E.D. 1995, *The General Catalogue of Trigonometric Stellar Parallaxes*, Fourth Ed., New Haven: Yale University Observatory Press. Vol. I.
- Vandakurov, Yu.V. 1979, Astr. Zh., **56**, 750.
- VandenBerg, D.A. 1983, ApJS, **51**, 29.
- VandenBerg, D.A., & Bell, R.A. 1985, ApJS, **58**, 561.
- VandenBerg, D.A., & Bridges, T.S. 1984, ApJ, **278**, 679.
- VandenBerg, D.A., Swenson, F.J., Rogers, F.J., Iglesias, C.A., & Alexander. D.R. 2000, ApJ, **532**, 430.
- Williams, P.M. 1971, MNRAS, **155**, 215.
- Woolley, R., Epps, E.A., Penston, M.J., Pocock, S.B. 1970, Royal Observatory Annals No. 5.
- Young, A.T. 1967, AJ, **72**, 747.
- Young, A.T. 1993. Obs, **113**, 41.
- Zhevakin, S.A. 1963, ARA&A, **1**, 367,

## **Peter A. MacDonald**

181 Arnett Street  
Summerside, PEI, C1N 2N2  
(902) 436-3614 (Home)

### **EDUCATION:**

#### **1999-2001**

M.Sc. in Astronomy, October 2001, Saint Mary's University, Halifax, NS

#### **1994-1998**

B.Sc. in Physics and Mathematics (Honours), May 1999, University of Prince Edward Island, Charlottetown, PEI

#### **1992-1995**

High School Diploma, Honours, Three Oaks Senior High School, Summerside, PEI

### **RELEVANT EXPERIENCE:**

#### **2000**

Coordinated an internet based astronomy class at Saint Mary's University along with other graduate students. Responsibilities included overseeing and marking tests and exams along with handling any problems that came up during the course because the class professor teaches at the University of Hawaii.

#### **1999-2001**

Telescope tour guide for the public at the Burke-Gaffney Observatory, Saint Mary's University.

First year physics lab demonstrator, Saint Mary's University. Responsibilities included maintaining classroom order, ensuring the labs run smoothly and safely, knowledge of the equipment used, and the grading of lab reports.

#### **1996-1998**

Grading responsibilities at the University of Prince Edward Island for the Department of Mathematics.

### **PUBLICATIONS:**

M.Sc. Thesis, Saint Mary's University, Halifax Nova Scotia, 2001

## **Internal Publications and Conference Proceedings**

MacDonald, P.A. 2001, poster presentation, CASCA conference, Hamilton, ON, May 26-29, 2001, "ε Eridani: A Stellar Model and Seismological Analysis"

## **REFERENCES**

Dr. David Guenther  
Associate Professor  
Astronomy & Physics  
Saint Mary's University  
Halifax, NS  
B3H 3C3  
(902) 420-5637  
guenther@ap.stmarys.ca